AGN in the X-ray
Relativistic effects in the Fe Kα line

Linda Baronchelli

München 2020

AGN in the X-ray
Relativistic effects in the Fe Kα line

Linda Baronchelli

Dissertation
an der Physik
der Ludwig–Maximilians–Universität
München

vorgelegt von
Linda Baronchelli
aus Novazzano

München, den 4. August 2020

Erstgutachter: Prof. Dr. Kirpal Nandra
Zweitgutachter: Prof. Dr. Jochen Weller
Tag der mündlichen Prüfung: 15.09.2020

Contents

List of Figures

List of Tables

Zusammenfassung

Aktive Galaxienkerne (AGN) werden durch Materie angetrieben, die in ein supermassives Schwarzes Loch (SMBH) einfällt. Diese Objekte emittieren stark in allen Wellenlängen und gehören zu den leuchtkräftigsten langlebigen Quellen im Universum. Die von diesen Systemen emittierte Röntgenstrahlung ist von besonderem Interesse, da sie in unmittelbarer Nähe des SMBH erzeugt wird und dadurch die Signatur seines extremen Gravitationsfeldes trägt. Die primäre Röntgenstrahlung entsteht wenn optische/UV-Scheibenphotonen an einer Korona heißer Elektronen, die das SMBH umgibt, invers Compton gestreut werden. Das Spektrum der primären Röntgenstrahlung hat die Form eines Potenzgesetzes. Ein Teil dieser Strahlung erreicht den Beobachter, während der verbleibende Teil vom Gas und Staub im Akkretionsstrom reflektiert und wiederaufbereitet wird. Aus dem Reflexionsspektrum kann die Geometrie und Zusammensetzung der das SMBH umgebenden Materie sowie relativistische Eigenschaften des SMBH selbst (z.B. den Spin) abgeleitet werden. In dieser Arbeit versuche ich, die Häufigkeit relativistischer Effekte in der Reflexionskomponente der AGN im Röntgenlicht festzustellen. Insbesondere möchte ich feststellen, wie häufig man eine relativistische verschwommene Eisen (Fe)-Kα-Linie in einer großen Stichprobe dieser Objekte beobachten kann.

Die Fe Kα-Linie befindet sich bei einer Ruheenergie von 6,4 keV und ist eines der hervorstechendsten Merkmale des Röntgenreflexionsspektrums der AGN. Die natürliche Linenbreite der Fe Kα-Linie ist schmal (10 eV), kann aber durch relativistische Effekte bis zu einer Energiebreite von 3 keV gedehnt und verzerrt werden. Dies macht sie zum perfekten Merkmal zur Messung von BH-Spin und Scheibenneigung.

Breite Fe Kα-Linien werden häufig im nahen Universum beobachtet, ihre Häufigkeit bei höheren Rotverschiebungen wird jedoch immer noch diskutiert. Um dieser Fragestellung nachzugehen, analysiere ich 199 Quellen aus einem der tiefsten *Chandra*-Felder, dem *Chandra* Deep Field South (CDFS) 4Ms. Mit Hilfe des Software-Paketes BXA passe ich Modelle an die Röntgenspektren an und bestimme die besten Anpassungsparameter, sowie die Bayessche Evidenz für die verwendeten Modelle. Dieser Ansatz ermöglicht es mir, die Bayes'schen Evidenzen eines Modells für die gesamte Stichprobe zu finden, indem ich alle Spektren in der Stichprobe einzeln anpasse und die einzelnen Evidenzen kombiniere. Diese Methode hat mehrere Vorteile gegenüber dem Aufsummieren von Spektren und dem Anpassen des gesamten gemittelten Spektrums. Unter anderem wird das Risiko einer künstlichen Vergrößerung der Linienverbreiterung aufgrund von Unsicherheiten in der Rotverschiebung verringert, und der gesamte Bayes'sche Evidenz für die Stichprobe kann für den Bayes'schen Modellvergleich verwendet werden. Unter Verwendung der aufsummierte Evidenz zur Berechnung der Bayes-Faktoren für verschiedene Anpassungen

vergleiche ich vier zunehmend komplexere Modelle. Das einfachste Modell ist ein absorbiertes Potenzgesetz, zu dem für die komplexeren Modelle jeweils eine schmale oder eine breite Reflexionskomponente hinzugefügt wird (letztere jeweils mit Spin gleich 0 oder 1). Dieser Ansatz zeigt, dass die Population der AGN bei z>0,5 bevorzugt mit einem Modell angepasst wird, das eine breite Reflexionskomponente mit maximal drehendem SMBH enthält. Die überwiegende Mehrheit der Spektren hat ein zu geringes Signal-Rausch-Verhältnis (S/N), um zwischen den unterschiedlichen Modellen zu unterscheiden. Die beiden hellsten Quellen der Probe haben jedoch ein Signal-Rausch-Verhältnis, das hoch genug ist, um eine signifikante Präferenz für das Modell mit einer unscharfen Reflexionskomponente zu zeigen. Dies lässt vermuten, dass die breite Fe Kα-Linie bei unzureichendem S/N Verhältnis nicht detektiert werden kann.

Dieses Ergebnis wird durch die Analyse von 2237 Quellen aus den vier tiefsten *Chandra*-Durchmusterungen bestätigt: die CDFS 7Ms, das *Chandra*-Tiefenfeld Nord (CDFN), die AEGIS- und COSMOS-Felder. Diese Stichprobe wurde anhand ihres harten Spektrums selektiert. Diese Studie führt zu neuen S/N-Beschränkungen für die Signifikanz der Methode. Dank eines neuen Ansatzes mit einem hierarchischen Bayes'schen Modell untersuche ich die Beziehung zwischen der Luminosität der Quelle und dem Reflexionsanteil der schmal Reflexion vom Torus und der breiten Reflexion von der Scheibe für diese erweiterte Stichprobe. Wie bereits durch den Iwasawa-Taniguchi-Effekt (oder Röntgen- Baldwin-Effekt) erklärt, ist der Reflexionsanteil mit der Luminosität antikorreliert. Dies bestätigt die Ergebnisse von Nandra et al. (1997a).

BXA und der Bayes'sche Modellvergleich ermöglichen es uns Modelle zu finden, die eine Population mit niedrigen S/N-Spektren bestmöglichst beschreiben. Die Analyse individueller Quellen benötigt hingegen ein viel höheres S/N Verältnis. Dies gilt auch für Modelle mit höherer Komplexität. Die Anpassung eines komplexen Modells mit vielen freien Parametern an ein Spektrums mit niedrigem Rauschabstand kann zu einer Überanpassung führen.

Aus diesen Gründen schließe ich diese Arbeit mit einer detaillierten Analyse von acht *XMM-Newton* Beobachtungen von MCG–6-30-15 mit hohem S/N Verhältnis ab. Die Qualität dieser Spektren erlaubt es mir komplexere bestehende Modelle auf relativistische Reflexion zu testen und Effekte aufgrund von Ionisation in der Anpassung zu berücksichtigen.

Abstract

Active galactic nuclei (AGN) are powered by matter infalling into a supermassive black hole (SMBH). These objects emit strongly in all the wavelengths and are some of the most powerful persistent sources in the Universe. The X-ray radiation emitted from these systems is of particular interest since it is produced in the direct proximity of the SMBH and it carries the signature of its extreme gravitational field. The primary X-ray radiation has the shape of a power-law and it arises when optical/UV disc photons are inverse Compton scattered by a corona of hot electrons surrounding the SMBH. Part of this radiation reaches the observer, while the remaining gets reflected and reprocessed by the gas and dust in the accretion flow. The originating reflection spectrum can unveil the geometry and composition of the matter surrounding the SMBH and relativistic properties of the SMBH itself (e.g. the spin). In this work, I aim to establish the ubiquity of relativistic effects in the reflection component of AGN in the X-ray. In particular, I want to determine how often one can observe a relativistic blurred iron (Fe) Kα line in a large sample of these objects.

The Fe Kα line, at 6.4 keV in the rest frame, is one of the most prominent features of the X-ray reflection spectrum of AGN. The Fe Kα line is intrinsically narrow (10 eV) but it can be stretched and skewed by relativistic effects up to an energy width of 3 keV. This makes it the perfect tool to measure BH spin and disk inclination.

Broad Fe Kα line are commonly observed in the nearby Universe, however, their ubiquity at higher redshift is still debated. To address this issue, I analyze 199 sources from one of the deepest *Chandra* fields, the *Chandra* deep field south (CDFS) 4Ms, using a Bayesian framework called BXA to fit X-ray spectra and obtain the best-fit parameters and the Bayesian evidence for the used model. This approach allows me to find the Bayesian evidence for a model for the full sample by fitting singularly all the spectra in the sample and stacking the individual evidence. This method has several advantages over stacking the spectra and fitting the total averaged spectrum, among which the risk of artificially increasing the broadening of the line due to uncertainties in the redshift is reduced and the total Bayesian evidence for the sample can be used for Bayesian model comparison. Using the stacked evidence to calculate the Bayes factors for different fits, I compare four increasingly complex models, starting from an absorbed power-law and adding a narrow reflection component and later a broad reflection component (spin equal 0 or 1). This approach shows, that the population of AGN at z>0.5 is preferentially fitted with a model including a broad reflection component with maximally spinning SMBH. The vast majority of the spectra have signal-to-noise ratio (S/N) too low to rule-out the models for the individual sources. However, the two brightest sources of the sample have S/N high enough to

show a clear preference for the model containing a blurred reflection component. This seems to confirm that if the broad Fe Kα line is not detected in a spectrum it might be due to an insufficient S/N.

The result is later confirmed by repeating the analysis on a sample of 2237 hard selected X-ray spectra from the four deepest *Chandra*, surveys: the CDFS 7Ms, the *Chandra* deep field north (CDFN), the AEGIS and COSMOS fields. This study leads to new S/N constraints for the method to be significant. Thanks to a new approach involving a hierarchical Bayesian model, I study the relation between the luminosity of the source and reflection fraction of narrow reflection from the torus and broad reflection from the disc for this extended sample. The reflection fraction is found to be anti-correlated with the luminosity as explained by the Iwasawa-Taniguchi (or X-ray Baldwin) effect, confirming the found from Nandra et al. (1997a).

BXA and Bayesian model comparison allow us to find models to describe at best a population of low S/N spectra. However, if we would try to rule-out and confirm models for single sources we would need a much higher S/N. The same argument applies to a model of higher complexity, in fact, fitting a low S/N spectrum with a complex model with many free parameters might lead to overfitting.

For these reasons, I conclude this thesis with a detailed analysis of eight high S/N *XMM* observations of MCG–6-30-15. The quality of these spectra allows me to test more complex existing models for relativistic reflection and to include also effects due to ionization in the fit.

Chapter 1

Introduction

Active Galactic Nuclei (AGN) are the most luminous persistent objects in the Universe. Their emitted energy varies from $< 10^{40}$ erg $\cdot$ s^{-1}, for some of the most nearby galaxies, to $> 10^{47}$ erg $\cdot$ s^{-1}, for distant quasars. The emission of these objects spans the full electromagnetic spectrum and can be powerful enough to outshine the luminosity of all the stars in the host galaxy combined. The luminosity of AGN is highly variable on time scales from years to days, hours, and sometimes even minutes. This implies that these systems must be spatially small (Salpeter 1964) (see Sec. 1.1 for more details). Moreover, high luminosities imply high masses such that gravity can counteract radiation pressure and the object does not disrupt. Hence, it is supposed that AGN is powered by matter falling into supermassive black holes (SMBH) with masses that can be of 10^8 M$_\odot$ or more (e.g. Rees & Mészáros 1998, for a review).

These powerful engines undergo one of the most efficient processes to convert matter into energy (see Sec. 1.3.2). The study of their emitted radiation can be used to probe general relativistic effects and to study black hole (BH) growth. Especially in the X-ray wavelengths, thought to be emitted in the direct proximity of the central SMBH, we can learn about the behavior of matter and radiation in extreme gravitational fields.

Despite the fact that these exotic objects have been known for more than a century, many mysteries connected to AGN accretion and evolution remain unsolved, making this one of the most active research fields in Astrophysics.

In this chapter, I provide an overview of AGN as a phenomenon. In the first section I will give a brief summary of the steps in astronomy history that lead us to the knowledge on AGN we have today (see Sec. 1.1). In the sections afterward I will address the physics behind AGN and black holes with particular attention to the X-ray radiation emitted by these objects (see Sec. from 1.2 to 1.4). I end the chapter with an overview of astronomical X-ray instruments, discussing the observatories most relevant in this thesis, in particular *Chandra*, *XMM*, *eROSITA* and *Athena* (see Sec. 1.5).

1.1 Observational history of AGN

NGC 1068 was the first AGN for which an optical spectrum was obtained by Fath (1909) at the Lick Observatory, during a study of spiral nebulae, now known to be galaxies. He observed that NGC 1068 presented strong high-ionization emission lines similar to those in planetary nebulae. Other researches, for example Slipher (1917) soon afterwards obtained better spectra of the same source and of the somewhat similar NGC 4151. Hubble (1926) showed that the spiral nebulae, like NGC 1068, 4051 and 4151, now known as AGN, are actually of extragalactic nature and all present planetary-nebula-like emission lines. However, it was only seventeen years later that Seyfert (1943) realized that there are several similar galaxies with high central surface brightness, i.e. stellar-like cores. He found that the optical spectra of these galaxies are dominated by high-excitation nuclear emission lines with width up to 8500 km s^{-1} and that the hydrogen lines are sometimes broader than the other lines. However, Seyfert's work was not yet enough to spark the interest of the astronomical community in these objects. In fact, Seyfert galaxies were not probed further until after the dawn of radio astronomy (Jansky 1933), when Baade & Minkowski (1954) detected some of these galaxies at radio wavelengths.

A major breakthrough was made by Minkowski (1960) with the identification of the radio source 3C 295 with a galaxy in a galaxy cluster at the unprecedented redshift of 0.46.

The same year, Allan Sandage took an image 3C 48, which appeared to be a star-like object surrounded by a faint nebulosity. Several other similar objects where found to coincide with radio sources and their spectra showed broad emission lines at unexpected wavelengths (Matthews & Sandage 1963). Such objects were referred to as quasi-stellar radio sources or quasars.

At first, quasars were believed to be stars in the Milky Way showing peculiar properties. However this scenario was difficult to reconcile with the presence of forbidden lines and with the broadness of the emission lines. Only after the works of Hazard et al. (1963), Schmidt (1963), Oke (1963) and Greenstein & Matthews (1963), that identified the rest frame wavelength of the observed emission lines in 3C 273 and 3C 48, it became clear that these objects were of extragalactic nature, with redshifts reflecting the Hubble expansion. Moreover, Kristian (1973) showed that the nebulosity surrounding the star-like bright core of a sample of quasars was consistent with a presence of a host galaxy.

The field was further enlarged by the discovery of a large radio-quiet sample that showed the same properties as quasars, identified by an excess in the UV wavelengths (Matthews & Sandage 1963). These extremely bright and variable sources were named quasi stellar galaxies or quasi stellar objects (QSO) (Sandage 1965). Only around that time the parallel between QSO and Seyfert galaxies became clear.

The first attempt at a physical explanation for the nuclear emission of Seyfert galaxies was given in Woltjer (1959). He noted that the nuclei of these galaxies have very small angular sizes. Even for the most nearby active galaxies, the center remains unresolved, thus their size must be less than 100 pc. Woltjer also noted that 1 of 100 spiral galaxies is a Seyfert. Thus, assuming that all spiral galaxies pass through a Seyfert phase we can argue that this phase lasts $10^{10}/100 = 10^8$ years (where 10^{10} years is the age of the Universe). If the matter in the nucleus is gravitationally bound, the mass of the nucleus must be very high. This can be explained with a virial argument $M \sim v^2 r/G$. The velocity dispersion can be measured from the widths of the emission lines and

is of the order of 10^3 km s^{-1}. Since the nucleus is spatially unresolved we have an upper limit to its radius ($r \lesssim 100$ pc). Moreover, Woltjer inferred a lower limit of $r \gtrsim 1$ pc, knowing that the emission lines are characteristic of low-density gas. Thus, the mass of the nucleus can be inferred to be in the interval $M \sim 10^{9\pm1}\, M_\odot$.

Thermonuclear reactions do not produce enough energy to explain the luminosity produced. A possible explanation was provided by Salpeter (1964) and Zel'dovich & Novikov (1967), who showed that matter accreting onto compact objects could liberate up to 10% of its rest energy as radiation. After the study of Lynden-Bell (1969), the powerful emission of AGN was linked to accretion discs around SMBH. This connection was made stronger with the advent of X-ray astrophysics and the discovery of stellar-mass black holes inside the Milky Way.

The era of X-ray astronomical observation begun only in 1962, thanks to the experiment of Riccardo Giacconi, in which the existence of extrasolar X-ray sources was demonstrated (Giacconi et al. 1962). Observations at the X-ray frequencies proved to be of pivotal importance in AGN research and in the understanding of the mechanisms powering them. In fact, the X-ray emission has the fastest variability of all the wavebands in which AGN have been observed. While optical/UV radiation has a variability timescale of the order of a few days, X-rays can vary in the span of hours or even of minutes (e.g. Matthews & Sandage 1963; Mushotzky et al. 2011). This implies that the X-ray radiation originates from a very small region very close to the central engine (e.g. McHardy 1988; Elvis et al. 1994).

Moreover, X-ray emission was found to be extremely common in Seyfert galaxies (Elvis et al. 1978) and can be considered as a defining characteristic of all AGN. X-ray radiation is a major fraction of the bolometric luminosity of the AGN spanning from the 5 to 40% for a typical AGN with L $> 10^{44}$ erg/s (Ward et al. 1987; Elvis et al. 1994).

Despite more than half a century of research and thousands of publications, many questions about AGN remain unanswered. The model suggesting that AGN are powered by accreting SMBH is well established and is also supported by indirect evidence of SMBH in the Milky Way and other nearby galaxies (Rees & Mészáros 1998). However, the geometry of AGN is still debated, as well as which mechanism which disperses angular momentum from the disk allowing the disk matter to fall into the SMBH. The same holds for the physics of the disc and the production mechanism of the relativistic jets. For these reasons, the research on AGN remains an ever-expanding field and will remain such for the years to come.

1.1.1 Taxonomy of AGN

AGN is a very diverse phenomenon. Since they emit strongly over the full electromagnetic spectrum, they were discovered and classified separately at different wavelengths as technology advanced and allowed scientists to access and study them. Non-stellar signatures have a large variety of features and shapes. This has led to a large swathe of definitions that, after many years and much effort, are considered manifestations of the same underlying physical process: emission from matter nearby a supermassive black hole. Different methods of AGN classification rely on different traits, for example, the presence or absence of broad emission lines in the optical spectra, optical/radio morphology, variability, luminosity, or spectral shape. Unfortunately, the multitude of approaches intended for AGN classification makes the task complex and often

confusing. Some recognized classifications of AGN are summarized below.

- At the lower end of the AGN luminosity range there are **low-ionization nuclear emission-line region (LINER)** galaxies (Heckman 1980). They are otherwise normal spiral galaxies that show potential evidence of nuclear activity in the form of low ionization lines from the central regions. However, it is still uncertain whether all LINERs are very low-luminosity Seyfert galaxies since LINER-type spectra can also be produced in cooling flows, in starburst-driven winds and in shock-heated gas (Ho et al. 1997). Thus, the relationship between LINERs and AGN is still not clear.

- **Seyfert galaxies** are one of the largest groups of AGN, together with quasars/QSO. They are closer and less bright than quasars, and even if they have quasar-like nuclei, their host galaxy is still clearly detectable. The original definition by Seyfert (1943) was primarily morphological, i.e. they were identified as galaxies with high surface brightness nuclei. The definition has evolved so that Seyfert galaxies are now characterized by the presence of strong, high-ionization emission lines. Morphological studies indicate that most of the Seyfert nuclei occur in spiral galaxies. Khachikian & Weedman (1974) recognized that there are two distinct sub-classes of these objects: 1) Type 1 Seyfert galaxies, characterized by two sets of emission lines superimposed on one another. One set of lines is referred to as the 'narrow lines' and is characteristic of a low density (electron densities $n_e \sim 10^3 - 10^6$ cm^{-3}) ionized gas. The second set of 'broad lines' is seen in the permitted lines only. These lines have widths up to 10^4 km s^{-1}. The absence of broad forbidden lines indicates that the emitting gas has high-density ($n_e \sim 10^9$ cm^{-3}) so that the non-electric-dipole transitions are collisionally suppressed. 2) Type 2 Seyfert galaxies differ from the type 1 ones in that only the narrow lines are present in their spectra. One school of thought holds that all Seyfert of type 2 are intrinsically Seyfert 1s where we are unable to see the broad lines from our particular observation point (see below).

- **Quasars** (Matthews & Sandage 1963) include the most luminous AGN and can be defined as having nuclear magnitude of $M_B < -21.5 + 5 \log h_0$. A small minority of these sources (~5-10%) are the strong radio sources that originally defined the quasar class. The main difference between these objects and Seyfert galaxies is that in general, the host galaxy is spatially unresolved in quasars. However, many of these sources are surrounded by a low surface brightness halo ('quasar fuzz'), which appears to be starlight from the host galaxy. Other spectral differences with Seyfert galaxies are apparent in the weaker stellar absorption features and in the narrow lines being generally weaker relative to the broad lines in the spectra of quasars (Urry & Padovani 1995).

- Strong radio sources can be considered as **radio-loud Seyfert galaxies** and are typically associated with giant elliptical galaxies (e.g. Baum et al. 1993). Broad-line radio galaxies

(BLRGs) and narrow-line radio galaxies (NLRGs) are the radio-loud analogs of type 1 and type 2 Seyfert galaxies, respectively.

- AGN can show variability at every wavelength, from radio to X-ray. However, a small subset of AGN show short-time variations that are abnormally large, e.g. $\Delta m \gtrsim 0.1$ mag in the visible spectrum on time-scales as short as a day. In addition to these large and fast variations in the flux, they tend to have also variable and high polarization. This kind of AGN is called an **Optically Violent Variable** (OVV). Some properties of the OVVs are also shared by the BL Lac objects, which are also distinguished by the absence of strong emission or absorption lines in the spectra. It is believed that both OVVs and BL Lacs are AGN with a strong relativistically beamed jet component close to the line of sight. Together, OVVs and BL Lacs are referred to as 'blazars'. All known blazars are radio sources.

AGN classification still faces several challenges. First among them is the diversity in classification methods. In fact, the ways to classify AGN differ not only between different wavelengths but also within the same wavelength region. This often results in more than one classification applying to the same AGN. Secondly, classification disregards that often the properties of AGN are continuous in nature and force the objects to be cataloged into discrete bins. One of the most fitting examples is the distinction between Seyfert 1 and Seyfert 2. The strength of the broad permitted line relative to the narrow lines varies in a continuous manner, hence, the difference between Seyfert 1 and 2 is in many cases ambiguous. Therefore, Osterbrock (1977) introduced a more detailed scheme in which Seyfert galaxies are assigned the numbers 1.0, 1.2, 1.5, 1.8, 1.9, 2.0 based on the relative strength of their broad lines. Another issue of classification is given by the strong variability of AGN. In fact, AGN can present a strong variation of the spectral shape over periods from years to decades, for example changing from type 1 to type 2 (Oknyansky et al. 2018, e.g. NGC 2617). Thus, it would be wrong to assume a classification static over time. Lastly, an improvement in the observing techniques and in instrument sensitivity can contribute to classification change.

1.2 AGN structure

While AGN classification identifies the observed differences between AGN, some of the most important insights about AGN structure and nature have been gained by comparing what they have in common with each other.

Today, the aspects of AGN taxonomy are not viewed as different objects anymore but are considered to be different manifestations of the same underlying structure. This theory is called the unification theory for AGN and the underlying structure describing AGN is often referred to as the standard unification model (see Sec. 1.2.1 for more details).

It is widely thought that gravitational accretion of matter by SMBHs is the primary energy source in AGN. The detailed process by which gravitational potential energy is converted into radiation is still an argument of research.

In the standard model for AGN (see Figure 1.1), the infalling matter forms an accretion disk surrounding the SMBH. For a luminous Seyfert galaxy, the BH mass is estimated to be typically $M \approx 10^7 M_\odot$ and hence has the Scwarzschild radius $R_S \lesssim 10^{13}$cm. The region of the accretion disk emitting the UV/optical continuum is smaller than $\sim 10^{15}$ cm, while the corresponding X-ray emitting region appears to be even smaller, with a radius only a few times the Schwarzschild radius R_S.

The accretion disc has the physical size of ∼1 AU and is surrounded by an obscuring molecular torus (see Figure 1.1, the molecular torus will be discussed in Section 1.2.1). Krolik & Begelman (1988) noted that the obscuring torus must be composed of individual very optically thick dusty clouds. This observation was subsequently confirmed by an interferometric analysis of the Circinus galaxy that supported the evidence of a cloudy or filamentary dust structure around the central AGN (Tristram et al. 2007).

Above the SMBH and the accretion disc, clouds of reprocessing material are located around the SMBH. The closest clouds have higher velocities hence the optical lines emitted in that region are broader, giving it the name broad-line region (BLR). The lines emitted by the clouds far from the SMBH are narrower since the clouds are slower, hence giving them the name narrow-line region (NLR). The type of AGN spectrum observed depends on the inclination of the disk relative to the observer (see Section 1.2.1).

1.2.1 Orientation-based AGN unification scheme

The efforts to create a unification scheme for AGN started in the 1970s stimulated by the development of very long baseline interferometry (VLBI) techniques and by the discoveries of anisotropies induced by gas and dust in optical and X-ray observations. Radio-quiet and radio-loud AGN were treated separately until the end of the 1980s when an effort to reconcile the two cases was made. Some milestones in the establishment of the unification theory are the works of Rowan-Robinson (1977), that observe that Seyfert 2 show enhanced extinction compared with Seyfert 1 galaxies, and the pioneering work of Antonucci (1984), that contains the first tentative description of an obscuring circum-nuclear torus, that is now one of the key elements of the unification scheme (see Section 1.2) (Lawrence & Elvis 1982).

To summarise, by the beginning of the 1990s it was recognized that beaming by relativistic jets and obscuration by optically thick regions surrounding the AGN could produce the anisotropy necessary to cause the appearances of an AGN to vary with the orientation of the observer with respect to the line of sight. Thus, the type of AGN spectrum observed depends on the inclination of the disk relative to the observer. If the disk has a low inclination, it will be viewed face-on, hence the observer can see the BLR and the spectrum will show broad optical lines. If the inclination is higher, the BLR will be obscured by the molecular torus, hence the spectrum will have narrower lines (Antonucci 1993; Urry & Padovani 1995). This way, anisotropic obscuration can explain the difference between Seyfert 1 and 2. It also became clear that to unify all the different states of radio-loud AGN it was necessary to combine the two sources of anisotropy.

Hence, in the orientation-based unification scheme, in a Seyfert 2 spectrum we only see narrow emission lines because the system is oriented in such a way that the obscuring torus obscures the BLR. Seyfert 1, on the other hand, would be more face on with respect to the

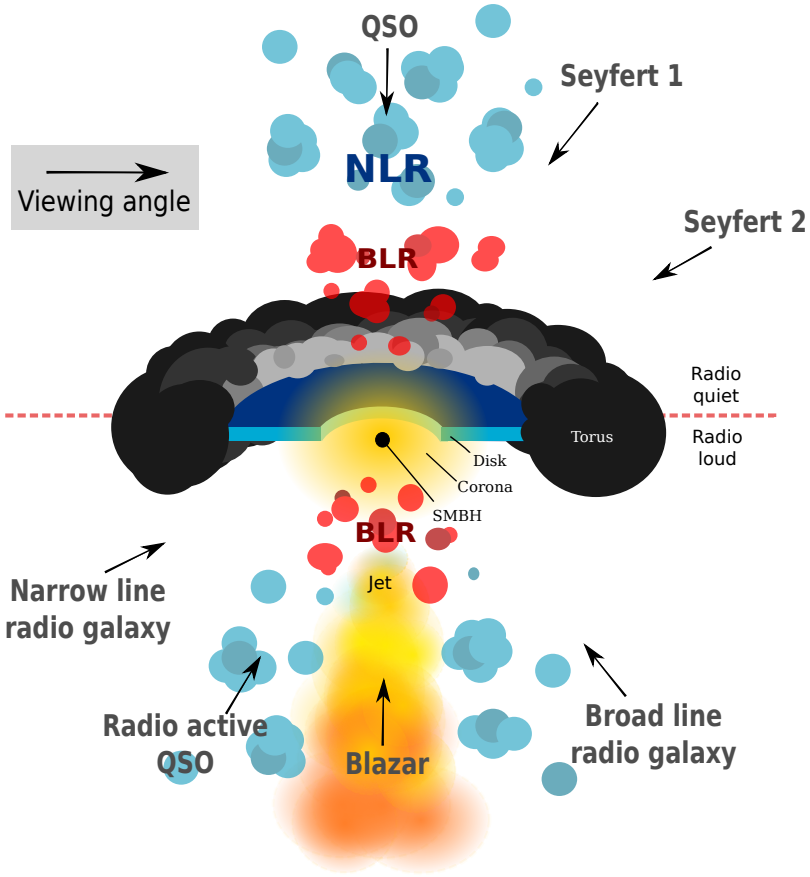

Figure 1.1: Standard unification scheme of AGN. The emission of an AGN can be explained by matter accreting onto a SMBH. The matter is arranged as an accretion disc around the central engine. This structure is enclosed by an obscuring molecular torus. Rapid AGN variability overall wavelengths suggest that this whole structure is only a few parsecs in radius. Around the central engine of AGN, there are zones of gas and dust. The clouds located closer to the SMBH have larger velocity, thus they emit broader emission lines, and are referred to as the broad line region (BLR). Further away clouds have lower velocities, hence their emission lines are narrower, therefore the name narrow-line region (NLR). Different classes of AGN can be explained by different orientations of the disc and obscuring torus with respect to the line of sight. In the case of radio-loud AGN, more anisotropy is introduced by the relativistic beaming in the radio jet. Deviations from this model are described in Section 1.2.1. (Image adapted from Urry & Padovani (1995) and produced with Inkscape)

observer, so that also the emission lines from the BLR are seen. Similarly, QSO would be AGN observed directly face-on, so that less radiation is absorbed. The work of Antonucci & Miller (1985) provides supporting evidence to this theory. The authors noticed that the polarized emission from NGC 1068, an AGN classified as Seyfert 2, showed evidence of faint broad lines buried under the much stronger narrow lines. The broad lines must be scattered into the line of sight. while being obscured from direct view.

In the case of radio-loud AGN, the greater radio luminosity of quasars could be explained by Doppler boosting of a jet pointing in the direction of the observer, magnifying the emission.

Hard X-ray observations (> 2keV) provided further proof of the unification model. Seyfert galaxies in the X-ray are characterized to first order by a power-law spectrum, denoting the presence of common powering mechanisms in both Seyfert 1 and 2. Even if the obscuration in the X-ray and in the optical wavelength does not seem to be always correlated, most Seyfert 2s are generally much weaker in the soft X-ray (< 2keV) due to a photoelectric absorption cut-off demonstrating the presence of an obscuring medium along the line of sight.

Early models proposed a toroidal and optically thick obscuring torus (Antonucci 1993). However, one of the main problems of this model is the dynamical stability (Elitzur 2007). Some solutions were suggested, for example, radiation pressure from IR photons could contribute to keeping the torus geometrically thick. So could supernovae and stellar winds. Recently, the hypothesis of a uniform gas distribution has been modified in favor of a torus model presenting a clumpy structure (Krolik & Begelman 1988).

The clumpy torus model leads to several issues whit the idea that assumes the viewing angle as a sole attribute for AGN classification. In fact, the clumpiness of the molecular torus (Krolik & Begelman 1988) implies that AGN of the same luminosity can have different shapes of tori and the difference between Seyfert 1 and 2 becomes the probability of viewing the central source directly (Elitzur 2008; Nenkova et al. 2008). This means that there is a non-zero probability of detecting a Seyfert 1 also with inclinations that would typically result in Seyfert 2 spectra. There is also evidence of a further sub-category among the Seyfert 2 galaxies that display higher X-ray obscuration and a much stronger reflection than the Seyfert 1 and less obscured Seyfert 2 galaxies (Ricci et al. 2011). This might be explained by a molecular torus covering a larger fraction of X-ray photons. According to this, AGN classification does not only depend on orientation but also on the covering factor of the molecular torus, which is an intrinsic, observer-independent property (Elitzur 2012).

In another possible scenario for the unification scheme, the BLR and the molecular torus are part of a continuous distribution of clouds (Elitzur 2007). All clouds are embedded in a disk wind with intensity proportional to the accretion rate (thus, luminosity). Hence, by decreasing luminosity, $L < 10^{42}$ erg/s, the molecular outflow would decrease until the torus disappears so that only Seyfert 1 type spectra would be detected. If the luminosity decreases further, even the BLR disappears and only Seyfert 2 type spectra are observed (Elitzur 2006).

However, other studies find that higher luminosity AGN ($L > 10^{42}$ erg/s) are in general less obscured. The stronger radiation emission of high luminosity AGN may cause the dust particles in the torus to sublimate, hence reducing the obscuration.

1.3 The Black Hole paradigm

Stronger evidence for supermassive ($M > 10^7 M_\odot$) object at the center of galaxies has emerged from dynamical studies of gas in the core of M87 (e.g. Korista et al. 1995), radio observation of Sgr A* (Balick & Brown 1974) and from megamaser kinematics in M106 (Miyoshi et al. 1995). The SMBH scenario is also supported by the observation of very broad, gravitationally redshifted X-ray emission lines in MCG-6-30-15 (Tanaka et al. 1995).

The fascinating properties of black holes (BH) have captured the imagination of scientists since the 18th century when John Michell and Pierre-Simon Laplace theorized objects whose gravitational field is too strong for light to escape (Montgomery et al. 2009). However, these objects were considered to be mere mathematical curiosity, even when Karl Schwarzschild in 1916 found the first solution of general relativity (GR) to characterize a BH (Schwarzschild 1999). It was only later, thanks to pioneering work of Chandrasekhar (Chandrasekhar 1931, 1984), that Oppenheimer & Volkoff (1939) and Oppenheimer & Snyder (1982) demonstrated that BH represent the collapsed state of sufficiently massive stars.

BH is described by GR as gravitational singularities, which are extreme cases of curved space-time where the gravitational field is so strong that not even light can escape (Wald 1984). They are defined by the event horizon, the radius at which the escape velocity from the BH is equal to the speed of light. BH does not emit light themselves but we can observe them indirectly thanks to the electromagnetic radiation produced by the matter they accrete (Misner et al. 1973; Shapiro et al. 1983; Hartle 2003).

The only properties that a BH can posses are mass, angular momentum, and charge (no-hair theorem) (Misner et al. 1973; Heusler 1998; Chruściel et al. 2012). The BH mass determines how much the space around them is warped, while the BH spin determines the degree to which the space-time is twisted. However, electrical charge, despite being a relevant property for BH in a vacuum, can be neglected for astrophysical BHs. In fact, the eventual charge of astrophysical BH can be neutralized by accreting plasma of particles of the opposite charge or by charge separation (Reissner 1916; Zajacek & Tursunov 2019).

As mentioned above, assuming standard GR, BHs can be described completely by three fundamental properties: (1) mass, (2) spin, and (3) electric charge. We assume the electric charge to be negligible as the BH in a non-vacuum environment would rapidly accrete particles of the opposite charge and neutralize itself. Moreover, the BH is believed to dominate the gravitational potential up to at least $10^5 M$. Hence, we can assume that the space-time is characterized by the Kerr metric (Kerr 1963) and that the mass M and the dimensionless spin parameter $a = Jc/GM^2$ are the only two necessary features to describe an astrophysical BH (Kerr 1963). Using Boyer-Lindquist coordinates, we write the Kerr line element as

$$\begin{aligned} ds^2 = &-\left(1 - \frac{2Mr}{\Sigma}\right) dt^2 - \frac{4aM^2 r \sin^2\theta}{\Sigma} dt d\phi + \frac{\Sigma}{\Delta} dr^2 \\ &+\Sigma d\theta^2 + \left(r^2 + a^2 M^2 + \frac{2a^2 M^3 r \sin^2\theta}{\Sigma}\right) \sin^2\theta d\phi^2, \end{aligned} \tag{1.1}$$

where $\Delta = r^2 - 2Mr + a^2$ and $\Sigma = r^2 + a^2 M^2 \cos^2\theta$. In the case where $a = 0$, the Schwarzschild

metric (Schwarzschild, 1916) is obtained

$$ds^2 = -\left(1 - \frac{2M}{r}\right)dt^2 + \left(1 - \frac{2M}{r}\right)^{-1} dr^2 + r^2\left(d\theta^2 + sin^2\theta d\phi^2\right). \tag{1.2}$$

From equation 1.1 one can see that in the Kerr metric are present two singularities, i.e. when $\Sigma = 0$ or when $\Delta = 0$, where $\Sigma = 0$ is a true curvature singularity of the manifold, while $\Delta = 0$ is a coordinate singularity.

The surface defined by $\Delta = 0$ represents the event horizon, which is a region in space-time beyond which events cannot affect an outside observer. The radius of the event horizon is found by solving the equation $\Delta = 0$ and given by $r_\pm = M \pm \sqrt{M^2 - a^2}$. It can be seen that there are no real solution when $a^2 > M^2$, posing the limiting value for the spin $|a| < M$ or $|a_*| < 1$ (for $a_* = a/M$). In a case where $a^2 > M^2$, the singularity $\Sigma = 0$ is not covered by any horizon (naked singularity) leading to paradoxes in our Universe.

It is convenient to rephrase the basic properties of a BH of mass M as expressions of its gravitational radius r_g defined as

$$r_g = \frac{GM}{c^2}, \tag{1.3}$$

where G is the gravitational constant and c is the speed of light in vacuum.

All properties of non-rotating (Schwarzschild) BHs can be defined using r_g. However, for rotating (Kerr) BHs we need to define one other attribute: the angular momentum of the BH

$$J \sim I\Omega \sim Mr_g^2\frac{v}{r} \sim Mr_g c, \tag{1.4}$$

where Ω is the angular velocity at the horizon and J is the specific angular momentum of the BH. It is convenient to define the BH spin a such as the specific angular momentum, J/M of the BH is expressed as

$$J/M = ar_g c. \tag{1.5}$$

This shows that the spin $a := cJ/GM^2$ can take all the values between 1 and -1. Negative spin values represent retrograde configurations, where the BH spins in the opposite direction to the accretion disk, while positive spin values denote prograde spin configuration, where BH and accretion disk rotate in the same direction. The spin determines the maximum energy that can be extracted from a BH during accretion (see Section 1.3.2).

The spin is one of the most challenging BH property to measure because it requires probing radiation emitted at a few gravitational radii from the SMBH. The angular momentum of a BH is manifested through Lense-Thirring precession, also known as frame-dragging. This occurs in the innermost radii of the accretion disk, where relativistic effects torque the space-time in the same direction of the BH rotation. This region of the accretion flow is known to emit strongly in the X-ray. For this reason, one of the best tools to probe the region of the disc so close to the SMBH is X-ray spectroscopy (Oda et al. 1971; van der Klis 1995).

The real existence of BH in the Universe was doubted by many, including Albert Einstein himself. However, in the second half of the 20th century, this view began to change, after astrophysical BH candidates were unambiguously detected within our Galaxy. These discoveries

were recently corroborated by the direct observation of the SMBH in the core of M87 by Event Horizon Telescope (EHT).

Today, it is believed that in a typical galaxy there are millions of BH candidates, ranging from several $M_\odot$ for stellar remnants to $10^6 - 10^{9.5}\ M_\odot$ for BH in galactic nuclei.

Accreting SMBHs in galactic centers have been known since the 1960s when the first QSO was detected (Salpeter 1964; Zel'dovich & Novikov 1967). However, the concept that every galaxy contains a SMBH in their center is much more recent. The existence of such objects was suggested by detailed studies of stellar velocity fields and gas motions in about 60 nearby galaxies (Magorrian et al. 1998).

1.3.1 SMBH growth

Since the discovery of stellar-mass BH in the Milky Way and the realization that all massive galaxies host a SMBH in their core researchers have worked to understand their growth (Kormendy & Richstone 1995; Magorrian et al. 1998; Gebhardt et al. 2000).

SMBHs can either grow by accreting surrounding gas and dust (Lynden-Bell 1969; Soltan 1982; Shankar et al. 2009) or by merging with other SMBHs (e.g. Volonteri et al. 2013).

Accretion onto a BH is believed to be largely "scale-free". Thus, the mode of accretion is determined by the ratio of the mass supply rate to the Eddington rate $\dot{M}_E = 4\pi GM/\kappa_T c$ (see Section 1.3.2) and the product of the angular velocity Ω of the BH and its mass M.

If SMBH growth is dominated by BH-BH mergers we will find a population of moderately spinning SMBH. However, gas accretion as the dominant growth mechanism leads to a population of rapidly-spinning or slowly-spinning SMBHs. The population will have high or low spin depending on whether the accreting matter maintains a coherent angular momentum vector over the time it takes to double the BH mass (Volonteri et al. 2003, 2005).

Thus the spin of SMBH in active galactic nuclei (AGN) can reveal the relative role of gas accretion vs. mergers in recent epochs of the life of the AGN and ultimately clarify the formation pathways and growth history of these objects (Berti & Volonteri 2008). Moreover, spin measurements offer a probe of the nature of space-time in the regions closer to the event horizon of the SMBH, well within the strong-gravity regime (Fabian et al. 1989; Laor 1991). SMBH spin could be the source of large amounts of energy, thus it could explain the relation between BH angular momentum and the powerful relativistic jets produced by many BH systems.

For these reasons, measuring the spin distribution in a population of AGN is of critical importance to understand how galaxy form and to evolve over cosmic time (Berta et al. 2008).

1.3.2 Basic physics of accretion

The energy produced by accretion is given by $E = \eta Mc^2$, where η is the efficiency factor of the process or radiative efficiency (Rees 1984; Laor & Netzer 1989). The luminosity over the full electromagnetic waveband, the bolometric luminosity L_{bol}, can then be defined as $L_{bol} = \eta \dot{M} c^2$, for a BH of mass M and accretion rate $\dot{M} = dM/dt$. The radiative efficiency η varies between 5.7% for the no spin case to 32% for the maximum plausible spin (Thorne 1974). For

comparison, the radiative efficiency for nuclear reactions is 0.7%[1] while the one for chemical reactions is 10^{-10}. Hence, the release of gravitational energy as radiation during accretion onto a SMBH is one of the most efficient processes of conversion of matter to radiation in the Universe, after the matter-antimatter annihilation (Frank et al. 2002).

Since photons have a momentum $p = h\nu/c$ we can expect radiation pressure to be exerted outward on the matter surrounding the BH. For a central source with luminosity L and flux F at a distance r and considering that the interaction between a photon and an electron is the Thomson cross section $\sigma_T = 6.65 \times 10^{-25}$ cm^2, the radiation pressure P can be calculated as

$$P = \frac{\sigma_T}{c} F = \frac{\sigma_T L}{4\pi r^2 c}, \tag{1.6}$$

assuming spherical geometry and that electrons and protons are fully electrically coupled (otherwise there would be huge electrical fields). The gravitational force GMm_p/r^2, where m_p is the proton mass, also scales with a factor r^{-2}. Hence, there is a maximum luminosity achievable via accretion, also called Eddington luminosity or Eddington limit (L_{Edd}), that represents the balance between gravitational pull from the BH and the radiation pressure from Thomson scattering of the electrons, and is given by

$$L_{Edd} = \frac{4\pi G c M m_p}{\sigma_T} \approx 1.26 \times 10^{38} \left(\frac{M}{M_\odot}\right) erg/s. \tag{1.7}$$

When the luminosity of the BH exceeds the Eddington limit the radiation pressure is larger than the gravitational pull and the gas surrounding the SMBH is blown away halting the accretion. Therefore, steady spherical accretion can occur only if the emitted luminosity is below the Eddington limit (Bondi 1952).

1.3.3 Accretion disc theory

When the accretion flow has an angular momentum with respect to the central SMBH, the gas cannot accrete directly as described by Bondi (1952). Accretion onto BH is believed to occur via an accretion disc, were gravitational energy and angular momentum can be efficiently dissipated and eventually converted into radiation (Shakura 1972; Shakura & Sunyaev 1973). If the specific angular momentum of the accreted gas exceeds $\sqrt{12} r_g c$, then the gas has to dissipate part of the angular momentum via viscous torques in order to cross the event horizon (Begelman 1985).

Thus, viscous processes between different rings in the accretion disc would cause some drag and part of the binding energy of the disc would transform into local heating of the rings or it would be radiated away and this would allow the angular momentum to be transferred outward (Pringle & Rees 1972; Shakura & Sunyaev 1973).

An accretion that radiates away most of its binding energy has the shape of a geometrically thin disc, i.e. its height is much smaller than its radius (Novikov & Thorne 1973; Page & Thorne 1974). This results in a stationary inflow falling into the SMBH with accretion rate $\dot{M}$ after completing a set of Keplerian circular orbits with zero-torque boundary condition at the innermost

[1]The efficiency for nuclear fusion is calculated as $\eta = (4m_p - m_\alpha)/(4m_p) = 0.007$, where m_p is the proton mass and m_α is the mass of the He nucleus.

radius of the disc, usually located at the innermost stable circular orbit (ISCO), also referred as marginally stable orbit (Pringle 1981).

To complete the solution of the disc structure we need to further assume that the viscosity is proportional to sound speed (Frank et al. 2002).

This disc model radiates locally in the form of black body (BB) radiation. The flux as a function of the radius and the temperature of the disc can be calculated knowing the mass of the SMBH, M_{BH}, the spin, a, and the accretion rate $\dot{M}$.

(Capellupo et al. 2015) showed that this relatively simple model fits several SEDs of AGN nicely. However, several unsolved issues about the accretion disc model still stand.

For example, molecular viscosity that allows the passage of molecules from the faster ring to the slower rings is too weak to explain the large luminosity of accretion discs (Lawrence 2018). Thus, from 1970 on, it was assumed that the angular momentum transfer was occurring thanks to viscosity-like effects, such as magnetic stresses and/or turbulence. Already Shakura & Sunyaev (1973) assumed an undetermined combination of the two effects, however, the idea was definitely accepted in 1991 with the development of the magneto-rotational instability theory (MRI, Balbus & Hawley 1991). This theory explains nicely the luminosity and compactness of AGN, however, it has difficulties in explaining some characteristics of the big blue bump in the UV and especially AGN variability. For example, AGN appears to be cooler than it ought to be (temperature problem) and the broad range of emission lines shown in an AGN spectrum cannot be explained by the energy produced into a theoretical accretion disc (ionization problem). However, these issues can be explained by effects that modify the AGN spectral energy distribution (SED), such as a system of clouds surrounding the disc or Comptonizing atmosphere (for a more detailed review, see Lawrence 2012).

AGN variability poses a more problematic issue. First of all, the emission from AGN varies significantly with timescales from months to days, whereas this should not be possible in a disc with viscosity high enough to explain the emitted luminosity. In fact, the expected optical variability from a viscous disc should change only over thousands of years. Secondly, different UV/optical wavelengths vary simultaneously, but in an accretion disc, different wavelengths come from different radii, thus changes should get propagated through the disc and for this reason one should be able to observe a lag between them (e.g. Clavel et al. 1991; Crenshaw et al. 1996; Edelson 2000). A possible solution to this problem is given by X-ray reprocessing (Clavel et al. 1992). The X-ray source shines on the disc and heats it and since X-ray radiation of an AGN has larger variability than the optical one the X-ray heating varies faster than the heating due to viscosity. The observations of delays explainable with light travel time delays between the variations at different wavelengths play in favor of this theory (Edelson et al. 2015; McHardy et al. 2016). In addition to this, the frequent observation of extreme variability, where the emission changes of a factor of several over a few decades, further complicate the issue. These large changes do not only occur in the UV or X-ray wavelengths but also in the optical, suggesting that also the outer radii of the discs undergo rapid physical changes inconsistent with viscous heating.

Since the idea of variable obscuration to explain these outburst does not really fit the data, it seems like we have to accept the fact that the viscous accretion disc theory is too simple. However, authors still assume that the standard theory is correct and the outburst can be explained

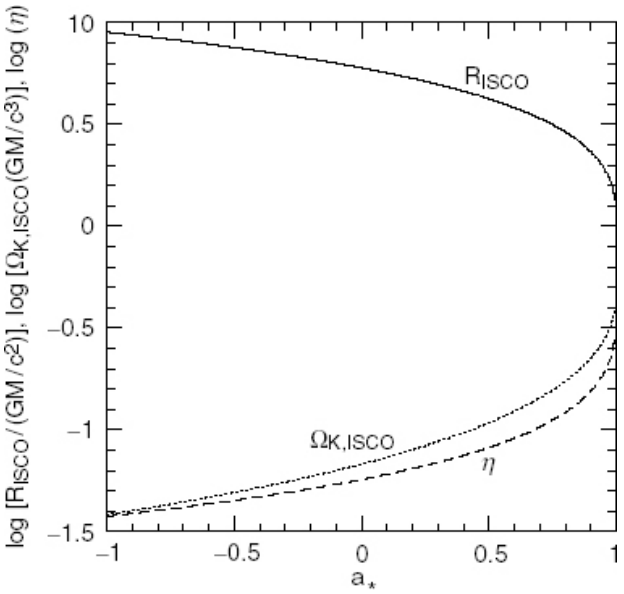

Figure 1.2: Variation of the radius of the innermost stable circular orbits (R_{ISCO}), the Keplerian frequency (Ω_{ISCO}) and the binding energy (η) at this radius for different values of the spin $a_\star$. (Image from Narayan (2005))

by "disc instabilities".

For this reason, alternative theories to explain AGN accretion flows are starting to appear. The simplest of these theories assume that an accretion disc is present but it has low viscosity and it is cold unless heated externally by another source. In this scenario, all energy is radiated as UV and X-ray by a central quasi point-like source and heats the passive disc. this region could be explained for example by an inner region in spherical accretion or by an inner viscous disc. Even if this theory seems to explain the light travel time delays observed in some AGN, it still has issues modeling the peak of the SED.

Alternatively, the loss of angular momentum and the heating of the disc might be explained by non-local processes. For example, we could have large magnetic-fields causing one ring to drag on a distant one, or corkscrew-like processes carrying the angular momentum away (for a review, see Rees 1984). However, most of these theories are complicated and hard to test, thus, the answers to the open questions on accretion discs still lay in the future.

1.3.4 How to measure BH spin

Most of the methods to measure BH spin rely on the dependence of the ISCO on the spin parameter a. The ISCO, with the designated radius R_{ISCO}) is a key concept for spin estimation. In fact, the radius R_{ISCO} varies strongly for different values of the spin a (see Figure 1.2). For example, a maximally spinning SMBH with matter rotating in the same direction (co-rotating) as the BH spin (a = +1) will have $R_{ISCO} = GM/c^2$. In the case where the accreting matter is rotating in the opposite direction (counter-rotating) as the BH spin (a = −1) the radius will be $R_{ISCO} = 9GM/c^2$,

while in the case of a Shwartzschild non-spinning BH (a = 0) we have $R_{ISCO} = 6GM/c^2$ (Narayan 2005). Thus, measuring the R_{ISCO} leads to the constrain of the SMBH spin.

Here below, are reported five methods to measure BH spin (see also (Brenneman 2013)):

- **Thermal Continuum Fitting** (Remillard & McClintock 2006): this method determines the inner radius (ISCO) of the accretion disk by fitting the thermal continuum spectrum of the accretion disk. The method has been primarily applied to stellar-mass BH.

- **High-Frequency Quasi-Periodic Oscillations** (e.g. Strohmayer 2001; Erkut 2011): the X-ray power density spectrum is characterized by 1-2 pulses at some harmonic frequencies indicative of resonance or periodic oscillation within the accretion flow. The frequency of these oscillations is related to the frequency of the ISCO. Hence, potentially the radius of the ISCO could be measured and the BH spin inferred. Such a phenomenon has been reported in accreting stellar-mass BH, but only once in AGN (Gierliński et al. 2008).

- **X-ray Polarimetry** (e.g. Tomsick et al. 2009): as expected by Shakura & Sunyaev (1973), the inner reflection from a geometrically thin accretion disk is expected to be polarized. The characteristic shape of the degree and angle of the observed polarization depends on the spin of the BH due to frame dragging and to the position of the ISCO. However, there is currently no active or planned mission to launch an X-ray polarimeter in space.

- **Imaging the Event Horizon Shadow** (Broderick et al. 2011): the innermost accretion disc can be directly imaged with sub-mm Very Long Baseline Interferometry (VLBI) with micro-arcsecond spatial resolution. The spin of the BH can be constrained by comparing the images with models of the appearance of the innermost disk. An image of M87 was produced last year using this technique (Event Horizon Telescope Collaboration et al. 2019). Soon, the technique will be extended to Srg A*.

- **Inner Disk Reflection Modeling** (e.g. Brenneman & Reynolds 2006): The X-ray emission in AGN arises when optical/UV photons from the disc are reprocessed by a hot corona of Comtonizing electrons surrounding the BH. Since the emission is produced in the innermost region of the accretion flow, the features contained in X-ray spectra from AGN can be directly used to measure BH spin (see Section 1.4).

The latter is the technique used in this thesis, so here we explore AGN X-ray emission in more detail.

1.4 AGN in the X-ray

Why are X-rays so appropriate to study AGN? X-rays provide a clean diagnostic of nuclear activity in the galaxies since emission from stellar processes is relatively weak at these wavelengths. They are relatively unaffected by obscuration and they are less contamination from non-AGN sources than IR radiation, allowing a census of accretion events over a wide obscuration interval

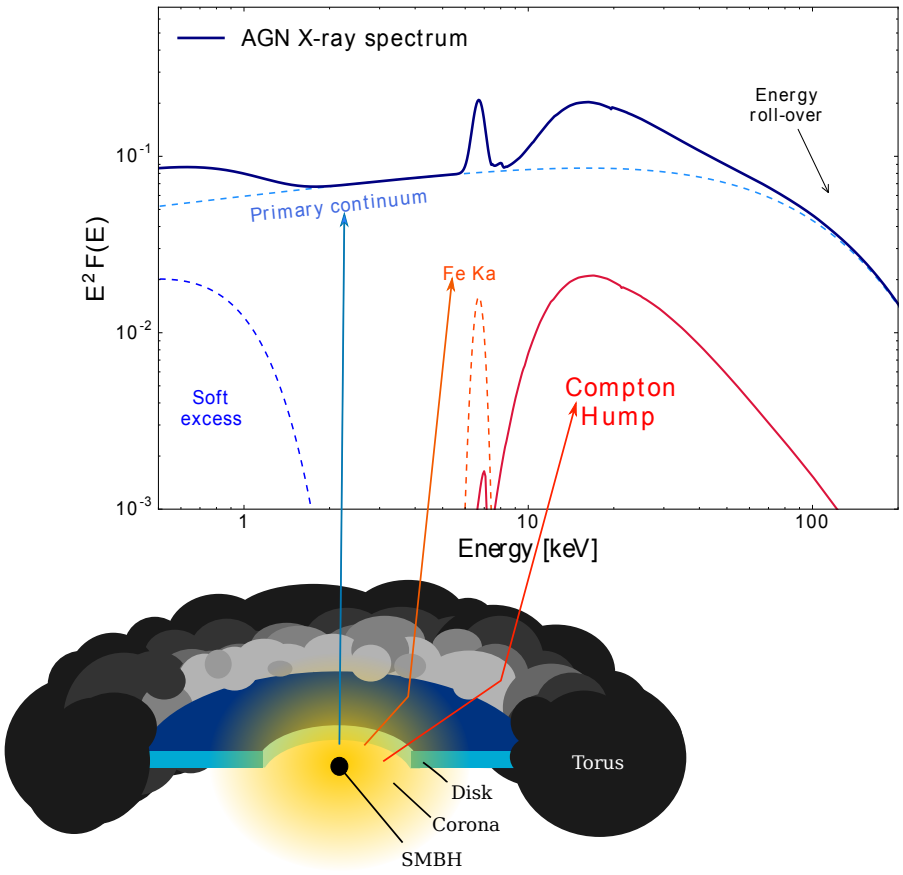

Figure 1.3: Structure of an AGN showing which feature of the X-ray spectrum is produced in which region. The accretion disc emits photons at optical and UV wavelengths. These disc photons are then inverse Compton scattered by a corona of hot electrons surrounding the SMBH. The inverse Compton scattered photons from the primary X-ray continuum with the shape of a power-law. Part of this emission shines over the accretion disc and the molecular torus and gets reflected and reprocessed. The reflection component presents two main features. A prominent fluorescent iron Kα line and, when the reprocessing material is Compton thick ($N_H > 10^{24} cm^{-2}$), a Compton hump, in the harder X-ray spectrum (>10 keV) peaking around 20 keV. The power-law continuum shows a high energy rollover located at a few hundred of keV depending on the temperature and optical depth of the hot electron plasma composing the corona. Many AGN often show an excess in the softer X-ray (< 2 keV). Attenuation of the X-rays is due to two different mechanisms: photoelectric absorption and Compton scattering. (Image produced with Inkscape.)

(Steffen et al. 2003). Hence, compared to other wavelengths, X-rays provide a more representative view of accretion events at any given cosmic time (Mushotzky 2004). Moreover, X-ray observation are of great importance to understand the AGN phenomenon, since X-ray emission account for $\sim 3-20\%$ of the bolometric luminosity of AGN (Ho 1999) and their rapid variability indicates that X-rays probe the innermost regions of AGN (Elvis et al. 1978).

One commonly accepted model for X-ray production states that the primary X-ray emission from AGN arises from optical/UV photon (green arrows in Fig. 1.4) inverse Compton scattered by a corona of hot and relativistic electrons situated above the SMBH. This Comptonized emission has the shape of a power-law (cyan arrows in Fig. 1.4), of the form

$$P_E(\text{photons s}^{-1}\ \text{keV}^{-1}) = AE^{-\Gamma}, \tag{1.8}$$

where P_E is the number of photons emitted per unit time and energy, with a photon index of typically $\Gamma \sim 1.8-2$ (Nandra et al. 1997a; Dadina 2008). The power-law continuum shows in most cases an high energy roll-over located at a few hundred keV. This feature is mainly related to the temperature of the electron plasma in the corona.

There are several possible scenarios to describe the nature and the morphology of the corona (see Figure 1.4). In the lamp-post model, the corona is a point-like source hovering above the SMBH along its spin axis (see Niedźwiecki et al. 2016, andreferences therein). This configuration could arise for example at the base of a jet (Vincent et al. 2016). If the corona would instead form in the atmosphere of the disc we would then observe a sandwich corona. A spherical or toroidal corona could be created from the accretion flow from the disk to the BH (Bambi 2017). A lag between the bands dominated by the primary power-law and those associated with the reflection is observed in many Seyfert galaxies. The mapping of this phenomenon, called reverberation, might be a key tool to distinguish between the different geometries (Peterson 1993).

Part of the primary power-law reaches the observer directly, while part of it is reflected and reprocessed by the accretion disk and the molecular torus (see Section 4.4 and orange arrows in Fig. 1.4). The reflected radiation consists mainly of two features: the Compton hump peaking at $\sim 20-30$ keV and the iron (Fe) Kα line at 6.4keV in the rest frame (see Section 1.4.2) (Lightman & White 1988; Pounds et al. 1990). The Compton hump becomes noticeable only when the material surrounding the SMBH is Compton thick ($N_H > 10^{26}\text{cm}^{-2}$), while the Fe K$\alpha$ line can be produced also by Compton thin material (Guainazzi et al. 2005; Fabian 2006).

Whereas most of the X-ray emission can be identified as arising in the spatially unresolved nucleus, several Seyfert galaxies show extended structures in the soft X-ray (0.1–2 keV) (e.g. Elvis et al. 1990; Wilson et al. 1995). The origin of this emission is not well understood, however, plausible theories include electron-scattered nuclear light and thermal bremsstrahlung from hot gas.

1.4.1 X-ray reflection and absorption

The basic mechanism of X-ray reflection can be explained by assuming that the hard power-law X-ray continuum illuminates a semi-finite slab of cold gas (the disk). In this case, the term "cold" means that metal atoms are generally neutral while H and He are mostly ionized (George

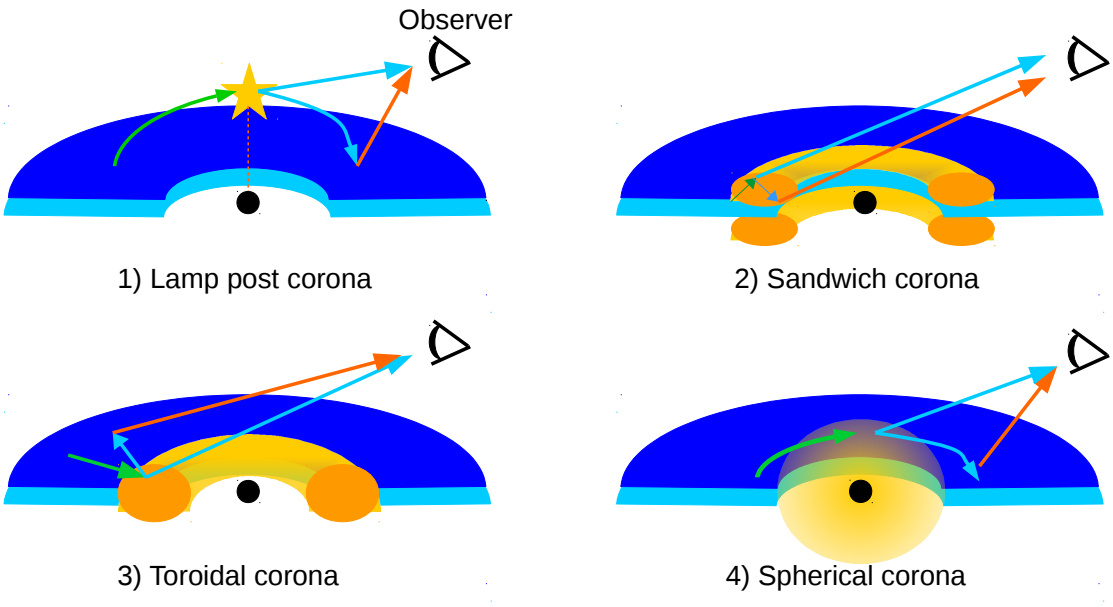

Figure 1.4: Examples of possible corona geometries: lamp post geometry (*top left*), sandwich (*top right*), toroidal (*bottom left*) and spherical (*bottom right*). (Image adapted from Bambi (2017) and produced with Inkscape.)

& Fabian 1991; Matt 2002). When a continuum photon enters the slab there are a number of possible effects arising: Compton scattering by free or bound electrons, photoelectric absorption with consequent fluorescent line emission, or Auger de-excitation. Incident soft X-rays are usually absorbed, due to the energy dependence of photoelectric absorption, while hard X-rays are absorbed only at higher obscuration and tend to be Compton scattered and leave the slab. Hence, the reflection component is a factor of $\sim \sigma_T/\sigma_{pe}$ lower than the incident spectrum, where σ_T is the Thompson cross-section and σ_{pe} is the photoelectric cross-section.

Above energies of ~20 keV Compton recoil reduces the backscattered X-ray flux. This gives the reflection component above 10 keV a broad hump-like shape sometimes referred to as the Compton-hump, which starts to dominate over the primary continuum, when the latter is strongly absorbed in the harder X-ray. The absorption of X-ray with energies 10 keV and above requires extreme column densities of $N_H > 1.5 \times 10^{24}$ atoms /cm^2. AGN showing these large levels of obscuration are labeled as Compton thick AGN (see Comastri 2004, for a review).

The reflection component provides us with information about the geometry, composition, ionization state, and temperature of the accretion disk (Reynolds 1999).

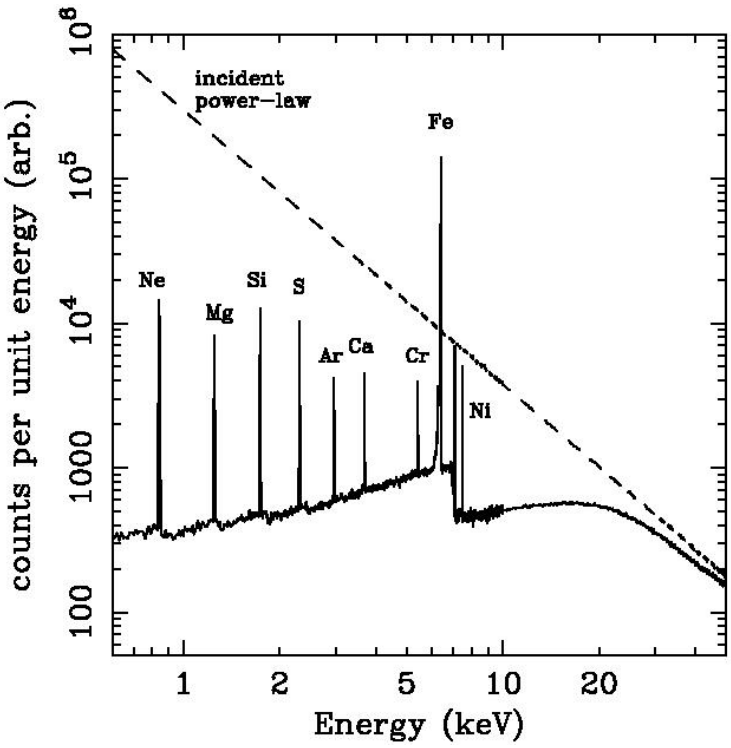

Figure 1.5: X-ray reflection spectrum of AGN. The dashed line represents the incident spectrum, while the solid line shows the reflected component integrated over all angles. From Monte Carlo simulation by Reynolds (1996) based on calculations from George & Fabian (1991).

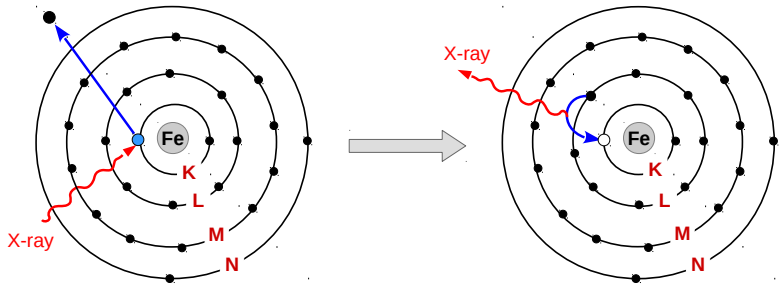

Figure 1.6: The Kα transition for iron occurs when an energetic X-ray photon ejects an electron from the Fe K-shell. A photon at 6.4 keV is then emitted when an electron from the L-shell fills the hole left by the K-shell electron. (Image produced with Inkscape.)

1.4.2 The Fe Kα line

The fluorescence Fe Kα line is emitted when an X-ray photon hits a K-shell electron of an iron atom and ejects it from its orbital. An L-shell electron will then fill the hole left by the K-shell electron releasing a ~6.4 keV photon (e.g. Yaqoob & Padmanabhan 2004) (See Figure 1.6) or in some cases, transferring energy to another electron and ejecting it from the atom (Auger electron). The analoge of the Fe Kα in hydrogen is Lyman α, however, due to the small nuclear charge of hydrogen, this line is in the UV and not in the X-ray range. The Kα line is by far the strongest X-ray line of any element in the reflection spectrum of AGN. The Kα line is actually a doublet, where the slight energy difference of the Kα_1 at 6.391 keV and Kα_2 at 6.404 keV depends on the spin-orbit interaction energy between the electron spin and the 2p orbital momentum (Roseberry & Bearden 1936; Fabian et al. 2000). However, modern X-ray satellites do not have sufficient spectral resolution to distinguish the doublet, hence I will continue to refer to the Fe Kα feature as a single line. The only exception was the satellite *HITOMI* (Hitomi Collaboration et al. 2016), which unfortunately underwent catastrophic failure in March 2016.

In ionized Fe atoms, the outer electrons are less successful in blocking the effects of the nuclear charge on the inner shell electrons, therefore both the energy required to free a K-shell electron and the energy needed to emit a Kα line is increased (You et al. 2003), although the Fe Kα line energy is significantly above 6.4 keV when the M-shell electrons are lost (i.e. FeXVII and higher states). The probability that the photoelectric event is followed by fluorescent emission rather than an Auger effect is called the fluorescence yield and is a weak function of the

ionization state from neutral Fe (FeI) to FeXXIII. From Lithium-like to Hydrogen-like Fe atoms (FeXXIV to FeXXVI) the absence of more than two electrons from the L-shell means that the Auger effect can not occur. For FeXXV and FeXXVI ions, the fluorescence line is produced when a free electron is captured by the atom (recombination) (Matt et al. 1997). For neutral Fe atoms, the fluorescence yield is proportional to the atomic number to the power of four ($\propto Z^4$), making the Fe Kα emission particularly strong (Fabian et al. 1989; Matt et al. 1997; Fabian et al. 2000). For cosmic abundances of Fe, the optical depth of bound-free Fe absorption is close to the Thomson depth. Hence, the Fe Kα line production of an X-ray irradiated slab takes place in the outer Thomson depth. This is only a fraction of the total thickness of the slab (0.1% to 1%) and depends on the ionization state of the gas in this thin region(Fabian et al. 2000).

Fe Kα is an intrinsically narrow line, with energy with ~3.5 eV (Laor 1991; Fabian et al. 2000; Ricci et al. 2014), which is much smaller than current satellite spectral resolution (e.g. *XMM-Newton* has a spectral resolution of ~ 150 eV at 6.4 keV). In a Newtonian, non-relativistic disc, the Fe Kα line would have a perfectly symmetrical double-horned profile due to the Doppler shift of the radiation emitted by the approaching (blue-shifted) and receiving (red-shifted) edges of the accretion disc (Fabian et al. 1989; Laor 1991; Fabian et al. 2000). The broadness of the line in this case would be determined by the velocity of the matter rotating at the innermost disc radius, which is the highest speed. However, the presence of the SMBH introduces relativistic effects that influence further the line profile. Special relativistic beaming enhances the blue peak of the line from every radius of the accretion disc. Transverse Doppler effect and gravitational redshift determine that photons can leave the gravitational potential of a BH only by losing energy thus shifting Fe Kα emission from every radius to lower energies. The sum of the contributed emission from all the accretion disc radii results in a skewed and highly broadened line profile (see Figure 1.7) (Fabian et al. 1989; Laor 1991; Bromley et al. 1998; Pariev & Bromley 1998; Martocchia et al. 2000).

The shape of the line profile is also determined by the metric of the spacetime. In the Shwarzschild metric

$$\frac{\nu_{obs}}{\nu_{em}} = \sqrt{1 - \frac{2}{r}}, \tag{1.9}$$

where ν_{em} is the emitted frequency, ν_{obs} is the observed frequency at infinity and r is the emission radius. In the Kerr metric, the gravitational redshift is defined as

$$\frac{\nu_{obs}}{\nu_{em}} = \sqrt{1 - \frac{2r}{r^2 + a^2}}, \tag{1.10}$$

however, this holds only for the photon emitted on the rotation axis ($\theta = 0$). Eq. 1.10 shows, that by increasing BH spin, the energy width of the Fe Kα line will also increase.

The profile of the Fe Kα line is also affected by the geometry of the matter surrounding the SMBH (Laor 1991; Brenneman & Reynolds 2006; Dauser et al. 2010, e.g.). The extended high-energy wing of the feature is a strong function of the angle between the normal to the accretion disc and the line of sight, which from now on we will refer to as the inclination angle. At low

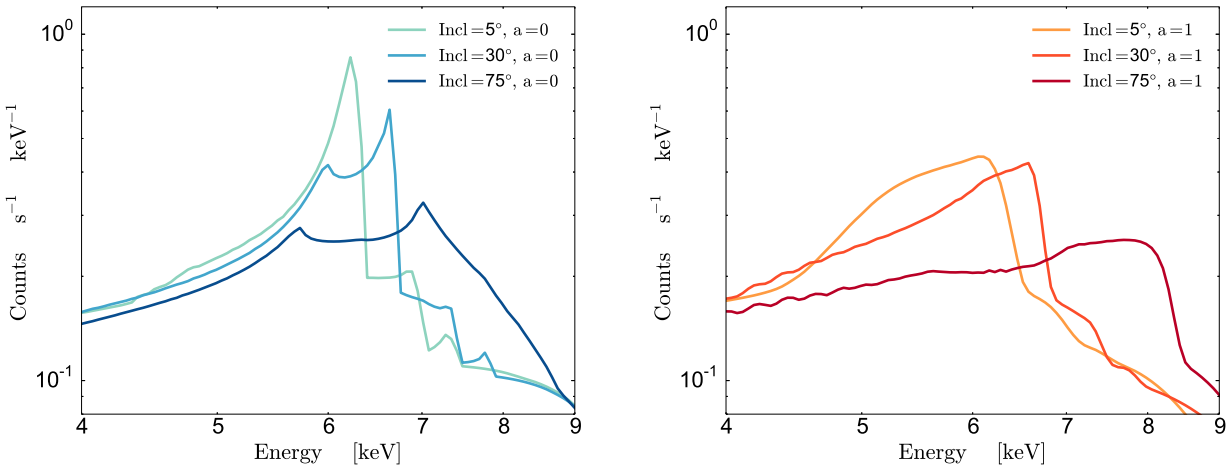

Figure 1.7: The Fe K α line is intrinsically narrow but its profile is broadened and skewed by the relativistic Doppler effect and gravity. The line profile depends on the geometry of the disc, thus inclination with respect to the line of sight, and spin of the BH. For this reason, the Fe Kα line profile is a diagnostic of relativistic signatures of SMBH and a great tool to test the AGN unification model.

inclination angles the observer views the disk almost face-on. In this case, the observer will see almost nothing of the rotation of the disk and there will be no large velocity component. In contrast, at high inclination angles, the observer sees the approaching and receding parts of the disk. In this case, the high-energy extent is increased by relativistic boosting and the line will appear to be double-horned (Fabian et al. 1989; Fabian et al. 2000) (see Fig. 1.7). High disc inclinations imply that the emission from the innermost regions of the disc is shielded and absorbed by the molecular torus (see Section 1.2). In the case of a toroidal uniformly distributed as predicted by the unification theory of AGN we would never be able to observe relativistic broadened Fe Kα lines in AGN with high column density and high disc inclinations. If however, we assume a clumpy molecular torus, then it would be possible to observe some radiation from the disc from the gaps in the torus. Thus, the relation between the broadening of the Fe Kα line and the disc inclination can be used as a test of the unification theory of AGN and to probe the geometry of the matter surrounding the SMBH (Zhang et al. 2008; Ricci et al. 2014).

The intensity of the Fe Kα line (and of the reflection component in general) might also reveal the geometry of the corona of relativistic electrons emitting the primary X-ray continuum (see Fig. 1.4) (Fabian et al. 2000; Ballantyne & Fabian 2003). In fact, different corona shapes determine how much X-ray radiation is reflected by the disc and thus how strong is the observed reflection component. Stronger reflection is observed in the case of a lamp-post geometry, where the height of the point source is larger than r_g (Bambi 2017).

The theory attributing relativistic effects to the broadness of the Fe Kα lines is widespread yet not unequivocally proven. Alternative hypotheses suggest that the broadening of the Fe Kα line is artificially introduced when the X-ray continuum is absorbed (e.g. Miller et al. 2008). In fact,

AGN showing a broadened Fe Kα emission line often present signs of absorption from several layers of ionized gas and ionized outflowing winds (Nandra et al. 2007; Miller et al. 2007, 2008). Distinguishing these requires high quality X-ray data.

The presence of broadened Fe Kα lines is well documented especially in bright AGN in the nearby Universe (e.g. MCG–6-30-15 Tanaka et al. 1995; Miller et al. 2002). However, there are some objects in which the broad Fe Kα line is not detectable (Gondoin et al. 2003; Pounds et al. 2003).

Relativistic lines are expected to be ubiquitous if we assume a standard scenario where the SMBH is surrounded by an accretion disc and a hot corona of electrons (Nandra et al. 2007; Guainazzi et al. 2006; Mantovani et al. 2014). The fact that these features are not always found is hard to explain. A possible reason for this could be that the matter in the disc is ionized. Indeed, it is reasonable to expect some degree of ionization, especially at large accretion rates. A strong reduction of the line flux is expected for moderate ionization due to resonant trapping. At very large degrees of ionization, the matter is fully ionized and no fluorescent line is emitted (Fabian et al. 2000). For a given BH mass M, the ionization parameter ($L/\eta r^2$) increases with luminosity. However, at fixed Eddington ratio, the ionization parameter decreases with the BH mass, hence its luminosity. It would be important to search for relations between the presence of the broad Fe Kα line and the luminosity or the accretion rate.

Another reason not to detect broad lines could be an accretion disc truncated well before the last stable orbit. It could also be possible that the broad line is present but so broadened to make it hard to detect, especially in faint sources (Guainazzi et al. 2006; Mantovani et al. 2014).

An interesting aspect of the Fe Kα line that could also explain why sometimes this feature is not detected is the anti-correlation between the line energy width (EW) and the luminosity of the X-ray continuum, called the Iwasawa-Taniguchi or X-ray Baldwin effect. Observed for the first time by Iwasawa & Taniguchi (1993), this anti-correlation has been confirmed several times and has been linked to the receding of the molecular torus at high luminosity. The same effect for the broad Fe Kα line was proposed for the first time in Nandra et al. (1997b), but not subsequently confirmed. The physical origin of the Baldwin effect for the broad wings of the line is very different from the one producing the anti-correlation for the narrow core. The broad component arises in the rings of the accretion disc closer to the ISCO and the central SMBH. A strong AGN luminosity could imply a higher ionization rate of the disc and in the most extreme scenarios the receding of the disc itself, which would suppress the emission of the Fe Kα line from those regions.

Detecting the Baldwin effect for the broad component of the Fe Kα line and disentangling it from the Baldwin effect for the narrow component would provide important insights on the geometry of the disc and molecular torus (Nandra et al. 1997b).

To sum up, the Fe Kα line is one of the most insightful features in the X-ray spectrum of AGN. The strong dependency of the line profile with spin and inclination angle of the disc makes it the perfect tool to probe the relativistic effects due to the proximity of the SMBH, the mode of BH accretion, and the unification theory of AGN. Studying the profile of the Fe Kα line could also solve open issues like the structure of the molecular torus and the geometry of the relativistic corona emitting the X-ray primary continuum.

1.5 X-ray instruments

The Earth's atmosphere is opaque to X-rays, thus X-ray instruments have to be mounted on high altitude rockets, balloons or satellites. Even if the technology to send detectors via rockets was already devised in 1929 by Edward Hulburt and used in 1949 by Herbert Friedman to detect solar X-rays, the true birth of X-ray astrophysics can be a dated to 1962, when Riccardo Giacconi imaged with a rocket-born detector the first extra-solar X-ray source Scorpius (Sco) X-1. Sco X-1 was later identified with a neutron star in a binary system with a low mass star.

X-ray astronomy and the technology required for it are complicated further by the difficulties in focusing X-ray photons. X-ray photons are approximately 1000 times more energetic than optical photons. Thus, the energy of an X-ray photon is greater than the binding energy of the electrons in most atoms, making the refractive index for X-rays less than unity. For this reason, single surface reflectivity is negligible for X-rays with incidence angles approaching the normal, and X-ray telescopes must be very different than optical telescopes. In fact, if X-ray instruments would have the same structure as optical ones, the X-ray photons will penetrate the mirrors like a bullet penetrates a wall. Thus, X-ray photons have to hit the mirror at a grazing angle to be focused, similarly to the way bullets ricochet when they hit a wall at a grazing angle. The grazing angle is about a degree for energies up to 10 keV but it decreases for higher energies. For this reason, the point spread function (PSF) of X-ray telescopes is energy-dependent.

In 1952, H. Wolter developed an X-ray focusing system using mirrors in the shape of rotated conic curves (Wolter 1952a,b). He showed that it is not possible to image a two-dimensional focusing of a field and an even number of nested surfaces is needed.

There are currently more than six X-ray satellites orbiting Earth and thirteen have already finished their course. In this work however, we mainly concentrate on the two observatories *Chandra* and *XMM-Newton*.

1.5.1 *Chandra*

The *Chandra X-ray observatory*[2] (*CXO*), previously known as the *Advanced X-ray Astrophysics Facility* (*AXAF*) was launched by NASA on the 23rd of July, 1999. Although it was initially given an expected lifetime of 5 years, *Chandra* has been observing the Universe for more than 20 years. The *Chandra* observatory consists of three major parts: the mirrors, the science instruments, and the spacecraft.

The focusing mirrors of *Chandra* are the largest, smoothest, and most precisely built and aligned X-ray mirrors ever constructed. If the surface of Earth were as smooth as the *Chandra* mirrors, the tallest mountain would be only two meters tall. *Chandra* is a Wolter telescope type II. Its mirrors consist of four pairs of nested cylindrical paraboloids and hyperboloids with a common focal length of 10 m. The mirrors system together with its supporting structure is called High-Resolution Mirror Assembly (HRMA). The mirrors have a 2 cm thick substrate coated with an iridium layer 33 nm thick for the reflecting surface. The thick substrate is fabricated with Zerodur, a material chosen for its low coefficient of thermal expansion and demonstrated

[2] https://chandra.si.edu/about/

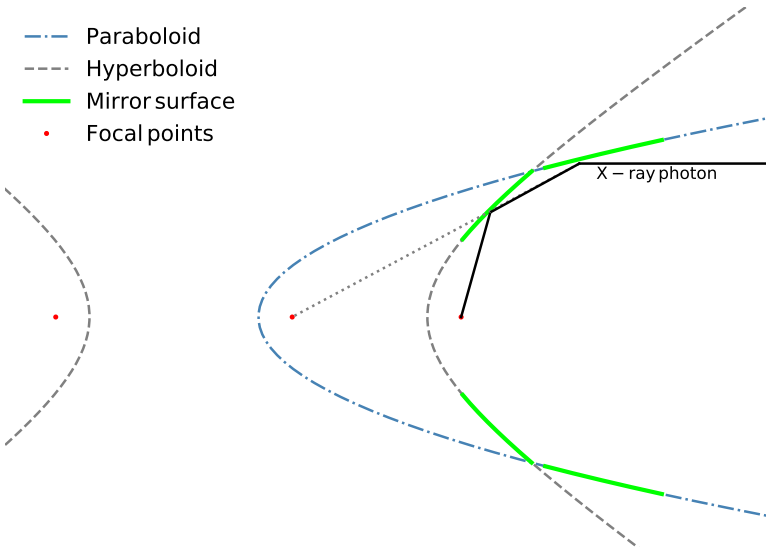

Figure 1.8: Scheme of Wolter I type optics. X-rays are so energetic that they usually get absorbed by the matter they interact with or they pass through without being reflected. The only way to focus X-ray photons is to reflect them at grazing angles. A Wolter I telescope design is based on this principle. They comprise paraboloid and hyperboloid mirrors (green) coated with iridium or gold. Technically it would also be possible to focus X-ray photons only using paraboloidal mirror shells, however, the focal length would be too long to be manageable. To increase the collecting area usually several sets of nested mirrors are required. For example, the high-resolution mirror assembly in *Chandra* consists of four nested Wolter I mirrors. The mirrors of *Chandra* were produced to be extremely precise and smooth to allow an angular resolution of 0.5 arcsec (on-axis). For this reason, it was necessary for every mirror to be 2 cm thick to avoid deformations due to stresses during the launch and the life of the satellite. *XMM-Newton* carries three Wolter I telescopes. The satellite was designed to have a larger collecting area with respect to *Chandra*. For reasons of mass, the mirrors in *XMM* are not as thick as the one carried by *Chandra*, thus it was possible to nest 58 mirrors in each of the three-mirror modules.

the capability of permitting very smooth polished surfaces. The mirror has to be this thick to be more stable and to avoid deformations following the launch or due to temperature swings. However, the thickness of the substrate limits the number of nested mirrors allowed resulting in a smaller collecting area compared for example to *XMM*-Newton.

The *Chandra* science instrument module holds two focal plane cameras: the Advanced CCD Imaging Spectrometer (ACIS, Principal Investigator (PI) Prof. G. Garmire) and the High-Resolution Camera (HRC, Dr. S. Murray, Smithsonian Astrophysical Observatory at Johns Hopkins University, PI). ACIS contains two arrays of CCDs that provide information over the energy and position of each detected X-ray photon. The imaging array (ACIS-I), which is specialized for surveys, consists of four CCDs (I0-I3) of 1024×1024 pixels each arranged in a 2×2 configuration. The spectroscopy array (ACIS-S) consists of six CCDs (S0-S5) arranged in 1×6 and can be used for imaging or for moderate-resolution spectra. In this work only ACIS-I is used. Used together with the High Energy Transmission Grating (HETG, Prof. C. Canizares, Massachusetts Institute of Technology, PI) or the Low Energy Transmission Grating (LETG, PI: A. Brinkman, SRON, Utrecht, with the collaboration of MPE, Garching), the ACIS-S can provide higher-resolution spectra with a resolving power ($E/\Delta E$) up to 1000 over the 0.4-8 keV band. The High-Resolution Camera (HRC) is a microchannel plate (MCP) instrument comprised of two detectors, one optimized for imaging (HRC-I), and one (HRC-S) which serves as a read-out for the Low Energy Transmission Grating (LETG). The HRC detector provides the highest spatial and time resolution on *Chandra*.

1.5.2 *XMM-Newton*

XMM-Newton, previously known as the X-ray Multi-Mirror Mission, is an X-ray space observatory launched on the 10th of December 1999 by the European Space Agency (ESA). XMM carries three Wolter Type I telescopes, whose mirror modules total a collecting area of over 120m^2 spread across three different X-ray telescopes[3], the largest collecting power ever achieved with an X-ray observatory. Each mirror module comprises 58 nested golden plated nickel mirrors only a few millimeters apart. The mirrors has a diameter of 70 cm and the focal length of the telescopes is 7.5 m.

Aboard the spacecraft, there are three instruments. The primary instrument is the European Photon Imaging Camera (EPIC), positioned at the focus of the three telescopes. EPIC consists of three cameras to record the incoming X-ray photons and provide both imaging and spectroscopy. The EPIC cameras perform sensitive imaging over a field of view (FOV) of 30 arcmins over the energy range 0.15–15 keV with spectral resolution $E/\Delta E \sim 20 - 50$ and angular resolution of 6 arcsec FWHM. Two of the cameras make use of metal oxide semiconductor (MOS) CCDs while the third uses a new type of CCD detector, pn, developed by a collaboration of the Max-Planck Institute for Extraterrestrial Physics (MPE) in Garching and the Astronomical Institute in Tübingen. The MOS detectors are located at the focal point of the two telescopes equipped with the gratings of the reflection grating spectrometers (RGS), the second *XMM* instrument , while

[3] https://www.esa.int/Science_Exploration/Space_Science/XMM-Newton_factsheet

the pn EPIC CCDs receives an unobstructed beam of photons.

The third instrument on *XMM* is the optical monitor (OM) mounted on the mirror platform together with the mirror modules. OM supplies UV/optical wavelength coverage of the central 17 arcmin^2 region of the X-ray field of view. The instruments cover the wavelengths between 170 nm and 650 nm. The XMM-OM comprises the Digital Electronics Modules and a Telescope Module. The Digital Electronic Modules, made of two identical units for redundancy, contains the Instrument Control Unit, which is responsible of the communication with the spacecraft, and the Processing Unit, which pre-processes the data before it is sent to the ground. The Telescope Modules contain the telescope optics and the detectors, together with the detector processor and power supply.

In this work, only EPIC data are used.

1.6 This thesis

The study of the Fe Kα and Compton hump features in the X-ray spectra of AGN can unveil important properties of the SMBH and the matter surrounding it. By quantifying the broadening of the line profile we can infer the magnitude of the BH spin, the inclination of the accretion disc, and even get hints on the geometry of the relativistic corona.

The goal of this work is to establish how common is the relativistic broadened reflection outside the nearby Universe.

In Chapter 2 we study 199 hard selected sources from the CDFS 4Ms. We fit all the spectra with BXA to calculate the Bayesian evidence and best-fit parameters for four different models. We choose physically motivated models of progressive complexity, starting from an absorbed power-law and adding to this simpler model a narrow reflection component from the molecular torus and a broad reflection component from the accretion disc.

In Chapter 3 we extend the analysis of 2 to four additional *Chandra* surveys: the CDFS 7Ms, CDFN, AEGIS and COSMOS.

In Chapter 4, we investigate different physically motivated models on the high-SN *XMM* spectra of MCG-6-30-15. The aim of the project is to determine whether outflowing winds are necessary to fit the data and whether a broad Fe Kα line is still needed in the model once the outflowing winds are added. We also test the theory according to which the broadening of the Fe Kα feature is not due to relativistic effects but too complex absorption of the X-ray continuum.

In Chapter 5, I summarize the work in the previous chapters and offer a small discussion on the possible future work that could be done to further expand our knoweledge of the Fe Kα feature.

Lastly, I summarize briefly the Bayesian methods used in this thesis in Appendix A.

Chapter 2

Relativistic reflection from accretion disks in the population of Active Galactic Nuclei at z=0.5–4

In this chapter, we report the detection of relativistically broadened iron Kα emission in the X-ray spectra of AGN detected in the 4Ms CDF-S. Using the Bayesian X-ray analysis (BXA) package, we fit 199 hard band (2–7 keV) selected sources in the redshift range z=0.5–4 with three models: (i) an absorbed power-law, (ii) the first model plus a narrow reflection component, and (iii) the second model with an additional relativistic broadened reflection. The Bayesian evidence for the full sample of sources selects the model with the additional broad component as being 10^5 times more probable to describe the data better than the second model. For the two brightest sources in our sample, CID 190 (z=0.734) and CID 104 (z=0.543), BXA reveals the relativistic signatures in the individual spectra. We estimate the fraction of sources containing a broad component to be 54^{+35}_{-37}% (107/199 sources). Considering that the low signal-to-noise ratio of some spectra prevents the detection of the broad iron Kα line, we infer an intrinsic fraction with broad emission of around two thirds. The detection of relativistic signatures in the X-ray spectra of these sources suggests that they are powered by a radiatively efficient accretion disk. Preliminary evidence is found that the spin of the black hole is high, with a maximally spinning Kerr BH model (a=1) providing a significantly better fit than a Schwarzschild model (a=0). Our analysis demonstrate the potential of X-ray spectroscopy to measure this key parameter in typical SMBH systems at the peak of BH growth.

This work was published as Baronchelli et al. (2018) in Monthly Notices of the Royal Astronomical Society, Volume 480, Issue 2, p.2377-2385

2.1 Introduction

The X-ray emission from active galactic nuclei (AGN) is believed to arise when the optical/UV photons radiated from the accretion disk are inverse Compton scattered by a corona of hot electrons surrounding the supermassive black hole (SMBH) (e.g., Sunyaev & Titarchuk 1980; Haardt

& Maraschi 1991, 1993; Zdziarski 1998; Jovanović & Popović 2009). The primary X-ray photons illuminate and are reprocessed by material surrounding the nucleus, including the accretion disk and the obscuring torus, producing a co-called Compton reflection spectrum (e.g., George & Fabian 1991). Thus, the reflection component of the AGN X-ray spectrum contains information about the geometrical structure and the dynamics of the matter surrounding the SMBH (Reynolds 1999). The most prominent features of the reflection component are the iron (Fe) Kα feature at 6.4 keV in the rest frame and the Compton hump peaking at energies around 30 – 40 keV (e.g. Pounds et al. 1990; Nandra & Pounds 1994). The Compton hump is only produced when the matter surrounding the SMBH is Compton thick ($N_H \gtrapprox 10^{24}$ atoms cm^{-2} which is approximately the inverse Thomson optical depth τ_{Thom}) while the Fe Kα line can be produced also when the reflecting material is Compton-thin (Lightman & White 1988; Krolik 1999; Ricci et al. 2014). Narrow components to the Fe Kα emission are seen nearly ubiquitously in the spectrum of nearby AGN (Yaqoob & Padmanabhan 2004; Nandra et al. 2007; Ricci et al. 2014) and generally attributed to an origin in the molecular torus (Krolik & Kallman 1987; Nandra 2006). However, when the reflection component arises from the innermost region of the accretion flow such as the accretion disk, the gravitational field of the SMBH affects the shape of the line (Fabian et al. 1989). The resulting line profile is broadened and skewed by light bending, gravitational redshift and relativistic Doppler shifts and in extreme cases the line can extend in energy from ∼3–7 keV (Fabian et al. 2000; Lee et al. 2002; Yaqoob 2007), indicating an origin close to the innermost stable orbit of the accretion disk. Because this depends on the black hole spin, the study of broadened Fe Kα lines represents an important probe of general relativistic effects and the dynamics of the SMBH, as well as the matter immediately surrounding it (Yaqoob et al. 2002; Reynolds & Nowak 2003; Fabian et al. 2005).

The clearest evidence for a relativistic broadened Fe Kα line was found by Tanaka et al. (1995) in the spectrum of the nearby Seyfert galaxy MCG-6-30-15 observed by *ASCA*. Since then, the presence of a skewed and broadened Fe Kα line profile has been confirmed in the X-ray spectra of many other bright, nearby AGN (Nandra et al. 1997a; Guainazzi et al. 2006; Nandra et al. 2007; de la Calle Pérez et al. 2010). While the relativistic phenomena therefore seem to be reasonably widespread in nearby SMBH systems, it is much more difficult to establish whether they are common in typical AGN at higher redshifts, and specifically those responsible for the bulk of the accretion power in the Universe, during the peak of black hole activity at z=0.5-4.

Past work aiming to do this has used stacking of the Fe Kα line in large samples of observations with low signal to noise ratio (Streblyanska et al. 2005; Chaudhary et al. 2012). In principle, this allows one to infer the global properties of the population in cases where it would be uninformative to fit single sources individually. For example, by analyzing the mean rest-frame spectra of a sample of type-1 and type-2 AGN over a broad redshift range in the Lockmann hole from the *XMM-Newton*, Streblyanska et al. (2005) presented evidence for broad Fe Kα line emission. However, it has been found that stacking the spectra can introduce artificial broadening in the Fe Kα line, especially in samples where the sources have a wide redshift distribution (Chaudhary et al. 2012). Chaudhary et al. (2012) nonetheless concluded after performing rest-frame stacking of a sample of 248 AGN from the 2XMM catalog that the average Fe Kα line profile is best represented by a combination of narrow and broad line. On the other hand, Corral et al. (2008) computed the averaged rest-frame spectrum of 600 *XMM-Newton* observation of type-1 AGN

without finding compelling evidence for any significant broad line component.

Evidence for broad Fe Kα line emission in stacking studies has also been reported in Falocco et al. (2013), where the XMM CDF-S spectra were averaged, and in Falocco et al. (2014), where the authors explored the spectra of an AGN sample built using the 2nd XMM serendipitous survey and the VCV catalog (Véron-Cetty & Véron 2006, 2010). The detection in Falocco et al. (2014) is compatible with the upper limit obtained in Corral et al. (2008, 2011). Liu et al. (2016) also found that the Fe Kα might get broader by higher Eddington ratio. Falocco et al. (2012, 2013, 2014); Liu et al. (2016) support the spectral stacking with simulations that quantify the broadening introduced by the stacking itself. Hence, these studies are free of artificial broadening.

Thus, the ubiquity of the relativistic broadened Fe Kα line in AGN X-ray spectra outside the local Universe is still controversial.

In this work, we aim to investigate the presence of the relativistic broadening of the Fe Kα in the spectra of the AGN population as observed with Chandra using a different approach, specifically by using the Bayesian X-ray analysis (BXA) spectral fitting method (Buchner et al. 2014). This allows information to be extracted from the individual spectra even if of low signal-to-noise ratio, and the results combined to make inferences about the population as a whole. In Sect. 4.3 we define the method and the spectral modeling applied to our data, including the definition of the sample selection. The results of the analysis are reported in Sect. 4.4 and discussed in Sect. 2.5.

Throughout this work, we adopt Ω_m= 0.272, Ω_Λ= 0.728, and H_0 = 70.4 km s^{-1} Mpc^{-1} (Komatsu et al. 2011). Errors are quoted at the 90% confidence level unless otherwise specified.

2.2 Method

2.2.1 Data and Sample selection

In this work we wish to explore the X-ray spectral properties of sources at the peak of supermassive black hole activity. Our sample is chosen from the 4Ms exposure of the *Chandra* Deep Field-South (CDF-S) (Xue et al. 2011), totaling 51 observations over an area of 464.5 arcmin^2. This deep *Chandra* exposure gives us the opportunity of studying the Fe Kα line of AGN spectra up to redshifts of $z \sim 4$.

The source and background spectra employed in this work are a selected subsample of the spectra extracted by Brightman et al. (2014) analyzed by Buchner et al. (2014) from the CDF-S 4Ms, which is based on the source catalog of Rangel et al. (2013) (hereafter R13), using data reduction methods following the work of Laird et al. (2009). The background extraction region around any given source is constructed so that it contains at least 100 counts after masking all the other sources out. Our sources are hard band (2–7 keV) selected and as in Rangel et al. (2013) are considered significant if the Poisson probability that the observed counts are a background fluctuation is less than 4×10^{-6}. We used spectroscopic (preferably) or photometric redshifts from the work of Hsu et al. (2014), following Buchner et al. (2014). In addiction to this, we restrict the analysis to sources with redshift lower than 4, both due to limitations in models and

because above this redshift the sources are few and of low signal-to-noise ratio. To ensure the reliability of the fits to the Fe K α feature, we exclude from the analysis sources with less than 20 counts in the 4 – 7 keV energy range. The selected sample is composed of 123 sources with spectroscopic redshift and 76 sources with photometric redshift for a total of 199 sources. Note that in the case of sources with photometric redshift, the probability distribution function is used in the spectral fitting rather than a single value, thus accounting for the systematic uncertainties in the photo-z determination (Buchner et al. 2015). In total, the selected sources show 30,667 counts in the 4–7 keV rest frame energy range. The total number of counts in this energy range in our sample is comparable to bright sources in the local Universe. Nandra et al. (2007), for example, imposed a lower limit of 30,000 counts in the 2-10 keV band when constructing their sample. Once combined, our data quality should be sufficient to provide constraints on the broad iron line (see e.g. Guainazzi et al. 2006; Mantovani et al. 2014).

2.2.2 Model comparison overview

We employ the Bayesian X-ray Analysis (BXA, Buchner et al. 2014) software to fit the X-ray spectra and compare models. BXA is a Bayesian framework to determine the best-fitting models and their parameter constraints for X-ray spectra. It can also be used as a robust statistical tool to determine if the data are better fit by a model containing a relativistically blurred component or by a simpler model. A key features is that it allows us to analyze a large sample of low signal to noise ratio observations and make inferences for the population without the need to stack the spectra. BXA computes for each model the Bayesian evidence Z, which is the likelihood integrated over the parameter space (see Section 2.2.4). The ratio Z_{M_1}/Z_{M_2} can then be used to compare the models M_1 and M_2.

We compared three models to the X-ray data. We first fit the spectra using a simple absorbed power-law to model the intrinsic X-ray emission. We then added a narrow reflection component to the intrinsic continuum, presumed to arise from distant material such as the molecular torus. Finally we added a blurred reflection component attributed to the accretion disk. The primary continuum of the AGN X-ray spectra was modeled with a redshifted power-law `zpowerlw`. The narrow reflection was modeled with the `pexmon` model (Nandra et al. 2007), which combines a reflected power-law in neutral medium (Magdziarz & Zdziarski 1995) with self consistently generated Fe Kα (6.4 keV), Fe Kβ (7.059 keV), Ni Kα (7.48 keV) and the Fe Kα Compton shoulder. We modeled the relativistic broadened component by convolving another `pexmon` component with a kernel representing different models of a relativistic accretion disk around the SMBH. We consider both the case of a Schwarzschild SMBH, with spin a = 0, and the case for a Kerr SMBH, with a = 1, given that the shape of the emission line depends on the metric used to describe the space-time of the SMBH. The first is achieved by convolving the `pexmon` with the `rdblur` model (a=0, Fabian et al. 1989) and the second the `kdblur` model (a=1, Laor 1991). Convolving the `pexmon` with these relativistic kernels has the advantage that the entire reflection components is blurred and not only the Fe Kα line.

The free and frozen parameters of the three models are listed in Table 2.1, 2.2 and 3.2 as well as the intervals chosen as the priors for BXA. We obtain the likelihood and the best fit parameters using the C-statistic (Cash 1979). This statistic is appropriate with low signal to noise data where

the counts are sampled from the Poisson distribution. When applying the C-statistic we can not subtract the background, so we model this simultaneously with the source spectrum. We use the Chandra background model from Buchner et al. (2014) (see Figure 2.1).

To be able to use the *Chandra* background (Figure 2.1) implementation from Buchner et al. (2014) we use the SHERPA (Freeman et al. 2001) implementation of BXA (CIAO version 4.8). However, the two convolution models `rdblur` and `kdblur` used to blur the `pexmon` are available only in XSPEC (Arnaud 1996). We therefore produced a table model of the convolved `pexmon`, `kdblur(rdblur)` and `kdblur(pexmon)`, from XSPEC (version 12.9.0) and imported the two table models into SHERPA. This procedure also has the advantage of reducing the fitting time required by BXA. To further speed the fitting procedure, we used XSPEC and the BXA module `RebinnedModel` to approximate the narrow `pexmon` component in models 2.2 and 3.2 by interpolating it over a smaller subsample of its prior space.

2.2.3 Model parameters

To define the models in a Bayesian framework we need to describe the prior distributions (or priors) of the parameters. The priors are the information about a parameter θ that is combined with the probability distribution of the data to generate the posterior distribution (Gelman 2002). In order to chose an appropriate prior distribution we need to take into account the information that the priors are going to contain and the properties of the resulting posterior distribution. We constrain the priors of our parameters to be limited to physical motivated intervals. However, we maintain the priors are as uninformative as possible to avoid biases in the posterior distribution. Note also that the prior choices for parameters that the models have in common are unimportant. However, the prior spaces of the parameters not shared by all the models have to be chosen more carefully.

We report in Table 2.1, 2.2 and 3.2 the parameter space of the three models 2.1, 2.2 and 3.2 respectively. If the parameter is left free to vary we show the range of accepted values. We choose log-uniform priors on the normalization and column density n_H, and uniform priors on photon index and inclination (model 3.2).

The normalizations of the `pexmon` components (narrow and blurred) are modeled relative to the intrinsic power-law and may vary between 10^{-2} and 10. The lower limit for the relative strength of the reflection is chosen on the basis that weaker components would imply an extremely small solid angle subtended by the accretion disk at the X-ray source, and in any event would be undetectable in the data. For the simplest scenarios, it is not expected that the relative normalization should exceed unity. This can be the case, however, if there is dramatic variability of the X-ray continuum, or if strong gravitational light bending is at play (Miniutti et al. 2003) motivating the choice of our upper limit of $R = 10$.

Restricting the strength of the reflection components relative to the normalization of the primary power-law within reasonable physical limits reduces the prior volumes of the complex models.

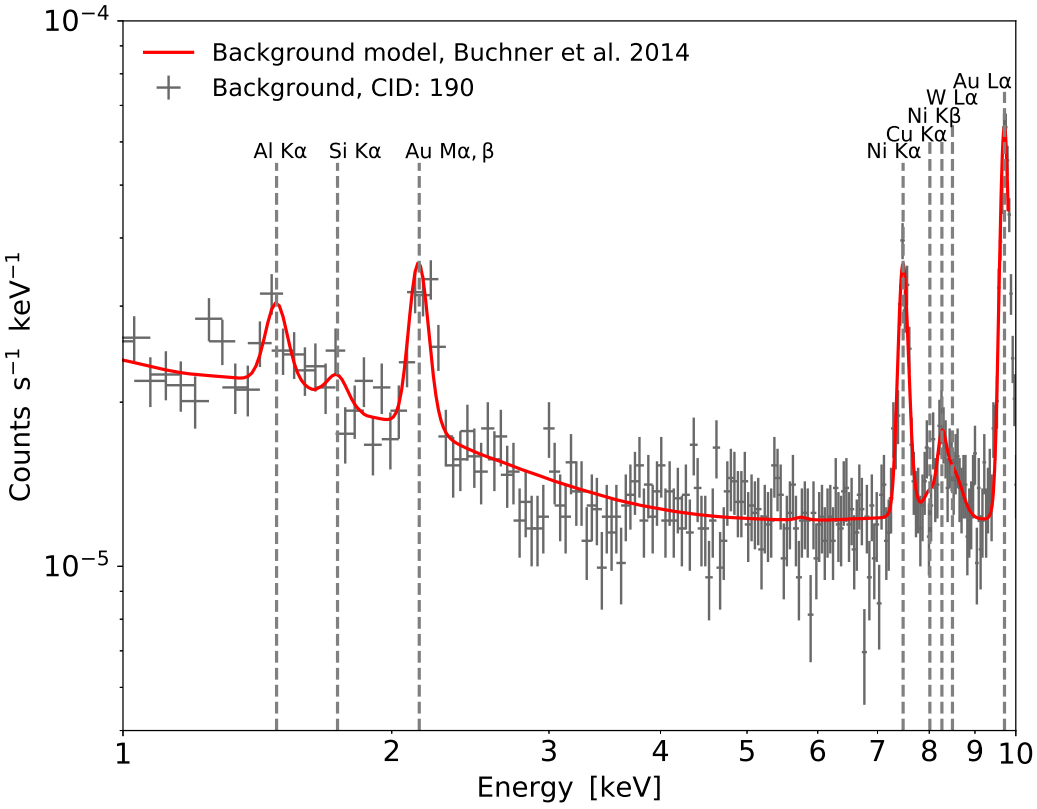

Figure 2.1: Example of the fitted background for the source CID 190. The background model (Buchner et al. 2014) is composed by eight narrow Gaussians describing the particle emission in the detector and a continuum component, described by a `box1d` SHERPA model (Bartalucci et al. 2014). In addition to the eight narrow Gaussians, the continuum also includes two broad Gaussians at energies lower than 1keV. The background model is first fitted to the background spectrum of each individual source. The best fit background parameters so-determined are subsequently frozen in the fit to the source spectrum, which is not background subtracted.

Table 2.1: Parameter description for model `zwabs * (zpowerlw)`. The model has three free parameters.

Comp.[a]	No.[b]	Name[c]	Min	Max	Fixed val.	free
zwabs	1	log(nH)	20	26	-	yes
	2	Redshift	-	-	z	-
zpowerlw	3	PhoIndex	1.1	2.5	-	yes
	4	Redshift	-	-	z	-
	5	log A_{pow}	-10	1	-	yes

[a] Model component.
[b] Parameter number.
[c] Parameter name.

Table 2.2: Parameter description for model `zwabs * (zpowerlw + pexmon)`. The model has four free parameters: the column density N_H, the photon index and the two normalizations. The strength of the unblurred reflection component R_{pex} is measured relative to the power-law and is defined as the ratio of the normalization of the pexmon component (A_{pex}) to that of the power-law (A_{pow}).

Comp.[a]	No.[b]	Name[c]	Min	Max	Fixed val.	Free
zwabs	1	log(nH)	20	26	-	yes
	2	Redshift	-	-	z	-
zpowerlw	3	PhoIndex	1.1	2.5	-	yes
	4	Redshift	-	-	z	-
	5	log A_{pow}	-10	1	-	yes
pexmon	6	PhoIndex	-	-	link to 3	-
	7	foldE	-	-	800	-
	8	rel_refl	-	-	-1	-
	9	redshift	-	-	z	-
	10	abund	-	-	1	-
	11	Fe_abund	-	-	1	-
	12	Incl	-	-	60	-
	13	log R_{pex}	-2	1	log $\frac{A_{pex}}{A_{pow}}$	yes

[a]Model component.
[b]Parameter number.
[c] Parameter name.

Table 2.3: Parameter description for model `zwabs * (zpowerlw + pexmon + blur(pexmon))` . The model component blur could be `rdblur` or `kdblur`. The model has six free parameters: the column density N_H, the photon index, the inclination of the broad component and the three norms. The strength of the blurred reflection component component R_{blur} is measured relative to the power law and is defined as the ratio of the normalization of the blurred pexmon component (A_{blur}) to that of the power-law (A_{pow}).

Comp.[a]	No.[b]	Name[c]	Min	Max	Fix val.	Free
zwabs	1	log(nH)	20	26	-	yes
	2	Redshift	-	-	z	-
zpowerlw	3	PhoIndex	1.1	2.5	-	yes
	4	Redshift	-	-	z	-
	5	log A_{pow}	-10	1	-	yes
pexmon	6	PhoIndex	-	-	link to 3	-
	7	foldE	-	-	800	-
	8	rel_refl	-	-	-1	-
	9	redshift	-	-	z	-
	10	abund	-	-	1	-
	11	Fe_abund	-	-	1	-
	12	Incl	-	-	60	-
	13	log R_{pex}	-2	1	log $\frac{A_{pex}}{A_{pow}}$	yes
kdblur rdblur	14	Index Betor10	-	-	3 -2	-
	15	Rin	-	-	6	-
	16	Rout	-	-	100/1000	-
	17	Incl	10	85	-	yes
pexmon	18	PhoIndex	-	-	link to 3	-
	19	foldE	-	-	800	-
	20	rel_refl	-	-	-1	-
	21	redshift	-	-	z	-
	22	abund	-	-	1	-
	23	Fe_abund	-	-	1	-
	24	Incl	-	-	link to 17	-
	25	log R_{blur}	-2	1	log $\frac{A_{blur}}{A_{pow}}$	yes

[a]Model component.
[b]Parameter number.
[c]Parameter name.

2.2.4 Model comparison in practice

BXA calculates the Bayesian evidence (Z, also said marginal likelihood) using the Multimodal Nested Sampling Algorithm (`MultiNest`, Skilling 2004; Feroz & Hobson 2008; Feroz et al. 2009, 2013) through its python wrapper `PyMultiNest` (Buchner et al. 2014). We use the Bayesian evidence Z to apply a model comparison using the Bayes Factor (BF) (see Equation 2.1) to determine which of the three fitted models describes the data better. The BF is the ratio of the marginal likelihood Z of two competing models. Thus the BF method will select the model with highest Z as the one better describing the data. The Bayesian evidence Z is the likelihood integrated over the prior distribution, thus the models with a large prior volume are naturally penalized. In our case, the broad component model has more free parameters, hence it is penalized by the BF method. To determine Z_{tot} for the entire sample we add the log(Z) of the single sources.

The outputs of BXA are the Bayesian evidence for the fitted model, the parameters posterior probability distribution and the marginal likelihood Z.

The Bayes factor B_{12} (BF) is the ratio of the Bayes evidence $Z_i = P(D|M_i)$, where i = 1, 2, of two competing models M_1 and M_2

$$B_{12} = \frac{Z_1}{Z_2} \tag{2.1}$$

(Jeffreys 1939). Occam's razor is naturally implemented in the Bayes evidence (see Equation 2.2) since it is defined as the likelihood ($L(\theta)$) integrated over the whole parameter space (θ) weighted by the priors ($P(\theta|M)$):

$$Z = P(D) = \int L(\theta)P(\theta|M)\mathrm{d}\theta \simeq P(\theta)\delta\theta L(\theta) \simeq \frac{\delta\theta}{\Delta\theta}L(\theta)\theta, \tag{2.2}$$

where M is the model, θ is the parameters vector and $\delta\theta/\Delta\theta$ is the Occam's factor (OF) (Jefferys & Berger 1992a). The OF is the ratio between the posterior accessible volume ($\delta\theta$) and the prior accessible volume ($\Delta\theta$) and it prevents data over-fitting by penalizing the BF of more complex models, i.e. the models with the largest prior volume.

The values of the BF method can be interpreted using the Jeffrey scale, which strengthens its verdict roughly every time that the logarithm of the BF ($\log(B_{ij})$) increases by one in logarithmic space (Robert et al. 2009).

2.3 Results

We fit our sample of 199 sources using BXA, to determine the Bayesian evidence for the fitted models, the likelihood and the best fit parameters with their posterior probability distributions, presented in Figure 2.4. We use the Bayesian evidence to compare the models 2.1, 2.2, and 3.2 and thus to determine which components are required to describe the data. In general, and as expected, the individual sources are usually too faint to select with high probability one model

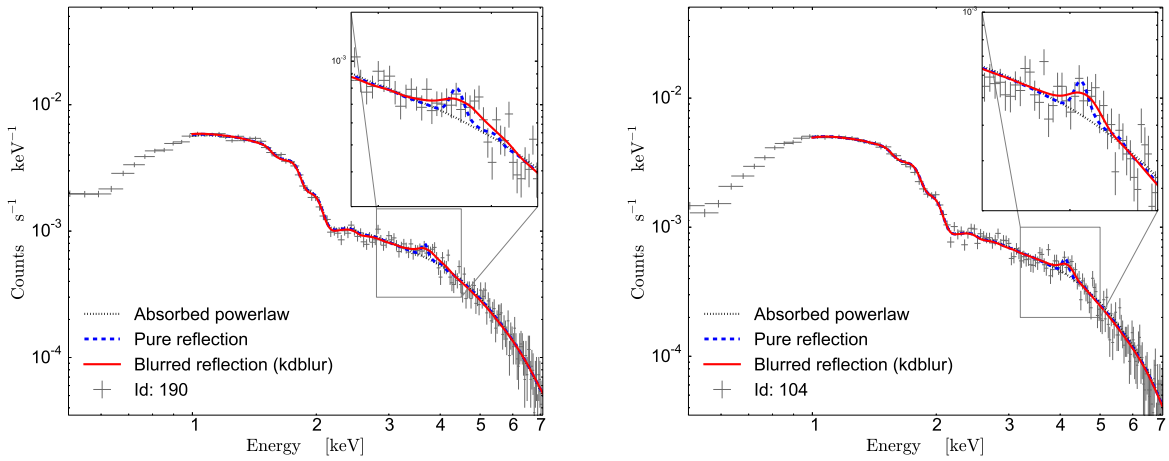

Figure 2.2: The two brightest sources in the selected sample, CID 190 (*Left*) and CID 104 (*Right*) (Id number from R13) at spectroscopic redshift of 0.734 and 0.543 and with number of counts in the 4–7 keV of 2723 cts and 2502 cts respectively. CID 190 and CID 104 are the only two sources of the sample with number of counts in the 4–7 keV higher than 2000 cts. These two sources are selected by the BF method as better fitted by model 3.2 with maximal spin. The models 2.1, 2.2 and 3.2 are shown in black (dotted), blue (dashed) and red (solid), respectively. Moreover, these sources are bright enough to constrain the inclination angle of the accretion disk modeled by the blurred component, albeit with large uncertainties.

over another. However, we can add the Bayesian evidences of the single sources to determine the evidence for the whole sample. We find that the BF method 3.2 selects the model containing a broad component as better fitting the full sample (see Table 2.4) with respect to the model for narrow reflection 2.2. The blurred model is selected to be 10^5 times more probable than the narrow model (see Table 2.4). Furthermore, by comparing the blurred model with a=0 and the one with a=1, we find that the model representing a maximally spinning BH is selected by the BF method as $10^{3.8}$ time more probable to be better fitting the data (see Table 2.4).

For the two brightest sources in our the sample, CID 190 (z_{spec} = 0.734; ID numbers from R13) and CID 104 (z_{spec} = 0.543) see Figure 2.2, the BF method also selects the blurred model with Kerr metric as best fitting the data. Using the BF method we obtain that for CID 190 model 3.2 is twelve times more probable than model 2.2, thus the difference in Bayes evidence is $\log_{10} \approx 1.1$ which is 22% of the evidence difference between 3.2 and 2.2 of the total sample. Instead, for CID 104 model 3.2 is five times as probable than model 2.2, hence its Bayes evidence difference ($\log_{10} \approx 0.7$) contributes to 13% of the difference in the evidence of the total sample. Hence, the contributions of CID 190 and CID 104 amount to the 35% of the total Bayesian evidence difference between the narrow and blurred models. Thus not taking the two brightest sources into account the Bayesian evidence difference would be of $\sim 10^{3.3}$ instead of 10^5. CID 190 and CID 104 have respectively 2723 and 2502 counts in the 4–7 keV energy range and are the only sources in the sample with more than 2000 counts in that range. While they have large uncertainties, the inclination values we obtain for the blurred component in CID 190 and CID 104 are consistent with the inclinations obtained for other sources in the literature where the relativistic component of the Fe Kα line was unambiguously observed. We obtain that the disk inclination of CID 190 is $\sim 35^{+5}_{-4}$ degrees, while the one of CID 104 is $\sim 37^{+20}_{-10}$ degrees (see Figure 2.5). While the vast majority of the individual sources have insufficient SNR to distinctly rule out one model over the others, we can still infer the fractions of sources containing a broad component by counting all the sources with highest Bayesian evidence for the broad model. Ranking the value of Bayesian evidence of the three models for each individual source, we find that the fraction of sources with highest evidence for the broad model, hence selected as containing the relativistic component is 54% (107/199). The sources selected as only containing a narrow reflection component are 19% (39/199), while the sources better described by a simple absorbed power-law comprise 27% (53/199) of the sample. These fractions have to be interpreted carefully, since in most cases the evidence difference between the three models is minimal (see Figure 2.6). Nonetheless, the fraction of sources selected as presenting a relativistic broadened component obtained in this work is comparable with the fraction observed in Nandra et al. (2007) for local AGN.

2.3.1 False positives and negatives

Because the difference in the evidence between the various models is generally small, statistical effects can result in both false positive detection for the relativistic components, or false negatives. To estimate the error on the selected fraction of sources showing a broad component we performed a set of simulations using the `fake_pha` tool of SHERPA. We simulated 200 sources for each of the spectral shapes given by models 2.1, 2.2 and 3.2. The fake sources are simulated

Table 2.4: Comparison of the total sample Bayesian evidence for the models `zwabs * (zpowerlw)`, `zwabs * (zpowerlw + pexmon)` and `zwabs * (zpowerlw + pexmon + blur(pexmon))`. We fit the models in the observed frame energy range 1 – 8 keV.

Model [a]	log10(Z)[b]
`zwabs*(zpowerlw)`	-78.1
`zwabs*(zpowerlw+pexmon)`	-5
`zwabs*(zpowerlw+pexmon+rdblur(pexmon))`	-3.8
`zwabs*(zpowerlw+pexmon+kdblur(pexmon))`	0

[a] Model components.
[b] Logarithm of the Bayes evidence of the full sample normalized to the largest evidence.

using the ancillary files of source CID 179 following the example of Buchner et al. (2014), for each spectral shape we assign the power-law norm 5×10^{-6} to the first 100 simulated sources and 10^{-5} to the remaining 100 sources. The strength of the blurred and narrow components with respect to the power-law norm is fixed to be $\log \mathrm{R} = -0.3$, which is the typical value found by (Nandra et al. 2007). This a conservative value, since if the actual R is smaller the number of false positives in the simulations will be overestimated. We fit the simulated sources using BXA to determine how many false positives and negatives we obtain by applying this method. The redshift of the simulated spectra is fixed at z=0.605, corresponding to the redshift of the original observation.

By applying the three models to the spectra simulated using the `pexmon` model, we obtain that ∼63% of the simulated sources (126/200) are rightly selected as `pexmon` while ∼37% (74/200) are false positives, in that they are selected as containing a broad component even though we know that the underlying spectrum does not contain one. The total Bayes evidence shows correctly that the sample is better described by the `pexmon` model.

Similarly, if we fit the three analyzed models to the spectra simulated using a broad component we obtain that 65% (130/200) of the sources are correctly selected as broadened.

The above analysis indicates that the inferred fraction of broadened components in our sample derived above (∼ 54%) is likely to be a lower limit. For the typical signal-to-noise ratios in our sample around 35% of broad components would not be detected even if present, while 37% are false positives. If we consider only models 2.2 and 3.2 in the CDF-S sample without including model 2.1 in the model comparison, we obtain that 63% (125/199) sources are selected as blurred while 37% (74/199) are selected as narrow. This result is very similar to the one obtained for the simulated sample with blurred component.

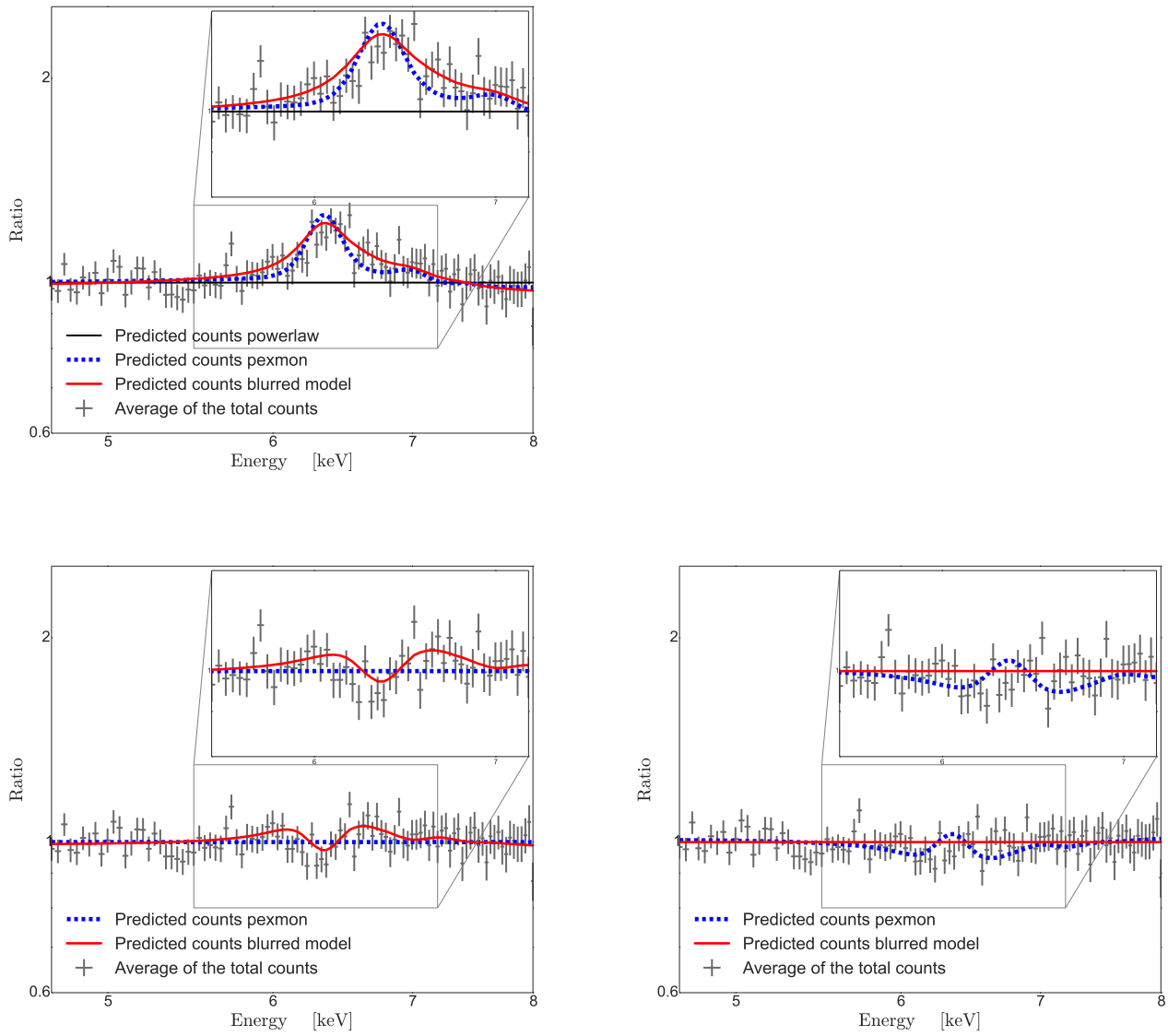

Figure 2.3: *Top*: Average of the total counts of the 199 spectra compared with the average of the three best fit models. The data and the models were normalized by the average of the best fitting power-law. *Bottom left*: Same as above but in this case the data and the models are normalized by the narrow pexmon model (blue, dashed). *Bottom right*: Same as above but data and models are normalized with the model including the blurred pexmon (red, solid). By comparing the two plots on the bottom it can be observed that the blurred model describes the data better than the narrow pexmon.

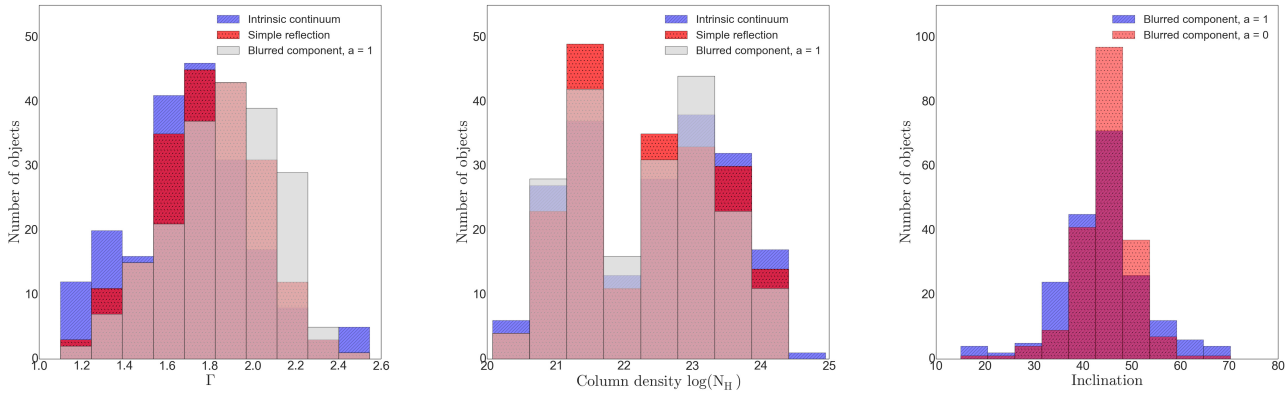

Figure 2.4: *Left*: Histogram of the best fit photon index Γ for the three models for the full sample. *Middle*: Best fit column density N_H for the full sample. *Right*: Comparison between the posterior distribution of the best fit inclinations for the blurred model with spin equal 1 (red, dotted) and the blurred model with spin 0 (blue, hatched).

2.4 Discussion

The key finding of this work is evidence for the presence of a blurred Compton reflection component in the X-ray spectra of AGN in the CDF-S. This result has been established via fitting of the individual source spectra using their individual redshifts, and does not rely on spectral stacking, except for the purposes of visualization. This has been enabled by the use of the Bayesian spectral fitting procedure BXA, which allows us to perform parameter estimation and model comparison for our faint spectra, accounting for sources of error like statistical and systematic redshift uncertainty, Poisson uncertainty and background contribution. Previous evidence for broad emission has been found abundantly in the X-ray spectra of nearby Seyfert galaxies (e.g. Nandra et al. 2007) and has furthermore been claimed for fainter deep field AGN (e.g. Streblyanska et al. 2005; Chaudhary et al. 2012; Falocco et al. 2013, 2014; Liu et al. 2016), but in other cases has not been confirmed (e.g. Corral et al. 2008, 2011). Our method, which fits individual spectra in the sample using a statistical method that is robust even with low counts, should provide a valid alternative to stacking.

The detection of relativistic emission in these sources is important, because it offers physical insight in to the accretion process in AGN at the peak of the cosmic accretion history at z=0.5–4 (e.g. Aird et al. 2010). The accretion disk in these objects must extend very close to the supermassive black hole - indeed there is tentative evidence for emission within $6R_g$ based on the (mild) preference for a model with a rapidly spinning SMBH. Because the disk fluoresces at these radii in response to intense external illumination, it must therefore be relatively cool, in a relatively low ionization state, and hence of high density. All of this evidence points convincingly towards a standard, radiatively efficient accretion disk (e.g. Shakura et al. 1978) and argues strongly against hot, radiatively inefficient flows (e.g. Narayan & Yi 1994; Hopkins et al. 2009).

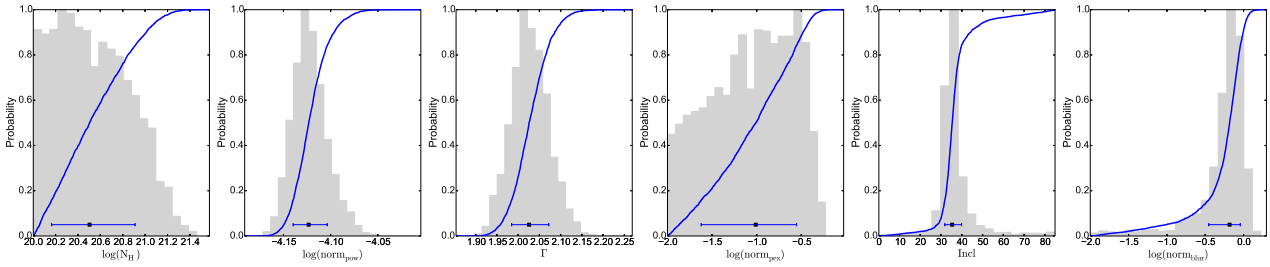

(a) CID 190.

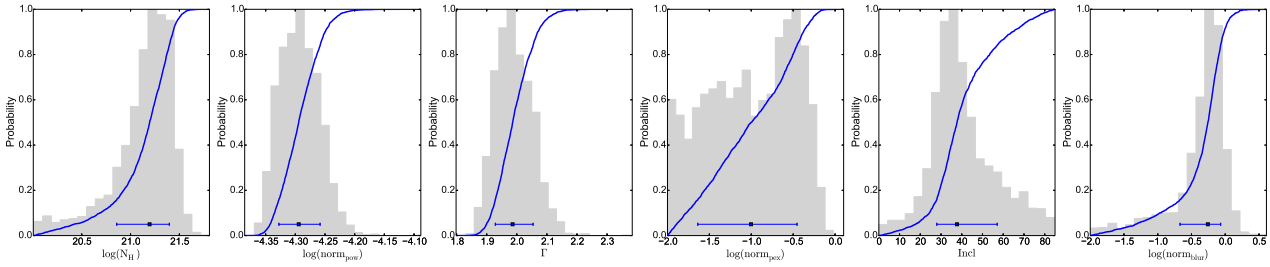

(b) CID 104.

Figure 2.5: *Top*: Marginalized parameters of the blurred model for CID 190. *Bottom*: Marginalized parameters of the blurred model for CID 104. The marginals histogram is plotted in gray and the cumulative distribution function is over-plotted in blue. The inclination angle of the blurred component is $\sim 35^{+5}_{-4}$ degrees for CID 190, while the one of CID 104 is $\sim 37^{+20}_{-10}$ degrees. In both sources the normalization of the narrow component is not well constrained, as is also the case of the column density $\log(N_H)$ of CID 190. The blue error bar indicates the 1 standard-deviation equivalent quantiles.

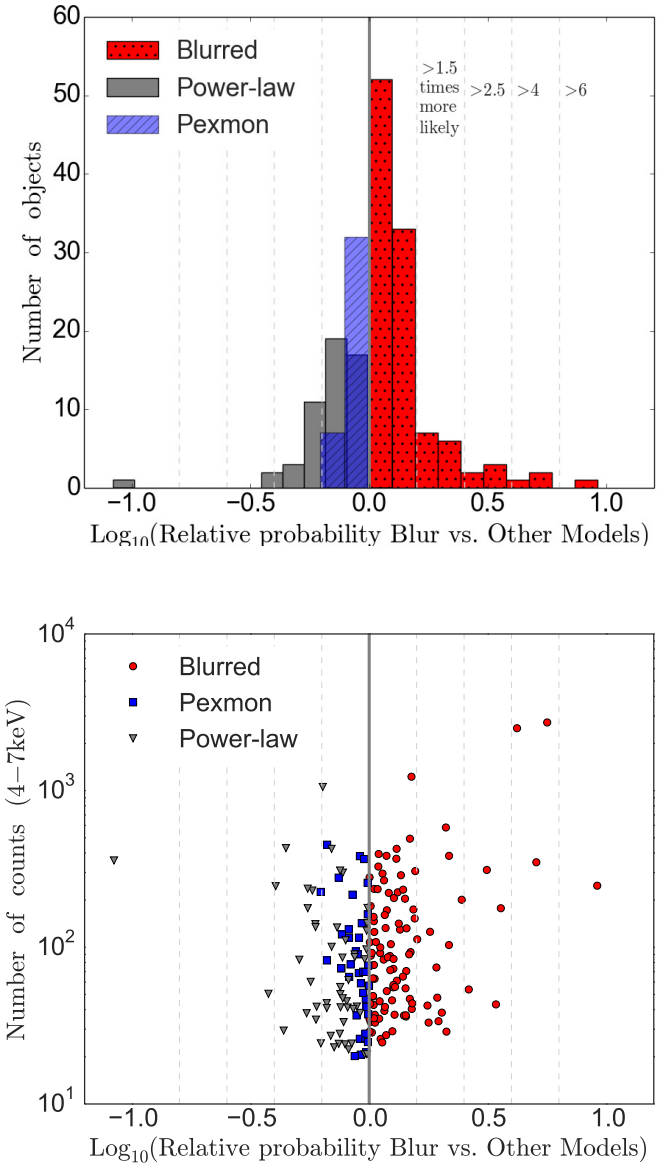

Figure 2.6: *Top*: Relative probability of the broadened model (spin 1) vs. the narrow reflection and the intrinsic emission. The sources are marked in red (dotted) is the model with highest probability is the blurred model 3.2, in blue hatched if the narrow model 2.2 has the highest probability while in gray (solid) if model 2.1 has the highest probability. *Bottom*: Relative probability compared to the sources number of counts in the 4–7 keV. The single sources have such a low SNR that in the majority of the cases the blurred (circles) and the narrow (squares) models are equiprobable, even if the blurred one is slightly preferred. There are a few exceptions, e.g. CID 190 and CID 104, the two brightest sources of the sample. The sources with the power-law model having higher probability are marked as triangles.

Our results further suggest that these black holes may typically be rapidly spinning. While this still needs to be confirmed, it would suggest that these black holes grow via a fairly steady and long-term mode of accretion. Other modes such as "chaotic" accretion King & Pringle (2006) or black-hole black-hole mergers would tend to counteract the spin-up effect associated with long periods of coherent accretion.

While it is certainly premature to consider these conclusions to be robust, they do indicate the tremendous power of X-ray spectroscopy to diagnose physical effects in these faint, growing supermassive black holes, and the future potential of this work. The fitting methods developed here rely not on the quality of the individual spectra, but on the total number of photons in the ensemble of spectra. They are therefore ideally suited to application to the forthcoming *eROSITA* all-sky survey (Predehl et al. 2010; Merloni et al. 2012). The *eROSITA* survey will yield AGN spectra with few counts, but for millions of X-ray emitting objects. Applying our techniques to these spectra will offer important insights into the relationship of the relativistic spectral signatures to other parameters such as accretion luminosity, accretion rate, black hole mass, obscuration and perhaps even larger-scale galaxy properties or large-scale structure environment. A revolution in such studies will later be provided by *Athena* (Nandra et al. 2013), whose unprecedented collecting area will have the potential to reveal relativistic signatures in individual cases, as well as ensemble samples such as those shown here.

2.5 Summary and Conclusions

Using a sample of 123 X-ray observations of AGN with spectroscopic redshift and 76 with photometric redshift from the CDF-S, we have sought to establish whether a relativistic broadened Fe Kα line and Compton reflecting continuum is a common characteristic of X-ray AGN detected in the CDF-S. This has been achieved by fitting the spectra individually, rather than stacking, and then selecting the best fit model via Bayesian model comparison. Our main findings are:

- The Bayesian evidence of the full sample shows that the model containing a relativistically blurred component is preferred over those without such a component.

- The data show a preference for a spinning SMBH, specifically a Schwarzschild SMBH with spin a=0 (`rdblur`) fits the data less well than one with a Kerr SMBH with a=1 (`kdblur`).

- Observations of the the two brightest sources in the sample (CID 190 and CID 104) confirm the results for the sample as a whole, in that the blurred model with a high spin is preferred when fitting their spectra individually.

- The estimated the fraction of objects showing a blurred component is approximately 63%, but this can be considered a lower limit given the low-signal-to-noise ratio of the spectra and the penalization of the more complex blurred model without a disk component.

- Our results imply that the majority of black hole growth in the Universe proceeds via standard, radiatively disk accretion, and demonstrate the great future potential of X-ray spectroscopy to reveal the physics of accretion, out into the high redshift Universe.

Chapter 3

Relativistic accretion disk reflection in AGN X-ray spectra at z=0.5–4: a study of four *Chandra* deep fields

In Chapter 2, we used the Bayesian framework developed by (Buchner et al. 2014) to study the relativistic reflection, in particular the presence of the broad Fe Kα line, in a large sample of 199 AGN observed with *Chandra*. We found that the model containing the a broad relativistic reflection in addition to a narrow reflection from the cold torus is required to describe the data at best. However, the sample was still very limited, since we used only the brightest sources of the CDFS 4Ms. To learn more about the properties of the Fe Kα line we need a larger sample and we need to take into account fainter sources too.

For this reason, in this Chapter we expand the previous work on 199 sources from the CDF-S 4Ms (see Chapter 2, Baronchelli et al. (2018)) to a large sample X-ray spectra from the four deepest *Chandra* surveys: the CDF-S 7s, CDF-N, COSMOS and AEGIS fields.

We confirm that the spectra are best fit by a model containing two Compton reflection components, one from distant material, and the other displaying relativistic broadening, most likely from the inner accretion disk. The degree of relativistic broadening indicates a preference for high black hole spin, but the reflection is weaker than that expected for a flat disk illuminated by a point source. We investigate the Compton reflection signatures as a function of luminosity, redshift and obscuration, confirming an X-ray Baldwin effect for both the narrow and broad components of the iron line. Anti-correlations are also seen with redshift and obscuring column density, but are difficult to disentangle from the Baldwin effect. Our methodology is able to extract information from multiple spectra with low signal-to-noise ratio, and can be applied to future data sets such as eROSITA. We show using simulations, however, that it is necessary to apply an appropriate signal-to-noise ratio cut to the samples to ensure the spectra add useful information.

This work was published by Baronchelli et al. (2020) in Monthly Notices of the Royal Astronomical Society, Volume 498, Issue 4, November 2020, Pages 5284 - 5298.

3.1 Introduction

Active galactic nuclei (AGN) are powered by matter falling onto a supermassive black hole (SMBH) (e.g. Rees 1984), via an accretion disk (e.g. Shakura & Sunyaev 1973; Malkan 1983; Laor & Netzer 1989).

In addition to the direct disk emission AGN emit up to 20% of their bolometric luminosity in the X-ray waveband (e.g. Elvis et al. 1994). The X-ray emission is produced via Compton upscattering by a hot corona (e.g. Haardt & Maraschi 1991) which illuminates the innermost regions of the accretion disk. The X-ray emission can be backscattered and induce fluorescence in the inner disk (e.g. Fabian et al. 1989; George & Fabian 1991), which leaves imprints due to the large velocities and gravitational field. Hence, the analysis of the X-ray spectrum from AGN allows us to probe general relativity and investigate the behaviour of matter in extreme gravitational fields, only a few gravitational radii from SMBHs (Reynolds & Nowak 2003; Psaltis 2008).

In many of these systems a strong iron (Fe) Kα fluorescent line is observed (Nandra & Pounds 1994). The Fe Kα feature peaks around 6.4 keV in the rest frame. Part of the emission comes from material at scales of several parsec, most likely the torus envisaged in orientation-dependent unification schemes (e.g. Krolik et al. 1994; Ghisellini et al. 1994) and hence the line is relatively narrow, with velocities of a few $\sim$ 100 km s^{-1} (Yaqoob & Padmanabhan 2004; Nandra 2006). As discussed above, the remainder of the iron Kα feature is emitted in a region of the accretion disk in the proximity of the SMBH, and it is broadened and skewed by relativistic effects, e.g. gravitational redshift and relativistic Doppler shifts (Fabian et al. 1989; Laor 1991; Fabian et al. 2000; Risaliti & Elvis 2004). The shape and width of the line and the amount of broadening can help us gain information on the geometry of the system and the spin of the SMBH (Brenneman & Reynolds 2006). Constraining the distribution of black hole spins in the whole AGN population would help determine the nature of the accretion history of the SMBH, for example by allowing us to distinguish whether the SMBH grew mostly through mergers, continuous, or "chaotic" accretion (King & Pringle 2006; Volonteri et al. 2013).

Strong, relativistically broadened Fe Kα lines are observed in a number of individual, bright Seyfert galaxies in the nearby Universe, e.g. MCG-6-30-15 (Tanaka et al. 1995; Fabian et al. 2002) and NGC 3516 (Nandra et al. 1999). Indeed such emission is found to be common in the nearby AGN population (**?**), though the evidence for such a component is not universal (Nandra et al. 2007; de La Calle Pérez et al. 2010). This is probably due to fact that the strength of the broad reflection component is weaker than that expected from a standard accretion disc illuminated by a point source (Nandra et al. 2007), meaning that very high signal-to-noise ratio (S/N) is needed to detect it convincingly Mantovani et al. (2016); de La Calle Pérez et al. (2010).

The fact that the reflection is weaker than expected, and differs in strength from source to source, can nevertheless reveal important information about the system such as the geometry. A well known effect of this type is the X-ray Baldwin or Iwasawa-Taniguchi effect Iwasawa & Taniguchi (1993) where the equivalent width of the iron line decreases with luminosity. This effect has been observed for the narrow (Nandra et al. 1997b; Page et al. 2003) and broad (Nandra et al. 1997b) components of the line.

Clearly it is then important to characterize the iron line emission of a representative sample

of AGN, including more typical objects at higher redshift. There are a few observations of relativistic broadened Fe Kα lines at high-redshift, sometimes thanks to studies of lensed Quasars (e.g. Chartas et al. 2012; Dai et al. 2019). The ubiquity or otherwise of the broad features in samples of typical AGN beyond the local Universe is hard to establish, however, given the faintness of the targets. The deepest X-ray surveys offer the opportunity to investigate this issue, and several attempts have been made to use deep surveys to infer the properties of a population of AGN and to verify the ubiquity of feature like the broadened Fe Kα line in a population of AGN (Comastri et al. 2004; Brusa et al. 2005; Streblyanska et al. 2005).

Most past studies have relied on stacking of large samples of low count X-ray spectra (e.g. Streblyanska et al. 2005; Chaudhary et al. 2012). By stacking, one may be able to infer the population properties in cases where fitting individual spectra would not yield meaningful results. Evidence for broadening of the Fe Kα line has been reported in several stacking studies, such as Chaudhary et al. (2012) and Falocco et al. (2013, 2014). Corral et al. (2008), however, combined the rest-frame spectra of 600 *XMM-Newton* type-1 AGN without finding compelling evidence for a relativistic broadening of the Fe Kα line. Some of this work showed, however, that stacking the spectra might induce artificial broadening of the Fe Kα in samples with a wide redshift distribution (Chaudhary et al. 2012). This problem was addressed by Falocco et al. (2012, 2013, 2014) and Liu et al. (2016) who compared the stacked spectra to simulations. While this approach can increase confidence in the existence of the broadened features, the simulations require an assumption about the true underlying spectrum.

In our previous work (Baronchelli et al. 2018) we employed an alternative technique to characterise the and the iron line and reflection properties of a large sample of AGN, whose X-ray spectra individually have low S/N ratio. Instead of fitting a stacked spectrum, we used the Bayesian X-ray Analysis (BXA) software (Buchner et al. 2014) to fit the individual spectra of low S/N sources. We then combined the Bayesian evidence for the putative broad reflection component to establish whether or not it was present in the whole sample. The analysis was performed on a sample of 199 hard X-ray selected sources from the *Chandra* Deep Field South 4Ms exposure, and revealed strong evidence for a relativistically broadened X-ray reflection component from the accretion disk. The properties of the reflection also implied a preference for a maximally spinning SMBH, as compared to a non-rotating Schwarzschild black hole.

In this work, we expand the study of Baronchelli et al. (2018) to a total of four *Chandra* fields. Our aim is to investigate further the prevalence of the Fe Kα and reflection features within typical AGN up to $z = 4$, and characterize their properties. With our expanded sample, we aim to confirm our previous results, and investigate the dependence of the reflection strength with other parameters such as the luminosity, redshift and obscuration.

The paper is structured as follows: in Sect. 3.2, we describe the data used in this work, and our methods of spectral and statistical analysis. The results of the work are reported in Sect. 3.3 and interpreted and discussed in Sect. 3.4. Sect. 3.5 summarises our results and presents our primary conclusions.

Throughout this work, we adopt Ω_m= 0.272, Ω_Λ= 0.728, and H_0 = 70.4 km s^{-1} Mpc^{-1} (Komatsu et al. 2011).

Table 3.1: Number of selected sources and summed counts in in the 1–8 keV observed frame for the individual fields, and for the combined sample. The information is also given for the samples restricted to S/N> 7 described in the text. The source and total counts are calculated with the SHERPA tool `calc_data_sum`.

		Total	CDFS 7Ms	CDFN	AEGIS	COSMOS
ALL						
	Number of sources	2237	199	376	540	1122
	Source counts	655951	313914	127563	119462	95011
	Total counts	759356	364635	148096	140087	106538
S/N ≥ 7						
	Number of sources	2165	198	349	539	1079
	Source counts	654899	313864	126922	119448	94663
	Total counts	755815	364472	145604	140033	105706

3.2 Sample and Method

3.2.1 Data

In this work we analyse four of the deepest fields observed by *Chandra*, the 7Ms exposure of the *Chandra* Deep Field South (CDFS), the *Chandra* Deep Field North (CDFN), AEGIS and the COSMOS fields. The long exposures in these fields ensure that meaningful spectral information can be extracted for typical AGN at moderate redshifts ($z = 0 - 4$) which dominate the accretion history of the Universe (e.g. Aird et al. 2010; Buchner et al. 2015). In our analysis, we focus on the properties of the iron Kα emission line and hard X-ray reflection continuum from Compton thick structures surrounding the AGN, such as the accretion disk and molecular torus. We hence use a hard X-ray selection (> 2 keV) for all fields to ensure that meaningful spectral constraints can be obtained using these features. Here we summarise the data and sample selection in each field:

The *Chandra* Deep Field South

The CDFS (Luo et al. 2017) is, with a nominal total exposure time of ~7 Ms, the deepest of all the *Chandra* surveys, and indeed the deepest X-ray survey of all. While it reaches extremely faint fluxes, it covers a relatively small area of ~0.13 deg^2 The CDF-S 7Ms is a collection of observations performed over multiple epochs between Oct 14, 1999 and Mar 24, 2016.

All 102 observation used ACIS-I, which offers spectral imaging over an approximataely 17 × 17 arcmin field of view and is often used for surveys.

We limit our CDFS sample to the 199 hard X-ray (2 – 7 keV) selected AGN at redshift z < 4 previously studied in Baronchelli et al. (2018) and Buchner et al. (2014). These were selected form the source catalog of Rangel et al. (2013), which was based on the 4Ms *Chandra* exposure. In the current analysis, however, we extract the spectra of the 4Ms sources from the deeper 7Ms

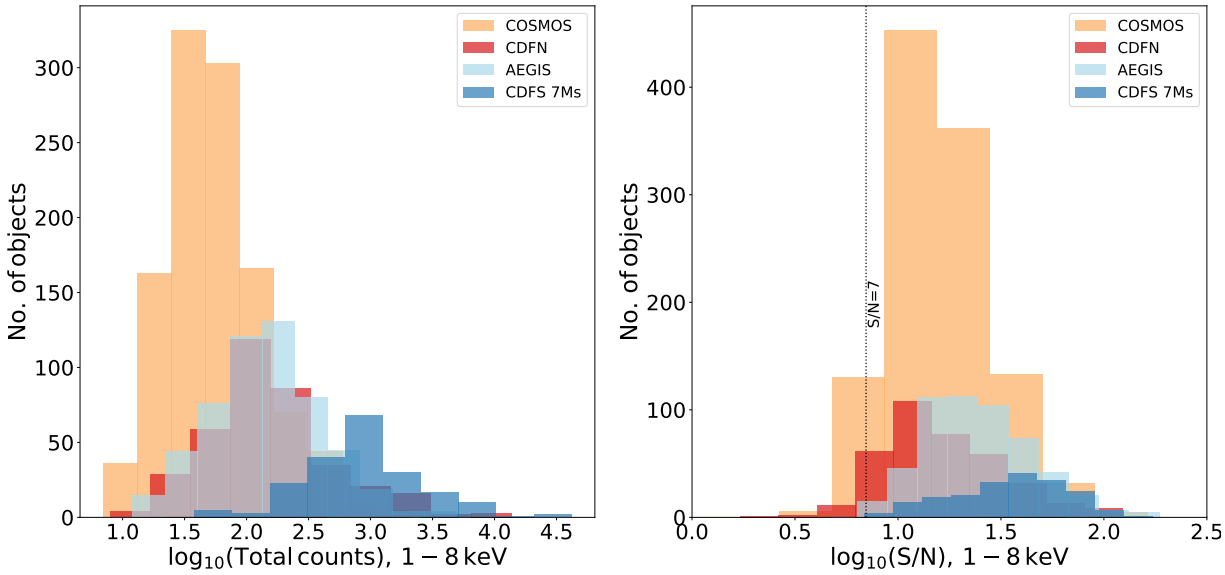

Figure 3.1: *Left*: Total counts (source counts plus background counts). *Right*: Signal to noise ratio of the four samples COSMOS, AEGIS, CDFN and CDFS 7Ms.

exposure. The 7Ms spectra of these 199 sources contain a total of 313914 source counts in the observed 1–8 keV energy band, which is most relevant for our analysis. All of these sources have a redshift measurement, the majority of which are spectroscopic redshifts for which we adopt a single value. For the remaining 38% of these sources (76/199) photometric redshifts and their probability distributions from Hsu et al. (2014) were used. These are specially tailored for AGN, and are based on the methods of Salvato et al. (2009) and Salvato et al. (2011).

The *Chandra* Deep Field North

The CDFN is a field which is has received a *Chandra* exposure of 2 Ms over a sky area of ~0.12 deg^2 It comprises 20 different pointings taken between November 1999 and February 2002. We use the source catalog from Xue et al. (2016) to obtain the redshift values and to exclude stars. We analyse a sub-sample of 376 sources with redshift information from the 411 hard selected (2–7 keV band) sources in Xue et al. (2016). Of these sources, 159 have spectroscopic redshift (Xue et al. 2016). The spectra contain a total of 127563 source counts in the 1–8 keV energy band. The PDFs of the photometric redshift for the CDFN are not available, thus we used the preferred redshift adopted in Xue et al. (2016). The fact that the photo-z PDFs are not available for the CDF-N means that, in some cases, an inaccurate redshift will be adopted in the spectral fit. On average, this will have the effect of reducing the significance when comparing the true underlying model with any other model, so should be conservative with respect to the significance of the results presented below. Because a single value for the redshift is used, it will also result in an overly narrow posterior distributions for those sources. This would also tend to lead to an overestimate of the intrinsic scatter and an underestimate of the statistical uncertainty of the

mean values derived for the sample.

AEGIS-X

The AEGIS-X Deep survey (Nandra et al. 2015) is the result of deep *Chandra* imaging of the central region of the Extended Groth Strip. The survey encompasses an area of approximately 0.29 deg^2 with a nominal exposure time of 800 ks. AEGIS-X is currently the third deepest *Chandra* blank field survey after the *Chandra* Deep Fields (CDF). While being shallower than the CDFs by a factor of ∼2–3 it covers an area ∼ 3 times larger. We use the source catalog from Nandra et al. (2015), selecting as a parent sample the sources detected in the 2 − 7 keV band, comprising 572 sources. After removing the sources identified as stars in Buchner et al. (2015), we select a sub-sample of 540 sources with redshift information from the original 572 sources in the hard selected sample, with a total of 119462 source counts in the 1–8 keV energy range. Of these 540 sources, 202 (∼ 37%) have a spectroscopic redshift. For the remainder, Nandra et al. (2015) provide photometric redshifts tailored for AGN, and their probability distribution functions, which we use in the spectral fitting.

COSMOS

The *Chandra* COSMOS Legacy survey spans an area of 2.2 deg^2 on the sky. The central 1.5 deg^2 has a nominal exposure of ∼ 160 ks while the surrounding regions are nominally exposed with ∼ 80 ks depth (Civano et al. 2016). This makes it the largest area survey in our complication, but also the shallowest. We study the hard band selected sample from Civano et al. (2016) after removing the sources identified as stars in Buchner et al. (2015), which comprises 1122 objects with a total of 95014 source counts in the 1-8 keV energy range. Of these sources, 534 have spectroscopic redshift, while the remaining 53% have accurate photometric redshifts and photo-z probability distributions from the work of Salvato et al. (2009).

3.2.2 Combined sample

The parent sample for this study, combining all four fields, comprises a total of 2237 sources (See Table 3.1). Figure 3.1 shows the distribution of counts and S/N of our sample. We calculate the S/N using the formalism of Li & Ma (1983) (see also Vianello (2018)), which takes into account the Poisson nature of both the source and background count measurements. In particular we use the function `poisson_poisson` from the python library `gv_significance` developed by Vianello (2018). The sample spans a wide range of both total counts and signal-to-noise ratio. Numerically it is dominated by sources from the COSMOS survey, which has the largest area, but the objects from the deepest field, the CDF-S, have the highest number of counts and S/N overall. The right hand panel of Fig. 3.1 shows a vertical line at S/N=7. We use sub-samples cut at this S/N in the subsequent analysis, as discussed below, and the number of sources and source counts obtained after applying this S/N cut are shown in Table 3.1.

The luminosities L_X, defined in the 2–10 keV energy range, and redshifts of the selected sources are presented in Figure 3.2, which also shows the S/N split sub-samples. The luminosities

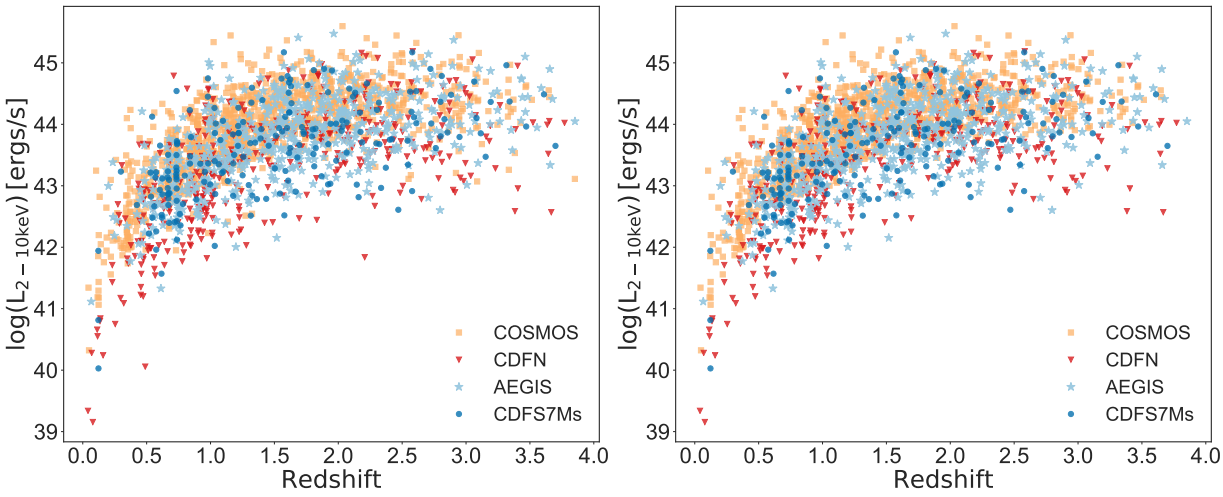

Figure 3.2: 2–10 keV Luminosity-redshift distribution for the full sample (*Top*) and S/N > 7 subsample (*Bottom*). We used the median of the absorption-corrected luminosity posterior probability from the model `zwabs*(zpowerlw + pexmon)`. The redshift used for the plots is the reported value from the original survey catalogs.

.

were calculated from the spectral fits described below and corrected for galactic and intrinsic absorption. The sample covers a broad redshift range up to $z \sim 4$, and the bulk of the sample covers the luminosity range $\log L_X = 42 - 45$ erg/s[1], with just a very few low redshift sources fainter than this. The sample becomes increasingly incomplete at luminosities below $\log L_X = 43$ erg/s above a redshift of about 1.

3.2.3 Spectral Extraction

We extracted the spectra of the sources using the software package *ACIS Extract* (AE) (Broos et al. 2010, 2012). AE was developed to automate as much as possible the analysis of X-ray data taken with the *ACIS* instrument of *Chandra*. It is well suited for our application as, given a source catalog, spectra can be extracted from multiple observations of the same field. As input files, AE requires the Level 2 event list of the observations, the exposure maps and aspect histograms corresponding to the field of view of the event data, the aspect solution file covering the time range of the observations and the mask file of the observations. We produced these files with a combination of the CIAO 4.10 (Fruscione et al. 2006) and FTOOLS 6.25 (Blackburn 1995) software.

The process of extracting spectra using AE can be summarized in four steps. First, the AE tool *ae_make_catalog* builds extraction regions sized to encompass 90% of the local point

[1]The log here represents the logarithm in base 10 ($\log_{10}$).

spread function (PSF) but small enough to avoid overlaps in crowded regions. Secondly, the tool *ae_standard_extraction* extracts source and background spectra of the sources in the catalog. Note that for data taken at -110C on certain CCDs the event file will not be corrected for charge transfer inefficiency (CTI) and AE will be set to use the CIAO tool *mkrmf* instead of the default *mkacisrmf* to build the RMF files. The next step uses *ae_adjust_backscal_range* to analyze the source's existing background extraction region and to choose a target background scaling range individually for each source. The process of extracting background and choosing a scaling range has to be repeated until the scaling range is stable. Finally, AE merges the observations combining the extraction from all the ObsIds and performing the photometry.

We produced the appropriate input files for AE following the method presented in (Georgakakis et al. 2011). The final data products are the source and background spectra together with RMF and ARF files.

3.2.4 Model fitting and model comparison

Four physically justified models are considered to represent different scenarios for the major gas structures surrounding the central black hole. The first model is an absorbed power-law, `zwabs*zpowerlw` in XSPEC terminology, which describes the emission from an X-ray corona behind a screen of obscuring gas. In the second model we add a non-relativistic reflection component to the simple absorbed power-law, `zwabs*(zpowerlaw+pexmon)`, to represent reflection from distant material such as the obscuring torus. We chose the `pexmon` model (Nandra et al. 2007) to describe the reflection component since it combines a exponentially cutoff power-law emission reflected by neutral material (`pexrav`; Magdziarz & Zdziarski (1995)) with self-consistently generated Fe Kα, Fe Kβ, Ni Kα and Fe Kα Compton shoulder emission (George & Fabian 1991; Matt 2002). The third and the fourth model add a relativistically broadened reflection component to the second model, as expected from an accretion disk. This last component is modelled by convolving a narrow reflection spectrum with a convolution model to represent the expected Doppler and gravitational shifts expected from an accretion disk. Specifically, we use the the `kerrconv(pexmon)` model (Brenneman & Reynolds 2006). The `kerrconv` allows the BH spin to be a free parameter. However, to avoid having unnecessarily many free parameters in the broadened reflection model we constrain our analysis by fixing the spin parameter to the two special cases of spin $a = 0$ (Schwarzschild metric, model three) and maximally spinning $a = 0.998$ (model four). The parameter priors are chosen to be consistent with Baronchelli et al. (2018), except for the parameter describing the inclination angle of the broad component, that in the current work is chosen to be uniformly distributed in cosine space (see Table 3.2). In Table 3.2 we list the chosen model parameters for the components `xszwabs`, `powerlaw`, `pexmon` and `kerrconv(pexmon)`. For the parameters allowed to vary, we list the minimum and maximum value of the prior distributions. The normalization parameters and the N_H are chosen to be uniform in logarithmic space, the inclination angle in `kerrconv` is uniform in cosine space, while all the other parameters are uniform in linear space. When only the photometric redshift of the source is available, we use the probability distribution function (PDF) produced using the SED fitting procedures and templates from Salvato et al. (2009) and Salvato et al. (2011) to take into account of the uncertainty of the photometric redshift estimation. The exception is the

Table 3.2: Parameter description for model `zwabs*(zpowerlw + pexmon + kerrconv(pexmon))` . The model component blur represents the model kerrconv. We fix the spin parameter to the values 0 or 0.998 depending on the case we want to analyze. The model has six free parameters: the column density N_H, the photon index, the inclination of the broad component and the three norms. The strength of the blurred reflection component component R_{blur} is measured relative to the power law and is defined as the ratio of the normalization of the blurred pexmon component (A_{blur}) to that of the power-law (A_{pow}). The parameters that have units are [N_H] = atoms cm^2, [foldE] = keV, [Incl] = deg, r_{br} in gravitational radii and R_{in} and R_{out} in units of the radius of marginal stability.

Comp.[a]	No.[b]	Name[c]	Min	Max	Fix val.	Free
zwabs	1	log(N_H)	20	26	-	yes
	2	Redshift	-	-	z	-
zpowerlw	3	PhoIndex	1.1	2.5	-	yes
	4	Redshift	-	-	link to 2	-
	5	log A_{pow}	-10	1	-	yes
pexmon	6	PhoIndex	-	-	link to 3	-
	7	foldE	-	-	800	-
	8	rel_refl	-	-	-1	-
	9	redshift	-	-	link to 2	-
	10	abund	-	-	1	-
	11	Fe_abund	-	-	1	-
	12	Incl	-	-	60	-
	13	log(R_{pex})	-2	1	log $\frac{A_{pex}}{A_{pow}}$	yes
kerrconv	14	Index1	-	-	3	-
	15	Index2	-	-	3	-
	16	r_{br}	-	-	6	-
	17	Rin	-	-	1	-
	18	Rout	-	-	400	-
	19	Spin	-	-	0/0.998	-
	20	cos(Incl)	0	1	-	yes
pexmon	21	PhoIndex	-	-	link to 3	-
	22	foldE	-	-	1000	-
	23	rel_refl	-	-	-1	-
	24	redshift	-	-	link to 2	-
	25	abund	-	-	1	-
	26	Fe_abund	-	-	1	-
	27	Incl	-	-	link to 17	-
	28	log(R_{blur})	-2	1	log $\frac{A_{blur}}{A_{pow}}$	yes

[a]Model component.
[b]Parameter number.
[c]Parameter name.

CDFN for which the photometric redshift PDFs are not available, and we use a single value for the redshift.

We fit a background model simultaneously to the data, following Buchner et al. (2014), instead of subtracting the background. We fit the *Chandra* background model provided in BXA to all the background spectra and then we include the background model with best fit parameters frozen in the model of the source spectra (see also Buchner et al. 2014; Baronchelli et al. 2018). As discussed in the introduction, we do not stack the spectra to determine the average properties of the sample, but instead fit each source individually and then infer the properties of the sample by combining the information from these individual fits.

Table 3.3: Comparison of the Bayesian evidence for our four models for the CDFS 7Ms, CDFN, AEGIS, COSMOS and the full sample. In each column, the values of log(Z) for each model are normalized by the log(Z) of the model with highest evidence. Thus in this table, the model with highest evidence is identified by a value of log(Z) = 0. We fit the models in the observed frame energy range 1 – 8 keV.

	Model [a]	Total log(Z)[b]	CDFS 7Ms log(Z)[b]	CDFN log(Z)[b]	AEGIS log(Z)[b]	COSMOS log(Z)[b]
S/N ≥ 0						
	`zwabs*(zpowerlw)`	-438.6	-133.2	-103.8	-101.0	-110.1
	`zwabs*(zpowerlw+pexmon)`	-26.8	-10.2	-19.7	-7.2	0
	`zwabs*(zpowerlw+pexmon+kerrconv0(pexmon))`	-6.3	-2.9	-2.3	-3.1	-10.6
	`zwabs*(zpowerlw+pexmon+kerrconv1(pexmon))`	0	0	0	0	-8.8
S/N ≥ 7						
	`zwabs*(zpowerlw)`	-437.1	-133.6	-102.1	-101.0	-109.5
	`zwabs*(zpowerlw+pexmon)`	-27.0	-10.4	-19.2	-7.2	0
	`zwabs*(zpowerlw+pexmon+kerrconv0(pexmon))`	-6.6	-3.0	-2.5	-3.1	-10.0
	`zwabs*(zpowerlw+pexmon+kerrconv1(pexmon))`	0	0	0	0	-8.2

[a] Model components.
[b] Logarithm of the Bayes evidence of the full sample normalized to the largest evidence.

3.2.5 Bayesian X-ray Analysis

The *Bayesian X-ray Analysis* (BXA) (Buchner et al. 2014) package is a Bayesian framework to determine the best fit parameters and their posterior distribution for X-ray spectra. BXA applies `PyMultinest` (Buchner et al. 2014), a python wrapping of an implementation of the nested sampling algorithm (MULTINEST) (Feroz & Hobson 2008) combined with SHERPA or XSPEC to compute the Bayesian evidence Z for X-ray data and hence parameter constraints. The Bayesian evidence Z is the integral of the likelihood over the prior and can be interpreted as the probability $P(D|M)$ of the model M given the data D marginalized over the model parameters θ.

$$Z = P(D|M) = \int L(\theta)P(\theta|M)d\theta, \tag{3.1}$$

MULTINEST Feroz & Hobson (2008); Feroz et al. (2009, 2013) provides an efficient approximation to this integral. This algorithm samples a number of live points in the parameter prior space evaluating the likelihood of the model for every point. At every step, the live point with lowest likelihood will be replaced by a newly sampled point until the algorithm converges to the highest likelihood value. MULTINEST is particularly specialized to deal efficiently with multimodal distributions by using a recursive clustering algorithm and proposal regions in the shape of ellipsoids.

To perform model comparison, we assume that all sources are described by the same model. We calculate the total evidence for that model by adding the $\log(Z)$ (see also, Buchner et al. 2014; Baronchelli et al. 2018) values from the individual fits. This allows one to compare the total evidence of the sample for different models. The difference in the logarithmic evidence then corresponds to a Bayes factor (BF), which can be used to discriminate between the models. A commonly used way to interpret the BF values is the Jeffrey scale, which strengthens the choice of one model over the other approximately every time that the logarithm of the BF increases by one in natural logarithmic units (Robert et al. 2009). However, Bayes factors are continuous quantities and such discretisations should not be over-interpreted (Nesseris & García-Bellido 2013). In (Baronchelli et al. 2018), we verified with simulations that the Bayes factors scatter around one ($\Delta \log Z \approx 0$) for low signal-to-noise data.

3.3 Results

3.3.1 Initial fitting and S/N effects

We first fit the total sample of 2237 sources with BXA to calculate the Bayesian evidence Z for the four models described in Section 4.2. We fit each source with each of the models individually and use the Bayes factor (BF) method to compare the models and determine which one provides the better fit. The single sources are generally too faint to significantly favour one model over the others. Instead, as discussed above, we combine the Bayesian evidence from the individual source fits to obtain the evidence for the full sample (Buchner et al. 2014; Baronchelli et al. 2018).

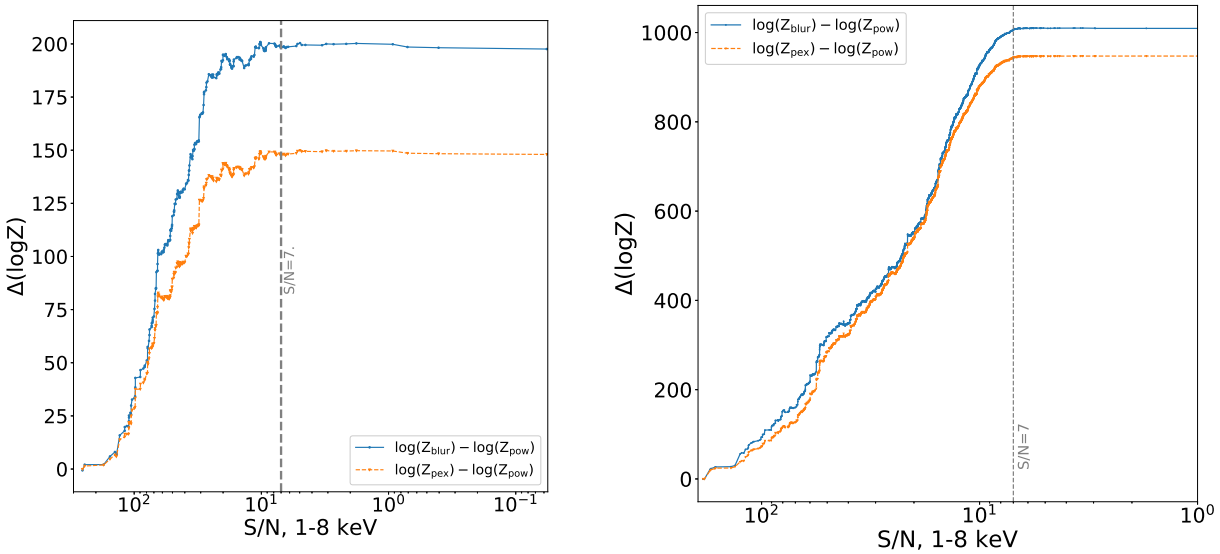

Figure 3.3: Cumulative evidence of the full sample for decreasing S/N for the full sample (*Bottom*) and the simulated sample (*Top*). The circular points (blue, solid line) show the cumulative evidence for the blurred model normalized by the evidence of the simple power-law. The triangles (orange, dashed line) show the cumulative evidence for the narrow model normalized by the evidence of the simple power-law. For the full sample the blue curve remains above the green curve. The gray dashed vertical line at S/N = 7 shows the S/N limit below which adding the evidence of the single sources to the total value does not add further information.

As can be seen in Table 3.3, the Bayesian evidence for the total sample shows a strong preference for the model including both narrow and broad reflection components, with a maximally spinning black hole preferred over a Schwarzschild solution. This preference is also found in the field-by-field subsamples, with the exception of the COSMOS field. Here the preferred model is that without the blurred reflection component. We discuss this result further below, but note here that there are a number of differences between the COSMOS sample and the remainder of the fields. One such difference is that, as shown in Fig 3.1, the COSMOS sources typically have lower signal-to-noise ratio than the sources in the other fields. This raises the possibility that, below a certain S/N threshold, the spectra become insensitive to the broad reflection component and do not add information about the presence or properties of that component.

This hypothesis is borne out by the data. Fig. 3.3 (top) shows the cumulative evidence as a function of signal-to-noise ratio for the sample. The evidence rises rapidly when adding sources with high S/N, but then flattens off and eventually becomes approximately horizontal, showing that the lowest quality spectra are not adding additional information/evidence. To estimate at which S/N the source will not add further information to the total evidence of the sample, we perform a set of simulations using the `fakeit` tool of XSPEC (Arnaud 1996).

We simulate a sample of 300 sources using the ancillary files (ARF and RMF), the background spectra and the redshifts from the AEGIS sample. As a first step to simulate a sample of spectra, we have to choose an input model that will define the spectral shape of the simulations. Since we are interested in studying how our method would perform on a sample of relativistic broadened spectra at different S/N, we chose to simulate the spectra using the fourth model. We simulate the sources so that the total number of net counts is comparable with the one of CDFS 7Ms sample.

We fit the simulated sample with the four models described in Section 3.2.3. In the bottom panel of Fig. 3.3, we show the cumulative evidence ratios $\log(Z_{blur}) - \log(Z_{pow})$ and $\log(Z_{pex}) - \log(Z_{pow})$ that represent the cumulative distributions of the broad and narrow models normalized by the evidence of the simple powerlaw. It can be seen that the two curves start to flatten below S/N$\sim$ 7, very similar to what is seen with the real data. We thus conclude that below this S/N value, little additional information is being added about the properties of the reflection, and henceforth restrict our analysis to a subsample with S/N$>$ 7. The number of sources meeting this S/N criterion are shown in Table 3.1.

3.3.2 Compton reflection properties of the sample

The results of the model comparison for the S/N-censored sample are also given are given in Table 3.3. The results are, in fact, rather similar to the full sample, as the number of very low S/N ratio sources is small. More specifically, we find that the BF method selects the model including both broad and narrow reflection components to be the best fitting model in the CDFS 7Ms, CDFN and AEGIS fields. For the COSMOS field, the BF method selects the model with only distant reflection as the best-fitting model over the more complex model with both narrow and broad reflection. Considering the total sample, comprising all four fields, the evidence for the broad reflection is very strong. The difference in the logarithmic evidence can be interpreted like a probability difference. Thus, we can see from Table 3.3 that the model containing a blurred

Table 3.4: Same as Table 3.3 but adding a model, `zwabs*(zpowerlw+kerrconv(pexmon))`, with a broad reflection component and no narrow reflection to the comparison for the COSMOS field. In each column, the values of log(Z) for each model are normalized by the log(Z) of the model with highest evidence. Thus in this table, the model with highest evidence is identified by a value of log(Z) = 0. We fit the models in the observed frame energy range 1 – 8 keV.

Sample/Model [a]	COSMOS log(Z)[b]
All	
`zwabs*(zpowerlw+kerrconv1(pexmon))`	-2.1
`zwabs*(zpowerlw+pexmon)`	-1.7
`zwabs*(zpowerlw+kerrconv0(pexmon))`	0
S/N ≥ 7	
`zwabs*(zpowerlw+kerrconv1(pexmon))`	-2.3
`zwabs*(zpowerlw+pexmon)`	-2.2
`zwabs*(zpowerlw+kerrconv0(pexmon))`	0

[a] Model components.
[b] Logarithm of the Bayes evidence of the full sample normalized to the largest evidence.

component is selected to be $10^{26.8}$ more probable than the scenario with only a narrow reflection component to describe the sample with S/N larger than 7. The total evidence also shows that the model with a maximally spinning (Kerr) black hole has a probability $10^{6.6}$ of being preferred over a non-rotating (Schwarzschild) solution, again seen also in the individual fields with the exception of COSMOS.

The fact that the COSMOS field shows a preference for narrow reflection only in the evidence comparison shown in Table 3.3 does not necessarily imply that broad reflection is not present in the COSMOS source population. This is because we test for the presence of the broad reflection *in addition* to narrower reflection from more distant material, e.g. the torus. As the model with broad reflection has more free parameters, this additional complexity is penalised in the evidence comparison. We therefore performed an additional test by fitting the spectra also with a model with a blurred reflection component but no additional narrow reflection component (see Table 3.4). This then tests whether there is evidence for broad reflection as an alternative to the narrow reflection. According to this test the preferred model is that with a blurred reflection component with a non-rotating (Schwarzschild) black hole. The preference for this model over the narrow reflection or maximally-spinning black hole is, however, marginal. We conclude that, while the COSMOS data are of sufficient quality to confirm the presence of Compton reflection in the spectra, they are not able to distinguish the properties of the reflection e.g. whether it is broad or narrow, or if broad the value of the black hole spin implied. Based on the fields with higher S/N ratio spectra, however, it seems most likely that both components are present also in the COSMOS data.

The average strength of both the narrow and broad reflection components, as measured by

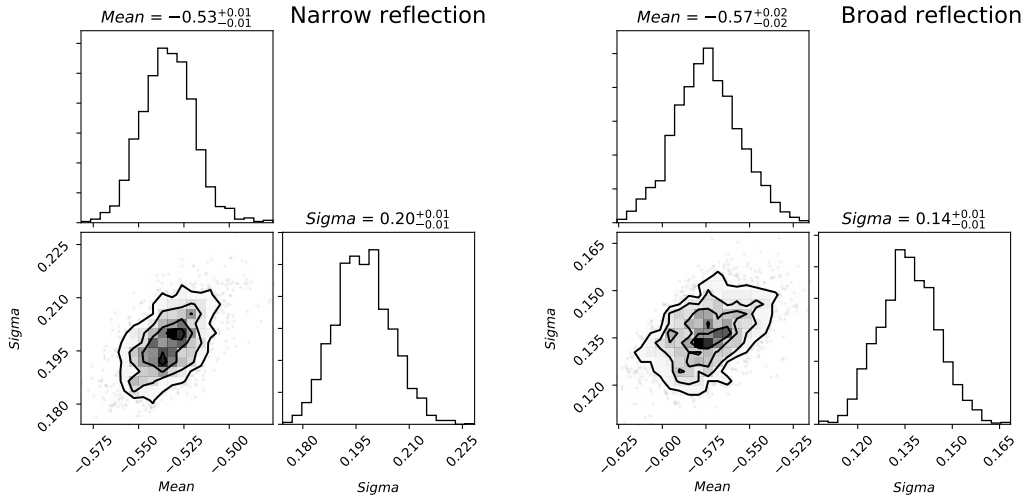

Figure 3.4: Corner plots of the mean and sigma of the population of log(R) values for narrow (*left*) and broad (*right*) reflection component. These result were calculated using the method explained in Appendix 3.6.1.

the R parameter, is an important diagnostic of the system, as it depends on the geometry and, in the case of the broad reflection, potentially also on relativistic effects close to the black hole (e.g. Miniutti & Fabian 2004). The task of calculating the mean and sigma of the underlying parent population that describes the R value is not trivial, however, since the posterior distributions for this parameter are not always well described by a normal distribution. To address this, we us a Hierarchical Bayesian model (HBM), described in detail in Appendix 3.6. For a sample it models the intrinsic log(R) distribution of the sample as a Gaussian. Taking into account the posterior uncertainties on each individual object, the HBM fit returns mean and standard deviation σ of the distribution. The results are shown in Fig 4.7. Applying the HBM to sources with S/N>7 from all fields, we find a mean of $\log(\mathrm{R_{pex}}) = -0.53$ (thus, $R_{\mathrm{pex}} = 10^{-0.53} = 0.30$) with spread $\sigma_{\log(\mathrm{R_{pex}})} = 0.2$ for the narrow reflection component and mean of $\log(\mathrm{R_{blur}}) = -0.57$ (thus, $R_{\mathrm{blur}} = 10^{-0.57} = 0.27$) with spread of $\sigma_{\log(\mathrm{R_{blur}})} = 0.14$ for the blurred reflection component. The population mean values obtained with the HBM for the reflection fraction are similar for the narrow and broad components. The strength of the blurred reflection component in particular is smaller than would be expected from a flat disk illuminated by a point source, as has been found previously (Nandra et al. 2007). Both R values also show a significant spread of ~ 0.2 dex, indicating there is considerable diversity in reflection strength within the population.

3.3.3 Dependence on other parameters

Our expanded sample compared to that of Baronchelli et al. (2018) gives a more robust detection of the reflection components and thus offers the opportunity to investigate any dependence of the reflection on other parameters. To this end, we computed the fraction of sources with S/N > 7 showing $Z_{blur} > Z_{pex}$. This is shown in Figure 3.5 as function of luminosity, redshift and $\mathrm{N_H}$ bins.

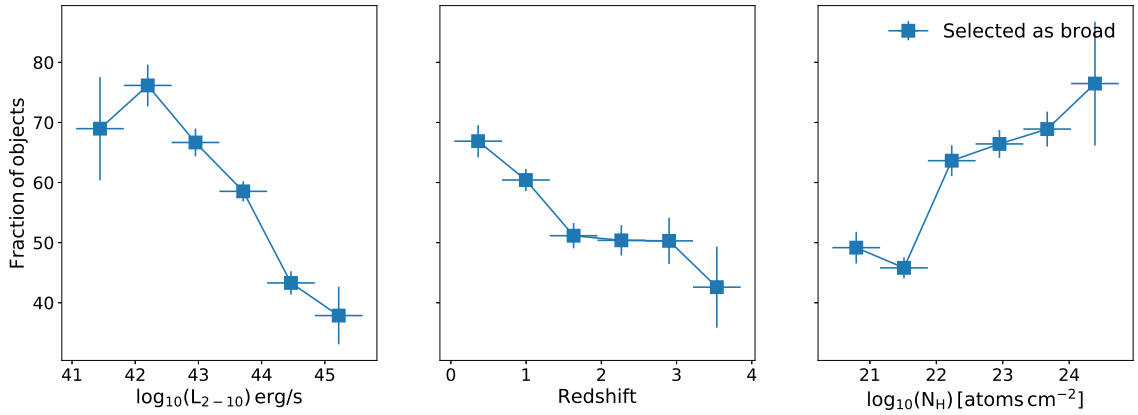

Figure 3.5: Fraction of sources in the sample with S/N≥7 best fitted by a model with broad reflection component as a function of luminosity (*right*), redshift (*middle*) and column density N_H (*left*). The fraction decreases with higher luminosities hinting that an anti-correlation with the Fe Kα line EW and the intensity of the luminosity might be present. All the subplots share the y-axis.

Errors are calculated assuming that the fractions follow a binomial distribution an the bin size is chosen to have the same interval size for the parameter on the x-axis.

In Fig. 3.5, we see that the fraction of sources showing larger evidence for broad reflection decreases with increasing luminosity (see Figure 3.5, left panel). We also notice an anti-correlation with increasing redshift and a clear increase of the fraction of broadened sources with increasing N_H (see Figure 3.5, middle and right panel).

The anti-correlation of the equivalent width (EW) of the Fe Kα line and the luminosity of AGN is well-known characteristic (Iwasawa & Taniguchi 1993; **?**; Page et al. 2003). This anti-correlation, called the Iwasawa-Taniguchi or X-ray Baldwin effect (Baldwin effect hereafter), has been seen both for the narrow core of the Fe Kα, and has also been claimed for the broad component of the line (Nandra et al. 1997b). The anti-correlation between luminosity and fraction of sources selected as broad (Figure 3.5, left panel) could be a consequence of the Baldwin effect for the broadened component of the Fe Kα line.

To study this phenomenon in more detail, we explore the relationship between the reflection fraction R (see Table 3.2) of both the broad and narrow reflection components in the most complex model and the luminosity of the sample sources (see Figure 3.6, left). The mean R values and their intrinsic dispersion were calculated using the HBM, as for the mean values for the whole sample, and exclude from the analysis the 12 sources with $L < 10^{41}$ erg/s to avoid contamination from star forming galaxies.

In Figure 3.6, we see a clear effect that both the narrow and broad Compton reflection fractions decrease significantly as a function of luminosity, from $R \sim 0.5$ at the lowest luminosities to $R \sim 0.1$ at the highest. Thus we confirm the existence of the Baldwin effect for both the broad and narrow components of the line.

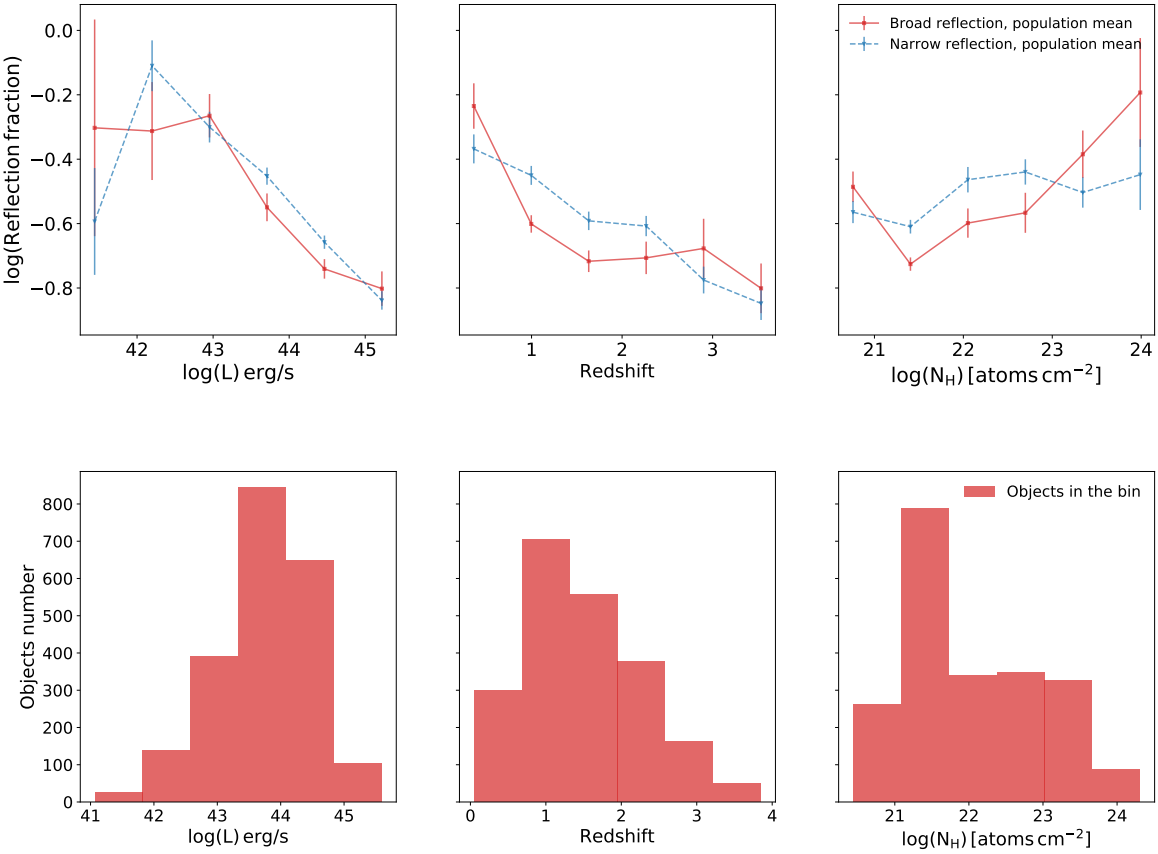

Figure 3.6: Dependence of the reflection fraction for the broad accretion disk reflection component $R_{\rm blur}$ (red) and the narrow reflection $R_{\rm pex}$ from distant material (blue) as a function of the luminosity (*Left panels*) redshift (*Middle panels*) and obscuring column density (*right panels*). Sources with $\log L_X < 41$ erg/s were excluded from the analysis. The upper panels show the mean and intrinsic dispersion of the parent distribution, calculated using the HBM (see text), while the bottom panels show the number of objects in each bin. Both $R_{\rm blur}$ and $R_{\rm pex}$ decrease significantly to higher luminosities, confirming an X-ray Baldwin effect for both the narrow and broad components of the Fe Kα line and associated Compton reflection. Both also show a significant reduction in strength with redshift, and a milder increase with $N_{\rm H}$. These trends might be a by-product of the Baldwin effect. All the subplots share the y-axis.

Fig. 3.6 also shows the dependence of the reflection strengths with redshift and N_H. The same trends shown in Figure 3.5 are seen, with a reduction in the R values with redshift, and a weak increase seen with obscuration. Both of these trends might be wholly or partially a consequence of the Baldwin effect, given the usual correlation between luminosity and redshift seen in flux-limited samples (Fig. 3.2, and the anti-correlation seen between luminosity and obscured fraction (Steffen et al. 2003; Barger et al. 2005; Ricci et al. 2017).

We test this hypothesis by splitting the sample (see Figure 3.7) into low-luminosity ($L < 10^{43.8}$ erg/s, blue in Figure 3.7) and high-luminosity ($L > 10^{43.8}$ erg/s, red in Figure 3.7) sub-samples. We chose this luminosity threshold because it splits the sample almost in half, with 1042 sources in the low-luminosity sample and 1120 in the high-luminosity one. The solid curves show the behaviour of the reflection fraction of the broad disk reflection component while the dashed lines show the R from the narrow torus reflection. We notice that the curves of R as function of redshift and N_H seem to flatten for higher luminosities, thus the trends of R vs. redshift and N_H might be indeed be mirroring the dependency of R with luminosity. Even in Figure 3.7, the stronger trend we can observe is the one with luminosity. In fact, the R values of broad and narrow reflection components at luminosities of $L > 10^{43.8}$ erg/s are consistently lower than the R values at $L < 10^{43.8}$ erg/s, as the X-ray Baldwin effect would predict.

3.4 Discussion

In this work we have used the deepest X-ray fields performed by *Chandra* to place constraints on X-ray Compton reflection in a sample of AGN typical of the overall population, covering a luminosity range $\log L_X = 41 - 45$ erg/s out to $z \sim 4$. We build on the previous work by Baronchelli et al. (2018), adopting the same Bayesian framework BXA to fit the spectra, determine parameters, and compare models. We confirm strong evidence for Compton reflection, and by implication also iron Kα emission, both from distant material, most likely the torus envisaged in orientation-dependent unification schemes, and relativistically broadened reflection modelled as arising from the inner accretion disk.

This relativistic reflection is expected to be ubiquitous in the standard scenario where the SMBH is surrounded by an accretion disk and a hot corona of electrons. As such, perhaps the most important result of our study is to confirm that paradigm in the general population of AGN, which are responsible for the bulk of black hole growth in the Universe, and the majority of the X-ray background radiation (e.g. Aird et al. 2015; Buchner et al. 2015). We observe that the model with maximally spinning Kerr BH is preferred over a model with Schwarzschild BH, reproducing the result from Baronchelli et al. (2018). This confirms that a portion of the reflection comes from very close to the black hole, indeed perhaps from within the $6R_g$ innermost stable circular orbit of a non-rotating black hole. In turn this implies both that a relatively cool accretion disk extends within this radius, and that the X-ray emission comes from the innermost regions, and is compact enough that a substantial proportion of the disk illumination is at these small radii. The result is supported by studies of microlensed quasars at high redshift. For example,

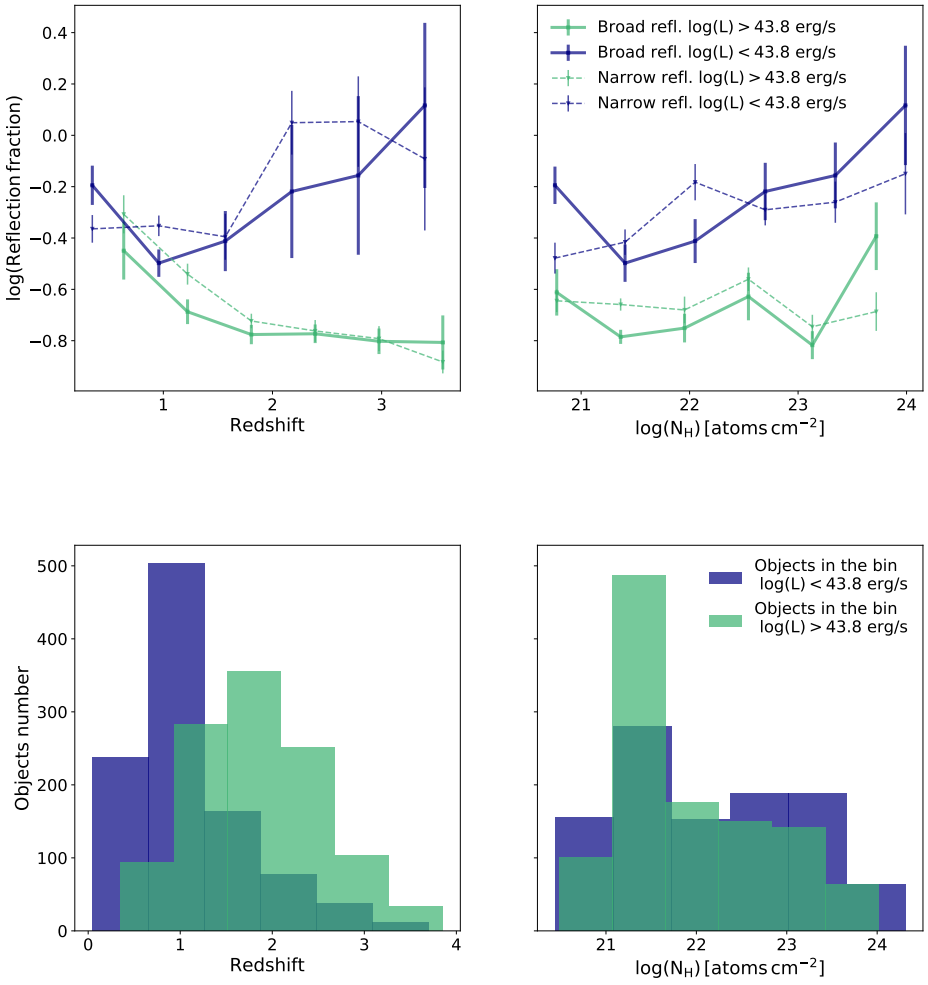

Figure 3.7: R value of broad (solid line) and narrow (dashed line) reflection as function of redshift (*left*) and column density N_H (*right*) in for the subsample with $\log(L_X) > 43.8\,\mathrm{erg/s}$ (red) and $\log(L_X) < 43.8\,\mathrm{erg/s}$ (blue). Both broad and narrow reflection component show a smaller R value at higher luminosity. The odd behavior of the R value in the last bin of the low luminosity sub-sample might be induced by low statistic effects, in fact that bin only comprises 11 objects. All the subplots share the y-axis.

Dai et al. (2019) show evidence of high spin (a > 0.8) in a sample of five lensed quasars at high redshift (z > 1.2) and an ultra-compact X-ray emitting region with size < $10R_g$.

This provides one possible explanation for one of the more puzzling aspects of our analysis, that being the average strength of the relativistic reflection component. We find a value for the average reflection fraction of $R_{\rm blur} \sim 0.3$, contrasting with the $R_{\rm blur} \sim 1$ expected for a flat disk illuminated by a point X-ray source. This relatively weak blurred reflection, at least on average, is in agreement with observations of local AGN (Nandra et al. 2007), although some nearby AGN also show anomalously strong reflection (e.g. MCG-6-30-16 and NGC 1365 Fabian et al. 2002; Risaliti et al. 2013). Both of these facts can be explained by strong relativistic effects and in particular light bending close to the central black hole. This can result in the reflection being either weaker, or stronger than that expected for a flat disc depending on geometrical considerations (Miniutti & Fabian 2004). A reduced reflection strength would also be expected if the X-ray emission is beamed away from the disk (Beloborodov 1999).

Apparently weak reflection may also be explained by ionization of the disk. Some reduction of the line flux is expected for moderate ionization due to resonant trapping, and at very high ionization parameters no line is produced at all once iron becomes fully ionized (Ross & Fabian 1993). In this case the reflection continuum would also become hard to distinguish from the primary continuum.

There may also be geometric effects. The strength of the reflection component is maximised for our assumed geometry of a semi-infinite slab illuminated by a point source. If the real accretion disk-corona geometry is different to this then the reflection is reduced. For example, if the corona of hot electrons were at a height h comparable than the ISCO radius r_{ms}, fewer photons from the corona would intercept the disk. The divergence from the "lamp post" supported is corroborated by studies of microlensed quasars (e.g. Chartas et al. 2012; Dai et al. 2019), and furthermore suggest a very compact primary X-ray source, consistent with this idea. This effect would be further exacerbated if the accretion disk is truncated before the last stable orbit, although in this case the relativistic signatures would be less prominent, contrary to the strong evidence for their presence found in this work.

Our expanded sample compared to that of Baronchelli et al. (2018) has enabled an analysis of the dependence of the strength of reflection from both the torus and the accretion disk with luminosity (see Figure 3.6, left). We confirm an X-ray "Baldwin effect" in which the strength of the reflection component, and by implication the equivalent with of the iron Kα line, reduces with luminosity.

This effect is quite well established for the narrow core of the iron Kα line. The most common interpretation is that of the "receding torus" in which the covering fraction reduces with luminosity (e.g. Simpson 2005). This is in agreement with the observation of a higher fraction of optical type 1 galaxies, and lower prevalence of X-ray absorption, at high luminosities (e.g. Ueda et al. 2003; Hasinger et al. 2005; Buchner et al. 2015).

The possible presence of a Baldwin effect for the broad part of the emission line was suggested by Nandra et al. (1997b). This should not have the same physical origin as the narrow-line X-ray Baldwin effect if the broad line comes from the accretion disk, rather than the torus. The near-absence of reflection in the highest luminosity objects may in part explain why the average reflection fraction in our sample is so low, and hence might be due to the same effects e.g. ge-

ometry, special or general relativistic beaming and/or disk ionization. A priori it is difficult to see where there should be a strong relationship between the disk-corona geometry and the luminosity, disfavouring this interpretation. On the other hand, if photons are beamed away from the disk this would result in an enhanced luminosity for a given object, along with weaker reflection, as observed. At higher luminosities, the disk may also be more highly ionized suppressing the iron Kα line and reflection continuum, as discussed above, and providing a natural explanation for the Baldwin effect.

Looking next to the apparent dependence of R with redshift, this seems most likely to be a consequence of the Baldwin effect, given the very strong luminosity-redshift correlation in our flux-limited samples. We therefore do not speculate further on the possibility of evolution of the disk-corona system over cosmic time, but if this can be confirmed with better data and samples it would certainly be an intriguing phenomenon.

We observe also that the fraction of sources selected as broad and the R value of both disk and torus reflection shows a mild increase with N_H (see Figures 3.5 and 3.6, right panel). At face value this is the opposite of what might be expected, because in standard orientation-dependent unification schemes, absorbed sources should be seen at high inclination, whence the observed reflection signatures are weaker. The observed increase could also partially be a consequence of the Baldwin effect. As discussed above lower luminosity AGN are more likely to be absorbed, and when we restrict the luminosity range in our analysis the effect does indeed seem weaker.

A further effect is the possible degeneracy of the broad iron line with complex absortion in sources with high N_H. If the absorption is in fact more complicate than the simple model assumed here, then for moderately high values around $\log N_H = 23$, mismodelling could introduce apparent curvature in the continuum in the 5-6 keV range, mimicking a broad red wing to the line. Unfortunately, the quality of the spectra in our sample prevents us from constraining the disk inclination parameter for most of the sources. Thus we can neither confirm nor rule out the degeneracy of the obscuration with the inclination of the disk on this basis.

One caveat to the above discussion is that is clearly challenging with spectra of the quality used in this work to decompose the reflection into its broad and narrow components. It can be noted from Figure 3.6 (left), for example, that the luminosity dependence of the R value for the broad disk reflection and for the narrow reflection from the torus have a very similar behavior. Since the two components arise from very different regions around the SMBH, this may indicates that the component are not well decoupled in the model, and that there is considerable co-variance between them.

Properly decoupling and measuring the properties of X-ray reflection in individual AGN at high redshift requires an X-ray telescope with significantly higher throughput then the current generation of instrument. Once launched, *Athena* (Nandra et al. 2013) will provide this capability. Deep field osbervations with the Athena Wide Field Imager (Rau et al. 2013; Meidinger et al. 2016) will yield one or two orders of magnitude more photons per unit exposure than *Chandra*, giving high quality spectra for individual objects like those in our sample. Follow-up observations of selected objects with the *Athena* X-ray Integral Field Unit (X-IFU; Barret et al. 2016) of brighter examples found with the WFI will enable the first high resolution spectra of such objects.

On the other hand, with this project we have confirmed the potential of of X-ray spectroscopy

combined with Bayesian inference to reveal information about the population properties of AGN, even with individual spectra of low signal-to-noise ratio. There are some limitations, in that we have also demonstrated that adding spectra with very low signal-to-noise ratio at some points fails to add further information. Once appropriate signal-to-noise ratio cuts are applied, however, each new objects added to the analysis is able to strengthen our inferences about the accretion processes in SMBHs and the gas structures around them. The recent launch of the instrument *eROSITA* (Predehl et al. 2010) aboard the SRG satellite present a particularly exciting opportunity to take this forward. eROSITA will detect millions of AGN (Merloni et al. 2012; Kolodzig et al. 2013) spread over the full sky and filling out an extremely broad luminosity-redshift plane. This will open up new and exciting possibilities for the application of our methods.

3.5 Summary and Conclusions

We present an analysis of the X-ray spectra of sources taken from the four *Chandra* deep fields CDFS 7Ms, CDFN, AEGIS and COSMOS to determine the Compton reflection and iron Kα line properties of typical AGN outside the nearby Universe. To this purpose, we fit all the spectra individually using BXA, rather than stacking them. We fit four models of increasing complexity, starting from a simple absorbed power-law and adding to this model a narrow reflection component (`pexmon`) and subsequently a further relativistically blurred disk reflection (`kerrconv(pexmon)`) with dimensionless spin parameterfixed at two values, a = 0 and a = 0.998. We perform simulations to determine from which signal-to-noise ratio, S/N, a source adds information to the total Bayesian evidence of the sample, finding that below a S/N of 7 the sources are too faint to add any new information, so we restrict the bulk of our analysis to sources above this limit. The outputs of BXA are the best fit parameters for and the Bayesian evidence of the model, thus we can use the latter to calculate the Bayes factor (BF) for model comparison. Based on the fits to the individual spectra, we adopt a hierarchical Bayesian model (see Appendix 3.6) to determine the sample properties.

Our main findings are:

- When considering the sample as a whole, the Bayesian evidence comparison shows a preference for a model containing both narrow and broad, relativistic Compton reflection. This is in agreement with the result of Baronchelli et al. (2018) using a smaller sample of spectra from the CDFS 4Ms.
- As in Baronchelli et al. (2018), we find that the broad disk reflection model with a maximally spinning BH is preferred over one with spin=0.
- The HBM shows that on average both narrow and broad Compton reflection is relatively weak. We find a mean of $\log(R_{pex}) = -0.53$ with spread $\sigma_{\log(R_{pex})} = 0.2$ for the narrow reflection component and mean of $\log(R_{blur}) = -0.57$ with spread of $\sigma_{\log(R_{blur})} = 0.14$ for the blurred reflection component. This implies a departure from the simple "lamp post" geometry assumed in our reflection models, and in the case of the broad reflection possibly light bending or ionization effects.

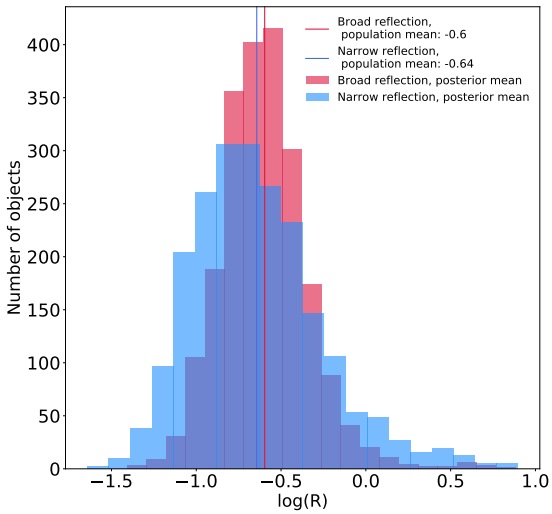

Figure 3.8: Histograms of the mean of the posterior distributions of the R values for narrow and broad reflection components for every object. The vertical lines show the population mean (i.e. the mean of the posterior means) for narrow (red) and broad (blue) reflection.

- We investigate the presence of an X-ray Baldwin effect in our sample, confirming a decrease in the reflection strength for both the distant and blurred components, and by inference both the narrow and broad components of the iron Kα line. The former may be explained by a "receding torus" model, whereas as the latter implies a dependence of the inner disk geometry and or ionization with luminosity.

- We also find anti-correlations of the reflection fraction of the disk and torus with redshift, and a weak positive correlation with N_H. Both may, however, be artifacts of the Baldwin effect.

- With this analysis, we confirm the power of Bayesian statistics to infer important physical characteristics and features of AGN using a sample of relatively low S/N X-ray spectra, a technique which can be applied powerfully to the upcoming eROSITA survey. To measure the properties of X-ray reflection in individual high-redshift AGN we will need instrument with significantly higher effective area, such *Athena*.

3.6 APPENDIX: Hierarchical Bayesian model to infer the intrinsic R distribution

In this work, we have derived posterior distributions for each model parameter over a large sample ($N > 1000$ objects). The parameter of foremost interest in this work is R, which we

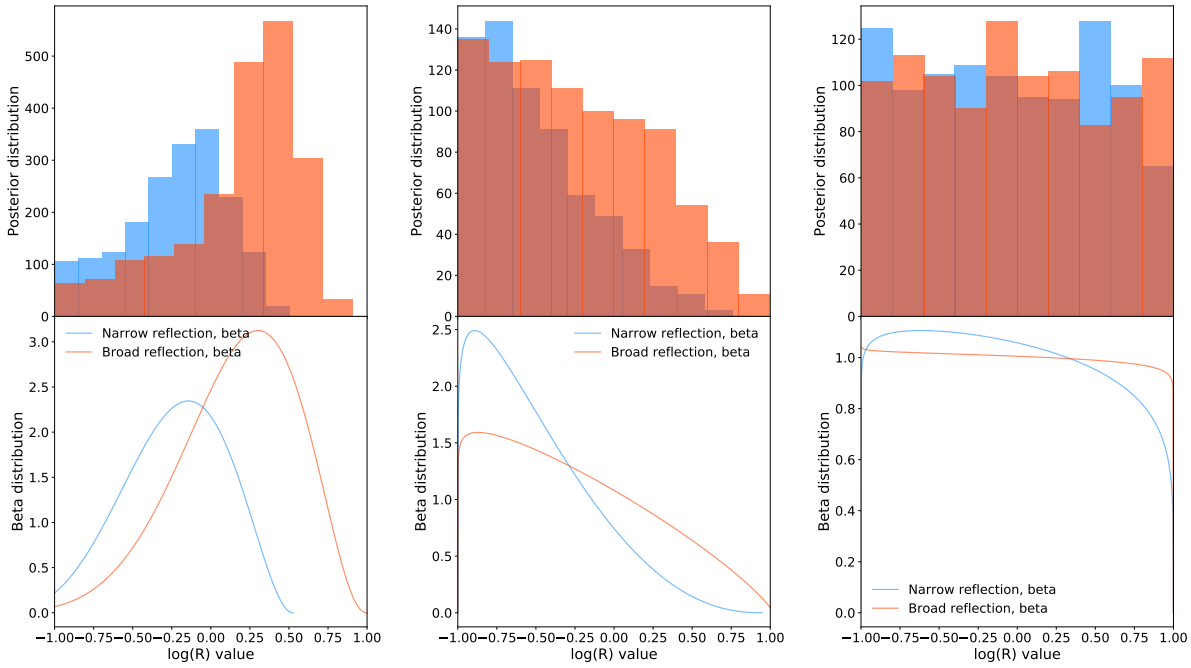

Figure 3.9: Three examples of the shapes of posterior distribution (*top*) of the log R parameter and the fitted beta distribution (*bottom*). The panels show a well constrained example (*left*), an upper limit with the posterior concentrated in the lower half of the prior space (*middle*) and a poorly constrained case (*right*), where the posterior has approximately the shape of the prior distribution (uniform). The three objects whose posterior we show here are source 133, 225 and 345 from the CDFS 7Ms survey.

derived from fitting a model to X-ray spectra of AGN using BXA.

The posterior distributions are diverse and often wide, as illustrated in Figure 3.8. The question is now how to combine these uncertain posterior probability distributions to infer the intrinsic distribution.

Hierarchical Bayesian modelling (HBM) can use the information we have on the single object (the posterior distribution) to infer the features of the parent population from which the objects are drafted (Betancourt & Girolami 2015). To do this, we first assume that the parent distribution of the log(R) parameter is distributed as a Gaussian $\mathrm{N}(\log\mathrm{R}|\mu,\sigma)$ with unknown mean μ and standard deviation σ. Adopting a different parent distribution shape, such as a skewed normal or a Beta distribution did not change the results significantly. For each object, we also have an a priori (before considering the data) unknown parameter R. We have already constrained this, as encoded in the posterior distributions $\mathrm{P}(\log\mathrm{R}|\mathrm{D_i})$ for each object. We can thus write the combined likelihood for a single object as:

$$\int \mathrm{P}(\log\mathrm{R}|\mathrm{D_i})\mathrm{N}(\log\mathrm{R}|\mu,\sigma)\mathrm{d}\log\mathrm{R}. \tag{3.2}$$

Because the same parent distribution should hold for all objects, we multiply their probabilties and find the HBM likelihood:

$$\mathcal{L} = \prod_{\mathrm{i}} \int \mathrm{P}(\log\mathrm{R}|\mathrm{D_i})\mathrm{N}(\log\mathrm{R}|\mu,\sigma)\mathrm{d}\log\mathrm{R}. \tag{3.3}$$

Reusing the derived per-object posterior works here because we have adopted wide priors that are uniform over the integration variable in Eq.3.3 (log R).

After adopting priors on μ (uniform) and σ (log-uniform), this forms a $2 + N$-dimensional Bayesian inference problem. To derive posterior distributions on μ and σ, we use two techniques explained in the following sections.

3.6.1 Hierarchical Bayesian Model inference with Stan

One way to solve Eq.3.3 is to fit for all $N + 2$ parameters simultaneously. This requires advanced Hamiltonian Monte Carlo techniques which rely on likelihood derivatives to navigate the search space. One issue is that we do not want to refit the spectra in this process. Therefore, to still allow each per-object R to vary according to its spectral constraints, we adopt an analytic approximation to its posterior.

We first fit the posterior distributions of every object with a beta distribution. The free parameters are the shape parameters α and β and the location and width of the distributions. Since the parameter range from $-2 < \log(\mathrm{R}) < -1$ does not have much physical sense and reflection fractions below 0.1 are virtually indistinguishable, we constrain the fit distributions to lie between -1 and 1. The posterior shapes differ depending on whether the parameter is well constrained, not constrained or an upper/lower limit (see Figure 3.9, *left* panels). Thus, we choose the beta distribution because it is flexible enough to fit reliably distributions with different shapes. The bottom panels of Figure 3.9 show our best-fit beta approximations.

Next, we implement with the Hamiltonian Monte Carlo framework STAN[2] (Stan Development Team 2014) a model that reads the parameters of all Beta distributions (vectors of α, β, location and scale). The model (Stan code in Listing 3.1) has free R parameters, which both follow these distributions and a parent normal distribution. The MCMC algorithm then simultaneously determines the posterior of the parameters (mean and sigma) of the normal parent distribution and that of the R values.

For the sample with S/N>7 we obtain a mean of $\log(R_{pex}) = -0.53$ with spread $\sigma_{\log(R_{pex})} = 0.2$ for the narrow reflection component and mean of $\log(R_{blur}) = -0.57$ with spread of $\sigma_{\log(R_{blur})} = 0.14$ for the blurred reflection component (see Figure 4.7). For comparison, if we average the means of every single posterior distribution of the R values we obtain a mean of $\log(R_{pex}) = -0.64$ with spread of $\sigma_{\log(R_{pex})} = 0.38$ for the narrow reflection component and mean of $\log(R_{blur}) = -0.6$ with spread of $\sigma_{\log(R_{blur})} = 0.26$ for the blurred reflection component (see Figure 3.8).

This method takes into account the large parameter uncertainties and upper limits. Since many of the posterior distributions for the R value have the shape of an upper limit (see Figure 3.9, *middle*), the mean of the population we obtain with a HBM is much smaller than the mean we would obtain by simply averaging the mean of every posterior distribution (see Figure 3.8, for the simple mean and Figure 4.7 for the mean and sigma obtained with a HBM method).

The values presented in Figures 3.5 and 3.6 were calculated by applying the HBM to the subsamples of objects in 6 bins of luminosity, column density and redshift.

Listing 3.1: Stan definition of a HBM where the input data has the shape of a beta distribution with parameters a, b, loc and scale and the model to be fit is a normal with parameters mu and sigma.

```
data {
    int<lower=0> N;
    vector[N] a;
    vector[N] b;
    vector[N] loc;
    vector[N] scale;
}
parameters {
    real<lower=-1, upper=1> mu;
    real<lower=-2, upper=2> logsigma;
    vector<lower=0, upper=1>[N] u;
}
transformed parameters {
    vector[N] x;
    real<lower=0> sigma;
    x = u .* scale + loc;
    sigma = pow(10, logsigma);
}
```

[2]See https://pystan.readthedocs.io/en/latest/.

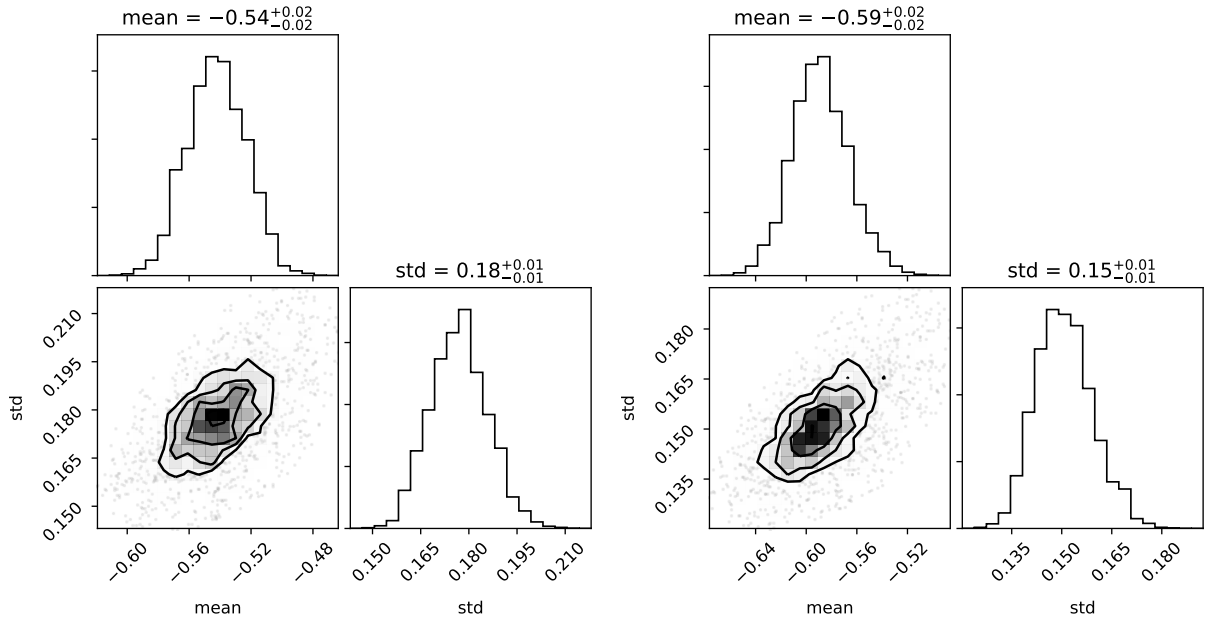

Figure 3.10: Corner plots of the mean and sigma of the population of log(R) values for narrow (*top*) and broad (*bottom*) reflection component.

```
model {
    u ~ beta(a, b);
    x ~ normal(mu, sigma);
}
```

3.6.2 Numerical Hierarchical Bayesian Model inference

Another approach is to use importance sampling to numerically simplify the problem to 2 parameters. In practice, we already have posterior samples $R_{i,j}$ for each object i that approximate the (sometimes complex) posterior distributions. Therefore, we can write 3.3, dropping constant factors, with an importance sampling estimate:

$$\mathcal{L}(\mu, \sigma) \approx \prod_i \sum_j N(\log R_{i,j} | \mu, \sigma). \tag{3.4}$$

When using too few posterior samples, this approach can induce numerical noise into the population posterior. Care has to be taken when this approach is used for multi-dimensional integrations (see also Buchner et al. 2015). Akin to cross-validation, this could be further improved by using sub-samples of the posterior samples in Eq.3.4, and averaging the estimators. However, by varying the number of posterior samples used from hundreds to thousands, we verified that for our problem this Monte Carlo one-dimensional integration is stable.

The two-dimensional log-likelihood defined in Eq.3.4 is Monte Carlo sampled using `UltraNest`[3],

[3]See `https://johannesbuchner.github.io/UltraNest/index.html`

a python nested sampling package developed in Buchner (2019). Figure 3.10 shows the posterior of the mean and sigma of the normal distribution. For the total sample with S/N>7 we obtain a mean of $\log(R_{pex}) = -0.54$ with spread $\sigma_{\log(R_{pex})} = 0.18$ for the narrow reflection component and mean of $\log(R_{blur}) = -0.59$ with spread of $\sigma_{\log(R_{blur})} = 0.14$ for the blurred reflection component.

Finally, we briefly compare the two methods. On the one hand, the method of 3.6.2 makes no assumptions about the shape of the distribution. On the other hand, the method of Section 3.6.1 using Beta distributions avoids numerical sampling issues. In practice, the two methods of Section 3.6.1 and 3.6.2 show consistent results, which gives confidence in the method. The presented tools for Hierarchical Bayesian modeling are thus powerful and robust for inferring the intrinsic distribution given a large number of uncertain measurements, including upper limits.

Chapter 4

Relativistic reflection in XMM observations of MCG–6-30-15

In the previous two chapters, we studied the characteristics of the relativistic reflection in large samples of *Chandra* AGN spectra. Our samples comprised two hundred (see Chapter 2) and later thousands (see Chapter 3) of objects, however, the vast majority of their spectra was low signal-to-noise. In this chapter, we test the method used in the previous two chapters on a single object with eight high signal-to-noise *XMM* observation, namely the source MCG–6-30-15. This will allow us to test more complex models with a higher number of free parameters that previously would have overfitted the noisier *Chandra* spectra. We aim to find a model to explain and fit consistently all eight observations. A recurrent interpretation for the broadening of the Fe Kα line links its origin to the proximity of the central SMBH to the region where the line is emitted. In this scenario relativistic effects (e.g. gravitational redshift and relativistic Doppler effect) broaden and skew the line profile, smearing it to low energies (Fabian et al. 1995). However, alternative theories suggest that a similar spectral shape could be produced by absorption of the continuum or by ionized out-flowing winds (Miller et al. 2007, 2008). Although considering the nature of AGN, it is natural to expect both relativistic effects due to the proximity of the SMBH and ionized material close to the central engine, due to the strong emitted radiation. Both these phenomena would contribute to the broadening of the Fe Kα line, in fact, simulations by Sim et al. (2008) show that the Fe line can develop a skewed red-wing as result of Compton scattering in an out-flowing wind. In this chapter, we use BXA to test the coexistence of these two broadening mechanisms in the X-ray spectrum of MCG-6-30-15. In particular, our aim is to find a model to explain the complex *XMM* spectra of this source and the spectra variability in a self-consistent way. The powerful hierarchical Bayesian methods developed and applied in the previous chapters can then help us to set strong constraints on parameters like spin and inclination angle.

4.1 Introduction

When the primary power-law X-ray emission from AGN illuminates the accretion disc and the molecular obscuring torus, the photons get reflected and reprocessed creating reflection features in the spectrum, for example, the iron (Fe) Kα line at 6.4 keV in the rest frame.

The Fe Kα line is intrinsically narrow, however, observations with ASCA, *XMM-Newton*, *Suzaku* and *Chandra* indicate that the line can have a broad red wing extending up to energies of 3 keV (e.g., Nandra et al. 1997a; Wilms et al. 2001; Fabian et al. 2002; Vaughan & Fabian 2004; Miniutti et al. 2007; Nandra et al. 2007).

The Seyfert I galaxy MCG–6-30-15 at z = 0.00775 was the first unobscured AGN to show line emission (Nandra et al. 1989; Matsuoka et al. 1990). It was also one of the first sources to show evidence in ASCA observations for broad wing emission in the 6.4 keV Fe Kα feature (Tanaka et al. 1995; Miller et al. 2008). The physical origin of the broadened Fe Kα line was first thought to be of relativistic nature (Fabian et al. 1995).

However, the bold theory to explain the Fe Kα skewing with relativistic effects arising a few gravitational radii from the central BH is still debated and should be probed against other models. Due to the quality of the 1994 *Advanced Satellite for Cosmology and Astrophysics* (*ASCA*) (and subsequently *XMM*) observations of MCG–6-30-15, the Fe Kα line in the spectra of this galaxy has become the test case to verify and reject different hypotheses.

Fabian et al. (1995) addressed different alternative models to explain the line profile of the iron line, including the contribution lines from mild relativistic outflow, the effect of absorption edges on the spectrum, and broadening of the line via Comptonization. All these alternatives were found as non-viable in Fabian et al. (1995), however, the broadening via Comptonization possibility was later revisited by Misra & Kembhavi (1998) and Misra & Sutaria (1999).

They hypothesize a Comptonizing cloud with optical depth $\tau \approx 4$. To explain the Fe line profile, the cloud has to be simultaneously cold ($kT < 0.5keV$), to predominantly down-scatter the line photons instead of up-scatter, and fully ionized, since no iron absorption edges are detected in the continuum. The cloud is kept ionized yet cold by assuming that the source is a powerful optical/UV emitter. There are strong arguments against this model, in fact, since also the power-law component would have to pass through the Comptonizing cloud, thus one should observe a break in the continuum spectrum at $E_{br} \approx m_e c^2/\tau^2 \approx 30$ keV (Reynolds 1999) but such break is not observed in either *BeppoSAX* (Guainazzi et al. 1999) nor in *Rossi X-ray Timing Explorer* (*RTXE*) spectra (Lee et al. 1999a). Moreover, the continuum variability (of the scale of ∼100s) and the ionization argument imply that the size of the cloud should e of the order of $R < 10^{12}\ cm^2$ and the ionization parameter close to the surface of the cloud should be so high that all abundant metals, including iron, must be close to fully ionized (Fabian et al. 1995; Reynolds & Wilms 2000). In the case of MCG–6-30-15, the constraints on the cloud size are so tight that the theorized optical/UV component required to keep the cloud cold would violate the blackbody limit (Reynolds & Wilms 2000). Furthermore, it was proved in Ruszkowski et al. (2000) that Componization would fit poorly MCG–6-30-15 spectrum. Therefore, I do not explore further the Comptonization model in this work.

In another alternative model, Skibo (1997) postulates that spallation due to energetic protons would transform Fe atoms on the surface of the disk into Chromium and other lower Z atoms.

The fluorescence emission of these new atoms would then be enhanced by the spallation process itself. With limited spectral resolution, these fluorescent lines would be then blended and appear like a broadened and skewed Fe Kα line. However, these models present both theoretical and observational issues. On the theoretical side, the protons would have to be produced with extremely high efficiency ($\eta \approx 0.1$), while on the observational side the Fe line in MCG–6-30-15 was observed with spectral resolutions of 150 eV in *ASCA* SIS (Tanaka et al. 1995) and that resolution would be enough to determine whether the feature would be produced due to several well-spaced singular lines distributed over 2 keV Reynolds (2001). For this reason, I consider this theory as non-viable and will not explore it further.

The most recent and debated alternative theory to explain the broadening of the line profile was given by Lee et al. (2001) and Kinkhabwala et al. (2003). Since the Fe line signature is often observed in spectra that show signs of absorption by photoionized plasma (the so-called "warm absorbers"), the authors showed that the 3–6 keV spectral shape could also be explained by a highly absorbed continuum. In fact, MCG–6-30-15 presents strong absorption lines, indicating absorption by clouds of gas with very wide ranges of ionization. Moreover, the detection of the emission lines Fe XXV and Fe XXVI at 6.7 and 7.0 keV (Young et al. 2005; Miniutti et al. 2007) together with Si XIV and Si XVI at 2.0 and 2.6 keV (Young et al. 2005) suggest a highly ionized outflow zone.

This hypothesis was already addressed by Sako et al. (2003), Young et al. (2005) and Reynolds & Fabian (2008) and was found not completely satisfactory.

Later (Miller et al. 2007, 2008) re-proposed the idea.

Despite MCG–6-30-15 is one of the most studied sources in the history of X-ray astronomy, many open questions still surround it. For example, not only the origin of the broad Fe line is not completely understood but also the nature of its variability. MCG–6-30-15 exhibits large variability on a variety of time scales and is one of the brightest and most variable Seyfert I ever observed (Nowak & Chiang 2000).

Lee et al. (1999b) and Chiang et al. (2000) of *RXTE* data sets for MCG–6-30-15 found that the photon index displays flux-correlated changes, in the sense that the brighter the source is the softer is its spectrum. More surprisingly, the authors find that the iron line flux was found to be constant over timescales of $\sim 50 - 500$ ks. The same result was found in Iwasawa et al. (1996) and Vaughan & Fabian (2004), which found that the red wing component is constant in amplitude despite the primary continuum being variable. In the case where the red wing emission is produced when the continuum is reflected by the accretion disk, one would expect its amplitude to vary analogously to the amplitude of the continuum. However, the reflection-dominated component and the power-law continuum appear disconnected, at least partially (Miniutti 2006). Indeed, this trend can be observed in many spectra of Seyfert 1 galaxies, where the spectrum can be described as the combination of a highly variable power-law continuum together with a much more constant disc reflection (Fabian et al. 2004, 2005; McHardy et al. 2005; Ponti et al. 2006).

As the extensive broadening of the Fe line in the reflection-dominated component of MCG–6-30-15 indicates, the reflection component is emitted at a few gravitational radii. However, this is also the region where most of the accretion power is dissipated and therefore the power-law component must be emitted in the corona in the same region close to the BH. Thus, the origin of the lack of response of the reflection component to the power-law variation cannot be attributed

to light-travel-time, since the two emissions arise in the same disc region (Miniutti 2006).

The constancy of the Fe line in MCG–6-30-15 seems to indicate that the central SMBH must have a very high mass (more than $10^8 M_\odot$). However, such a large mass contrasts with the constraints set from both the X-ray variability and the mass from the galactic bulge. In fact, the best estimate of the BH mass in MCG–6-30-15 is $\sim 1 \times 10^6 M_\odot$ (Uttley et al. 2002). That value is based on an estimated bulge mass of $\sim 4 \times 10^9 M_\odot$ (Reynolds 2000) and on the correlation between BH mass and galactic bulge mass presented by Wandel et al. (1999). To reproduce the constancy of the Fe line flux, the amount of line emission must be regulated by some feedback mechanism.

This lack of variability can be explained with a light-bending model, where the variation in amplitude is not due to an intrinsic variation of the source but to the distortion of geodesics of photons near the SMBH (Miniutti et al. 2003; Miniutti 2006). In this scenario, the parameters that drive the variability of the power-law continuum and of the primary photons illuminating the disc is the height (h) of the primary source above the accretion disc. Thus, if h is small and the source is closer to the BH a large fraction of primary power-law photons are bent toward the disc due to the strong gravitational field and the observed power-law will result weaker. If, however, the source is farther away from the BH, fewer photons will deviate towards the disc and the observed power-law will result stronger. With this setup, the broad Fe line is not expected anymore to respond to the observed power-law variability (Miniutti & Fabian 2004; Miniutti 2006). Another way to produce a constant red wing would occur if the reflection were emitted far away from the primary source, so that light travel time smooths any variation in the luminosity.

However, Miller et al. (2008) sees the lack of variability of the red wing as further proof that the broadening of the Fe line is just apparent and is due to the etching away of the continuum by ionized absorption.

The aim of this work is to probe the origin of the broad Fe Kα line in eight observations of MCG–6-30-15 taken with *XMM-Newton*. Thanks to BXA, I can try to find a model that would explain the complex spectra of MCG-6-30-15 consistently with variability. Moreover, I use Bayesian inference to verify the coexistence of relativistic broadening effects in the reflection spectrum as well as ionized absorption.

The chapter is structured as follow: inn Section 4.2 I present a small overview of the most relevant reflection models implemented for XSPEC. In 4.3, I present the sample selection criteria, the spectra extraction and fitting routine. The results are presented in Section 4.4 and discussed in Section 4.5. Finally, I summarise the work in Section 4.6.

4.2 Reflection models

There are many available models to describe the X-ray reflection component in X-ray spectra. On XSPEC alone there are at least twenty reflection models implemented.

Some of the most notable examples are `pexrav` (Magdziarz & Zdziarski 1995) and its derivation `pexmon` (Nandra et al. 2007), `reflionx` (Ross & Fabian 2005) and `xillver` (García & Kallman 2010). The models `pexrav` and `pexmon` represent the reflection from a

neutral medium of an exponentially cut off power-law spectrum (Magdziarz & Zdziarski 1995), the output spectrum is this reflection component added to the original cut off power-law, however, there is the option to only return the reflection component by setting the reflection fraction as less than 0. The additional feature in `pexmon` is that it combines `pexrav` with self-consistently generated Fe Kα, Fe Kβ, Fe Kα Compton shoulder and Ni Kα. The lines strengths are based on simulation from George & Fabian (1991) (see also Fig. 1.5). In these two models, it is assumed that the incident radiation is weak enough to leave the gas of the disc neutral but strong enough to produce reflection features (Guilbert & Rees 1988). This view, however, offers a limited representation of the physical processes behind atomic processes leading to absorption, emission, and excitation.

This issue was addressed in later models, for example `reflionx` and `xillver`. In the model `reflionx`, the authors take into account the case in which the X-ray radiation is strong enough to ionize the gas in the disc, with the assumption that the illuminated atmosphere has constant density. Moreover, in addition to fully ionized atomic species also partially ionized atoms are included in the calculation (for example C III-VI, N III-VII, O III-VIII, Ne III-X, Mg III-XII, Si IV-XIV, S IV-XVI, and Fe VI-XXVI). In `xlliver` the reflected spectrum is calculated by simultaneously solving the equations of radiative transfer, energy balance, and ionization equilibrium in a Compton-thick, plane-parallel medium. The model `xlliver` makes use of the photoionization code XSTAR to calculate the ionization structure in the disc atmosphere, therefore it is based on the most complete, accurate, and updated database of atomic emission and absorption X-ray lines for the most astronomically relevant ions.

These models are decoupled from the relativistic smearing associated with the proximity of the SMBH. However, the smearing associated with strong gravity might be added as broadening kernel. Some example of these relativistic kernels are the additive models `laor` (Laor 1991), `diskline` (Fabian et al. 1989) and `relline` (Dauser et al. 2010, 2013) later extended to the convolution models `kdblur/rdblur` [see Chapter 2 and `kerrconv` (Brenneman & Reynolds 2006) (see Chapter 3). The convolution models can be used to smear the non-relativistic reflection component, without limiting the blurring to only the Fe Kα line.

García et al. (2014) combines the angle-dependent reflection model `xlliver` with the convolutional relativistic blurring code `relline` to create the most advanced relativistic reflection model currently available. At first approximation, the model convolves `xillver` and `relline`, however, there are more subtle differences, as described in García et al. (2013), which make the model more than a simple convolution. In short, `relxill` correctly takes into account The emission angle of the photons coming from the disk, as due to GR and light-bending they will be observed at a different inclination, which is changing throughout the disk.

In this chapter, we compare mainly the models `reflionx`, `kerrconv`, and `relxill`, to explore different scenarios where the reflection component is blurred by ionized absorption or by relativistic broadening as well as a scenario where both effects are contributing to the smearing of the reflection component. We add to every model also a `pexmon` component to represent the narrow reflection component from the cold molecular torus.

Table 4.1: Description of the eight *XMM* spectra studied in this work. The source (src) and background (bkg) counts were obtained in the 2.5 – 10 keV observer frame energy range with the SHERPA tool `calc_data_sum()`. The observations are sorted in order of increasing exposure time. The signal to noise ratio (SNR) is calculated as SNR = src/ $\sqrt{(\text{src} + \text{bkg})}$.

Obs. Id[a]	Start date[b]	Exp. time[c]	Source counts	Background counts	SNR
0111570101	11/07/2000	46453	64427	640	252.6
0693781401	02/02/2013	48918	35443	250	187.6
0111570201	11/07/2000	66197	109346	508	329.9
0029740101	01/08/2001	89432	15831	502	397.4
0029740701	03/08/2001	129367	285166	1072	533.0
0029740801	05/08/2001	130487	286274	782	534.3
0693781201	29/01/2013	134213	375276	1001	611.8
0693781301	31/01/2013	134214	250726	703	500.0

[a] *XMM-Newton* observation Id.
[b] DD/MM/YYYY.
[c] Exposure time in seconds.

4.3 Sample and method

4.3.1 Data and spectra extraction

We study eight *XMM* archived PN spectra of MCG–6-30-15 observed in the time range from July 2000 to January 2013 (see Table 4.1). We clean the data and extract the spectra using XMMSAS as explained on the webpage [1] and in Nandra et al. (2007). To sum up the procedure, we first initialize XMMSAS with the tasks `cifbuild`, which produces a file linking the working directory to the current calibration files (CCF), and `odfingest`, which takes the observational information from all the observation data files (ODF) and produces a detailed summary file. Once the initialization of XMMSAS is complete, we extract light curves for source and background [2] and we filter the EPIC event list for periods of high flaring activity [3]. Finally, we select source and background regions and we extract the spectrum for source and background with `evselect` and ancillary files with the tasks `rmfgen` and `arfgen`.

We follow the method explained in Nandra et al. (2007) to select the ratio to filter the light curves and to select the background region.

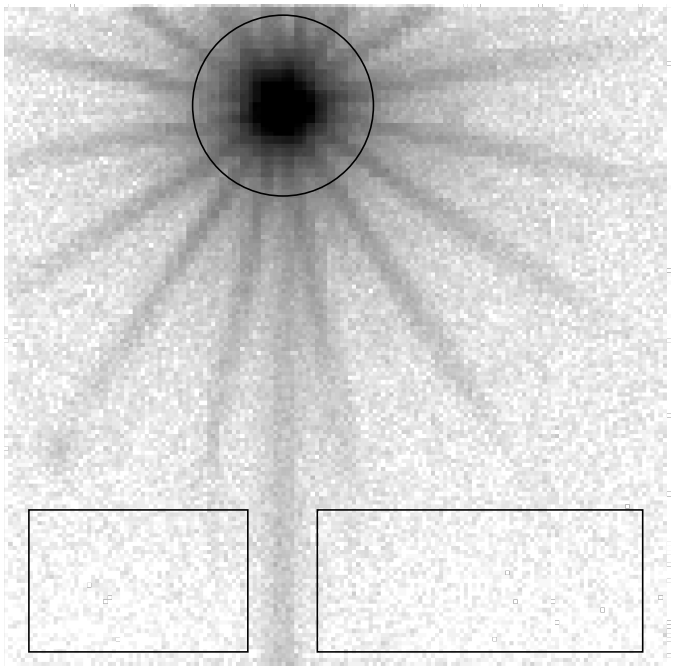

Figure 4.1: Example of source and background regions for the observation 0693781301 of MCG–6-30-15.

Table 4.2: List of the models used in this work with number of free parameters.

Model [a] Absorption comp.	Free parameters[b]
`zwabs`	N_H
`cwa18`	N_H, $\log(\xi)$
`swind1`	N_H, $\log(\xi)$, σ
`zxipcf`	N_H, $\log(\xi)$, σ (redshift), covering fract.
Model [a] Reflection comp.	**Free parameters[b]**
`zpowerlw+pexmon`	Γ, A_{pow}, A_{pex}
`zpowerlw+pexmon+kerrconv(pexmon)`	Γ, A_{pow}, A_{pex}, A_{kerr}, Incl
`zpowerlw+pexmon+reflionx`	Γ, A_{pow}, A_{pex}, A_{ref}, $\log(\xi)$
`pexmon+relxill`	Γ, A_{pex}, A_{ref}, $\log(\xi)$, spin, Incl,Index1

[a] Model components.
[b] Logarithm of the Bayes evidence of the full sample normalized to the largest evidence.

Table 4.3: Prior distribution of the free parameters in the absorption models `zwabs`, `cwa18`, `swind1`, and `zxipcf`. We report below only the parameters that are allowed to vary, their prior distribution is a uniform interval with limits [Min., Max.]. The redshift is set to 0.008 except in the model `zxipcf` where it is allowed to vary to simulate in-/outflows.

Comp.[a]	Name[b]	Min	Max
zwabs	$\log(N_H^c)$	20	26
cwa18	$\log(N_H)$	20	26
	$\log(\xi)$	-4	4
swind1	$\log(N_H)$	20	26
	$\log(\xi)$	-3	4
	σ	0	0.5
zxipcf	$\log(N_H)$	20	26
	$\log(\xi)$	-4	4
	redshift	-0.9	0.9
	covering fraction.	0	1

[a]Model component.
[b]Parameter name.
[c]The comuln density N_H is in units of atoms cm^{-2}.

4.3.2 Models and model fitting

As the first step in this project, I seek to find the "perfect" model that will fit the eight *XMM* observations of MG-6-30-15 consistently. The ideal model would find the same values of parameters like the SMBH spin and the accretion disk inclination for all the different observations, we expect these quantities to be constant over time, or at least to be constant over a lapse of time so limited as the one in which the observations were taken. Since MCG-6-30-15 has an extremely complex soft excess below 2keV and we are interested in higher energies to study the Fe Kα line in detail, we only fit the energy range 2.5 – 10 keV (observed frame) to avoid biasing our spectral fit with complexities arising from the softer X-ray spectrum.

We study four different models for absorption and four different types of reflection. We compare the classical model for photoelectric absorption `zwabs` (Morrison & McCammon 1983) with two models describing ionized absorption. The first ionized absorption model, `cwa18`, was created by Nandra et al. (2007) using version 21kn of XSTAR and is a fine grid covering a wide range of parameter space. The parameters of this model are redshift, ionization parameter ξ, and column density N_H. The third absorption model, `swind1`, was built by Gierliński & Done (2004) and updated in Gierliński & Done (2006). It is engineered to model partially ionized absorbing material with a large velocity dispersion. It approximates this by convolving Gaussian smearing with photoionization absorption grids modeled with XSTAR 5kn. Lastly, we test the

[1]See `https://www.cosmos.esa.int/web/xmm-newton/sas-threads`
[2]as explained in `https://www.cosmos.esa.int/web/xmm-newton/sas-thread-timing`
[3]see `https://www.cosmos.esa.int/web/xmm-newton/sas-thread-epic-filterbackground`

Table 4.4: Prior distribution for the continuum and reflection model components zpowerlw, relxill, reflionx, and kerrconv(pexmon) (here abbreviated as blur). In the model component kerrconv, we fix the spin parameter to the values 0 or 0.998 depending on the case we want to analyze. The parameters not reported here are fixed to the default value. The strength of the blurred reflection component component R_{blur} is measured relative to the power law and is defined as the ratio of the normalization of the blurred pexmon component (A_{blur}) to that of the power-law (A_{pow}). The parameters that have units are [N_H] = atoms cm^2, [foldE] = keV, [Incl] = deg, r_{br} in gravitational radii and R_{in} and R_{out} in units of the radius of marginal stability.

Comp.[a]	Name[b]	Min	Max	Fix val.
zpowerlw	PhoIndex	1.1	2.5	-
	log A_{pow}	-10	1	-
pexmon	PhoIndex	1.1	2.5	-
	rel_refl	-	-	-1
	Incl	-	-	60
	log(R_{pex})	-2	1	log $\frac{A_{pex}}{A_{pow}}$
kerrconv(pexmon)	cos(Incl)	0	1	-
	Spin	-	-	0/0.998
	PhoIndex	1.1	2.5	-
	rel_refl	-	-	-1
	Incl	-	-	link to pexmon
	log(R_{blur})	-2	1	log $\frac{A_{blur}}{A_{pow}}$
relxill	PhoIndex	1.1	2.5	-
	Index1	-10	10	-
	Index2	-	-	3
	R_{br}	-	-	15
	rel_refl	0	10	-
	Incl	0	80	-
	log(R_{blur})	-2	1	-
	spin	0	0.998	-
reflionx	PhoIndex	1.1	2.5	-
	log(ξ)	0	3	-
	log(R_{blur})	-2	1	log $\frac{A_{blur}}{A_{pow}}$

[a]Model component.
[b]Parameter name.

ionized partial covering model `zxipcf` (Reeves et al. 2008) leaving the redshift as free parameter to simulate a ionized wind. High resolution *XMM* observations of MCG–6-30-15 revealed that often several layers of ionizing regions are required to model the spectrum (Nandra et al. 2007), thus, we also test a model in which we multiply two independent `cwa18` components to model a two-zone ionized absorber.

We want to study three different scenarios to model the reflection component (see Table 4.2). In the first scenario, we assume the reflection component and the Fe Kα line are blurred by relativistic effects due to the proximity of the SMBH. We use the same model as the one used in Chapter 3 of this thesis, which is `kerrconv` (Brenneman & Reynolds 2006) with the same parameter constraints. For the second scenario, we represent the reflection from an ionized accretion disc with the model `reflionx` (Ross & Fabian 2005). In this model, the incoming hard X-ray photons photoionize the surface of the accretion disk to the extent that the main X-ray absorbers are significantly ionized. MCG-6-30-15 is a case of study for complex absorption and reflection features. For this reason, in contrast to Chapters 2 and 3, we do not fit the data with a simple absorbed power-law (`zwabs*zpowerlw`) as we know already that a power-law can not model adequately the complex spectrum of MCG-6-30-15.

Finally, we add two narrow absorption lines modeled with `zgauss` at 6.7 and 6.97 keV. We fix the sigma of these components at 0.01 keV, since this was the value found in Nandra et al. (2007) and we allow the norm of the components to vary between 10^{-10} and 10.

4.4 Results

We fit with BXA eight *XMM* spectra of MCG-6-30-15 singularly to calculate the Bayesian evidence Z for different models and their best-fit parameters with posterior distributions. Using the BF method (see Chapters 2 and 3) we want to find the model components fitting the different observations of MCG-6-30-15 consistently.

We first fit the reflection models used in Chapter 3, `powerlaw + pexmon` and `powerlaw + pexmon + kerrconv(pexmon)`, with photoelectric absorption `wabs`. We do not leave the spin as a free parameter but we fix it to either 0 or 0.998 (see Chapter 3). We find that a `pexmon` alone is not enough to fit adequately the complex reflection component shown in the spectra (see Table 4.5). Thus, from now on we will exclude the simplest model `zpowerlw + pexmon` from the analysis.

We want to determine which absorption model better fits the data, thus we fit the eight spectra with the same reflection component `powerlaw + pexmon + kerrconv(pexmon)` (maximum spin) and different absorption models (see Table 4.2). We also add to the analysis a fit with a double `cwa18` to model different layers of ionized absorbers and a model in which we fix the inclination angle in the `kerrconv(pexmon)` component and we let the spin-free to vary (see Table 4.6). We find that the BF method prefers the ionized absorption models `cwa18`, `swind1`, and `zxipcf` over the photoelectric absorption `zwabs` (see Table 4.6). Globally, `cwa18` is preferred over both `swind1` and `zxipcf`, however, the difference in evidence Z on a source by source basis is small enough to make them virtually indistinguishable. For this reason and considering that the model `cwa18` is more physically justified than `swind1`, we exclude

Table 4.5: Comparison of the total sample Bayesian evidence for the models `zwabs * (zpowerlw + pexmon)` and `zwabs * (zpowerlw + pexmon + blur(pexmon))`. We fit the models in the observed frame energy range 2.5 – 10 keV.

Model [a]	log10(Z)[b]
`zwabs*(zpowerlw+pexmon)`	-208.8
`zwabs*(zpowerlw+pexmon+kerrconv(spin=1)(pexmon))`	-3.3
`zwabs*(zpowerlw+pexmon+kerrconv(spin=0)(pexmon))`	0

[a] Model components.
[b] Logarithm of the Bayes evidence of the full sample normalized to the largest evidence.

the latter from the rest of the analysis and we proceed to include only `cwa18` in the next model fits.

In most of the spectra, two absorption lines at 6.7 keV and 6.97 keV are observable (Nandra et al. 2007). We decide to test the evidence with and without these features. The model we use for this purpose is `zgauss` (I will denote them as `G` in the following tables, for the sake of brevity) subtracted twice from the continuum plus reflection model. We fix the energy of the two absorption lines at 6.7 and 6.97 keV and we also fix the energy width at 0.01 keV as found by Nandra et al. (2007). The only parameter we allow to vary in those components in the norm. From Table 4.7 one can see that the models with the two absorption lines are in general preferred over the models without.

As a next step, we want to take into account different models for the reflection component to compare three different scenarios to explain the blurring of the Fe Kα line: 1) the broadening reflection component arises due to relativistic effects due to the proximity of the SMBH (`kerrconv(pexmon)`), 2) the Fe Kα line appears broadened because primary X-ray continuum is reflected by ionized matter and complex absorption (`reflionx`), 3) there is a contribution of both effects (`relxill`). For all three scenarios, we include a `pexmon` component in the model to fit the narrow reflection from the torus. We model the primary continuum as a `zpowerlaw` in the first and second model, but the third does not need such a component, since we allow the reflection fraction parameter of `relxill` to be positive and that already models the primary continuum (see Table 4.8).

Before comparing these three different reflection models, we need to choose a parameter configuration for `relxill` to make the model as physical as possible but keeping the complexity given by extra free parameters to a minimum. The minimal number of the free parameter we can have is 7 by allowing the variation of the photon index Γ, after linking it to the photon index of the `pexmon`, the norm, the reflection fraction, R, the inclination angle, the spin, a, and the logarithmic ionization fraction, log(ξ) (see Table 4.2). We chose a semi-physical parameter combination where the breaking angle R_{br} is fixed to 15, the Index 1 is free to vary and the Index 2 is frozen to 3.

The source count rate in the 2.5–10 keV and 4–7 keV is shown in Figure 4.3, the best fit model is shown in Figure 4.2 and the best fit parameters are reported in Figure 2.4. The values in Figure 2.4 are mean of the posterior distribution and the 68% confidence interval for the plotted

Table 4.6: Source by source comparison of the total sample Bayesian evidence for the models with absorption components `cwa18 x 2`, `zwabs`, `swind1`, `zxipcf`, and `cwa18` and continuum and reflection `(zpowerlw + pexmon + blur(spin 0)(pexmon))`. We fit the models in the observed frame energy range 2.5 – 10 keV.

Obs. Id[a]	$\log(Z_{cwa18\times2})$[a]	$\log(Z_{zwabs})$[b]	$\log(Z_{R_{swind1}})$[c]	$\log(Z_{zxipcf})$[d]	$\log(Z_{cwa18})$[e]
0111570201	-4.4	-1.5	-0.1	-0.8	0
0111570101	-1.4	-0.6	-2.2	-1.1	0
0029740801	-14.8	-4.5	-2.7	0	-0.6
0029740701	-11.2	-3.2	-0.2	-0.1	0
0029740101	-5	-2.2	-0.5	-0.1	0
0693781401	-3.6	-0.5	0	-0.8	-0.5
0693781301	-21.5	-1.6	0	-0.4	-1.1
0693781201	-18.5	-4.3	-1.5	-0.7	0
Total	-78.2	-16.2	-5	-1.7	0

[a] *XMM-Newton* observation Id.
[b] Logaritmic Bayesian evidence for the model `cwa18 * (zpowerlw + pexmon + reflionx)`.
[c] Logaritmic Bayesian evidence for the model `cwa18 * (zpowerlw + pexmon + blur(pexmon))`.
[d] Logaritmic Bayesian evidence for the model `cwa18 * ( pexmon + relxill)`.

Table 4.7: Comparison of the total sample Bayesian evidence for the models `cwa18 * (zpowerlw + pexmon)` and `cwa18 * (zpowerlw + pexmon + blur(pexmon))` with and without two absorption Gaussians component at energies 6.7 and 6.97 keV. We use twice the component `zgauss` to model the lines and in the table we write that in short as `G × 2`. We fit the models in the observed frame energy range 2.5 – 10 keV.

Model [a]	log10(Z)[b]
`cwa18*(zpowerlw+pexmon)`	-182.5
`cwa18*(zpowerlw+pexmon − G × 2)`	-181.9
`cwa18*(zpowerlw+pexmon+kerrconv(spin=1)(pexmon))`	-10.4
`cwa18*(zpowerlw+pexmon+kerrconv(spin=1)(pexmon) − G × 2)`	-10.1
`cwa18*(zpowerlw+pexmon+kerrconv(spin=0)(pexmon))`	-2.3
`cwa18*(zpowerlw+pexmon+kerrconv(spin=0)(pexmon) − G × 2)`	0

[a] Model components.
[b] Logarithm of the Bayes evidence of the full sample normalized to the largest evidence.

Table 4.8: Comparison of the total sample Bayesian evidence for the models `cwa18 * (zpowerlw + pexmon + reflionx)`, `cwa18 * (pexmon + relxill)` and `cwa18 * (zpowerlw + pexmon + blur(pexmon))`. We fit the models in the observed frame energy range 2.5 – 10 keV.

Obs. Id[a]	$\log(Z_{\text{reflionx}})$[b]	$\log(Z_{R_{\text{kerrconv}}})$[c]	$\log(Z_{\text{relxill}})$[d]
0111570201	-5.7	-0.6	0
0111570101	-3.3	-0.8	0
0029740801	-20.5	-0.4	0
0029740701	-2.6	0	-0.7
0029740101	-14.8	-1.7	0
0693781401	-1.6	0	-1.2
0693781301	-4.8	-1.5	0
0693781201	-9.6	-0.1	0
Total	-60.3	-1.6	0

[a] *XMM-Newton* observation Id.
[b] Logaritmic Bayesian evidence for the model `cwa18 * (zpowerlw + pexmon + reflionx)`.
[c] Logaritmic Bayesian evidence for the model `cwa18 * (zpowerlw + pexmon + blur(pexmon))`.
[d] Logaritmic Bayesian evidence for the model `cwa18 * ( pexmon + relxill)`.

quantities.

We find that this model describes the data better than any other model combination we chose (see Figure 4.2) and fits the spin and inclination parameters consistently over the eight observations (see Figure 2.4).

As a test, we compare the model with `relxill` and two negative Gaussian at 6.7 and 6.97 keV with the same model but only one of the two lines at the time (see Table 4.9).

Even after a visual inspection, the model seems to fit the data well. However, we can still observe a positive residuum at 8 keV that might mirror the behavior of the background.

Finally, we apply the hierarchical Bayesian model (HBM) similarly as described in the previous chapter to calculate the mean and sigma of the disc inclination (see Figure **??**). We parametrize the posterior distributions of inclination and spin by modelling them with a beta distribution, as shown in Figure 4.5 and 4.6. We find that the mean of the inclination angle is $43.79^{+0.86}_{-0.98}$ while the mean spin is $0.29^{0.11}_{-0.12}$ (see Figure 4.7). The standard deviation of the population of both parameters is an upper limit. This shows that the method does not detect significant variation among the eight posterior distributions.

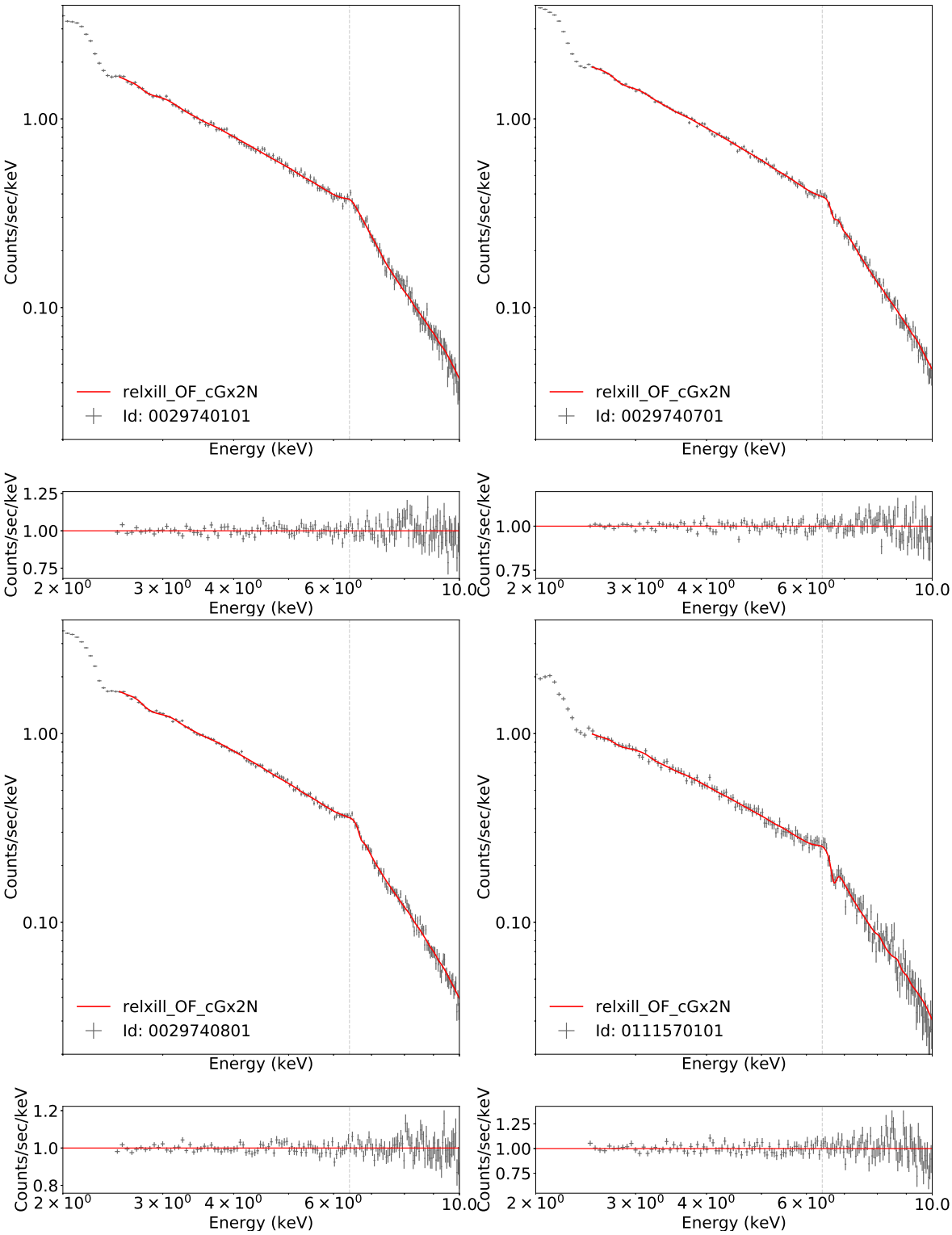
Counts/sec/keV
1.00
0.10
relxill_OF_cGx2N
Id: 0029740101
Energy (keV)
Counts/sec/keV
1.25
1.00
0.75
2 × 10^0
3 × 10^0
4 × 10^0
6 × 10^0
10.0
Energy (keV)
Counts/sec/keV
1.00
0.10
relxill_OF_cGx2N
Id: 0029740701
Energy (keV)
Counts/sec/keV
1.00
0.75
2 × 10^0
3 × 10^0
4 × 10^0
6 × 10^0
10.0
Energy (keV)
Counts/sec/keV
1.00
0.10
relxill_OF_cGx2N
Id: 0029740801
Energy (keV)
Counts/sec/keV
1.2
1.0
0.8
2 × 10^0
3 × 10^0
4 × 10^0
6 × 10^0
10.0
Energy (keV)
Counts/sec/keV
1.00
0.10
relxill_OF_cGx2N
Id: 0111570101
Energy (keV)
Counts/sec/keV
1.25
1.00
0.75
2 × 10^0
3 × 10^0
4 × 10^0
6 × 10^0
10.0
Energy (keV)

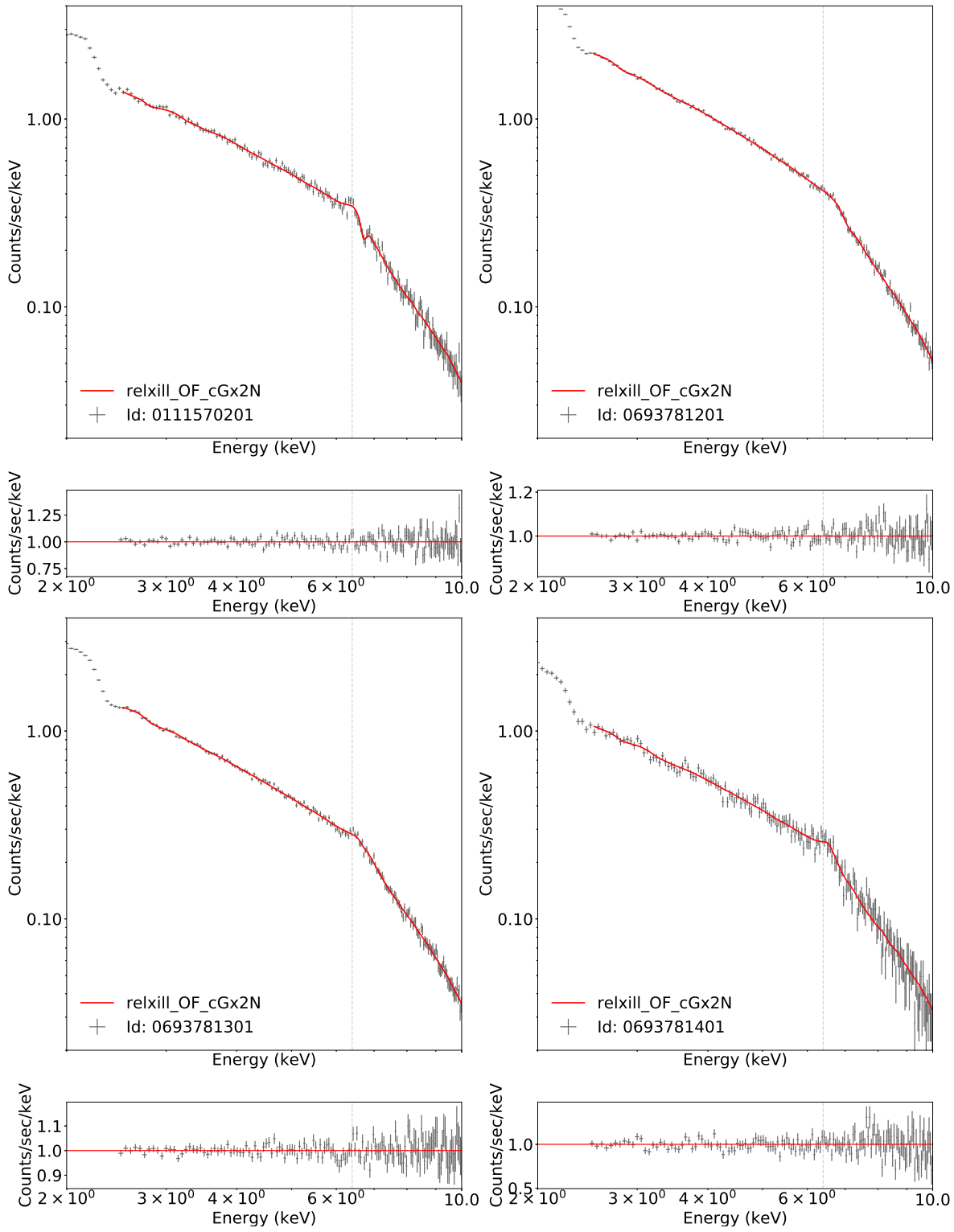

Figure 4.2: Best fit model with residua. The model here represented is `cwa18*(pexmon + relxill - 2 × G)` (in red). The values shown here represent the mean and the 68% confidence interval.

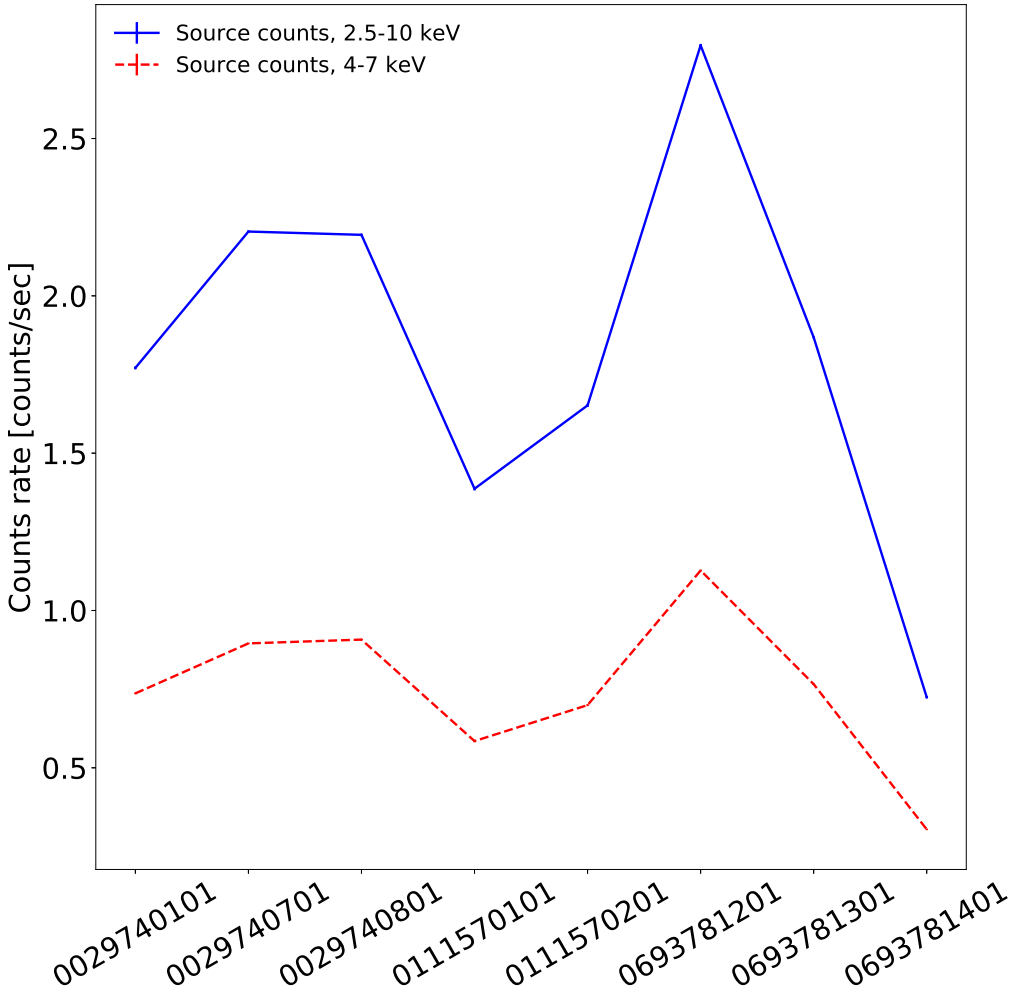

Figure 4.3: Source count rate in the 2.5–10 keV and 4–7 keV energy range for all eight observations.

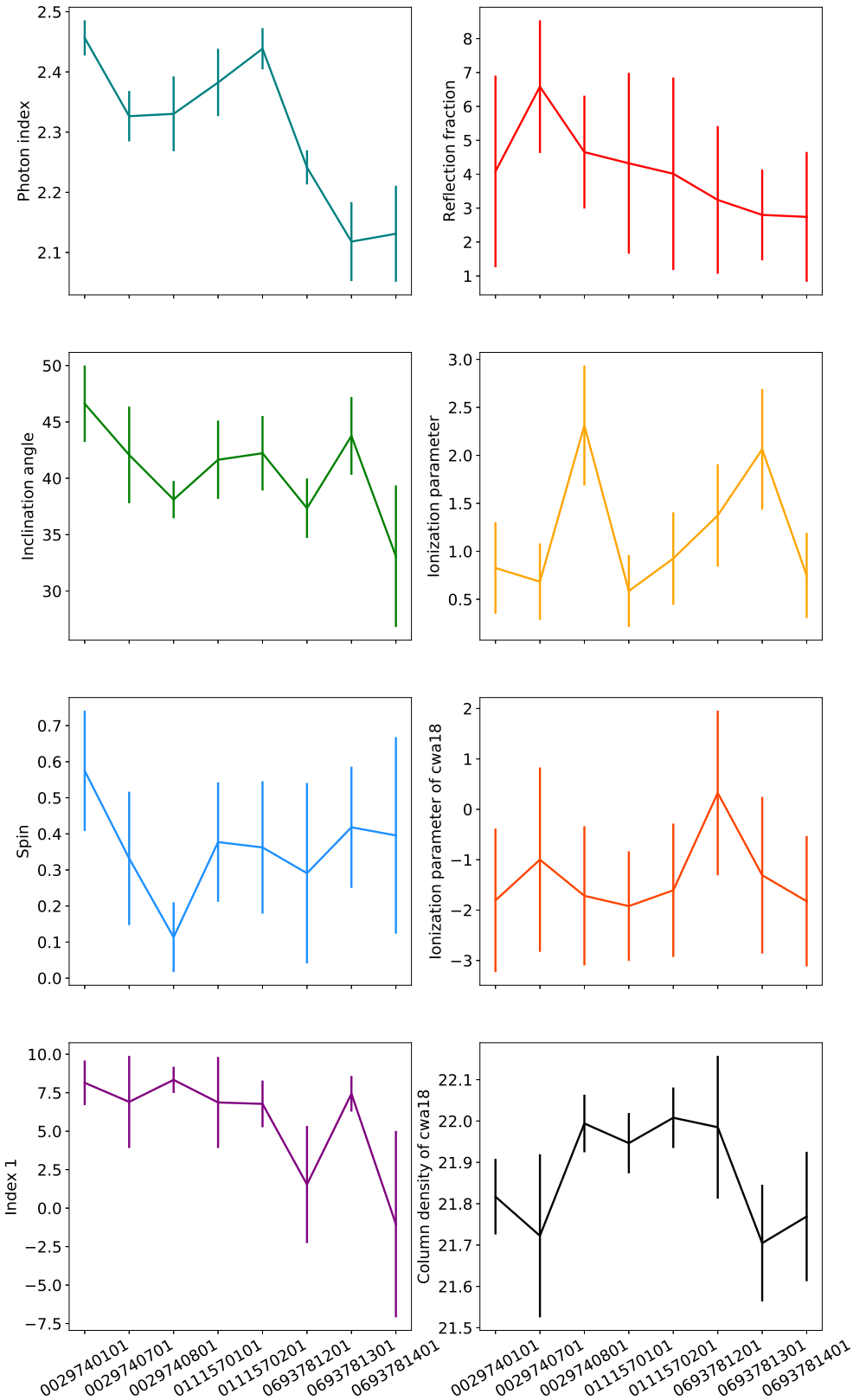

Figure 4.4: Best fit parameters for the model `cwa18*(pexmon + relxill - 2G)` for all eight observations. The value reported here are the mean of the posterior distribution and the 68% confidence interval for the most relevant free parameters of the model for every observation.

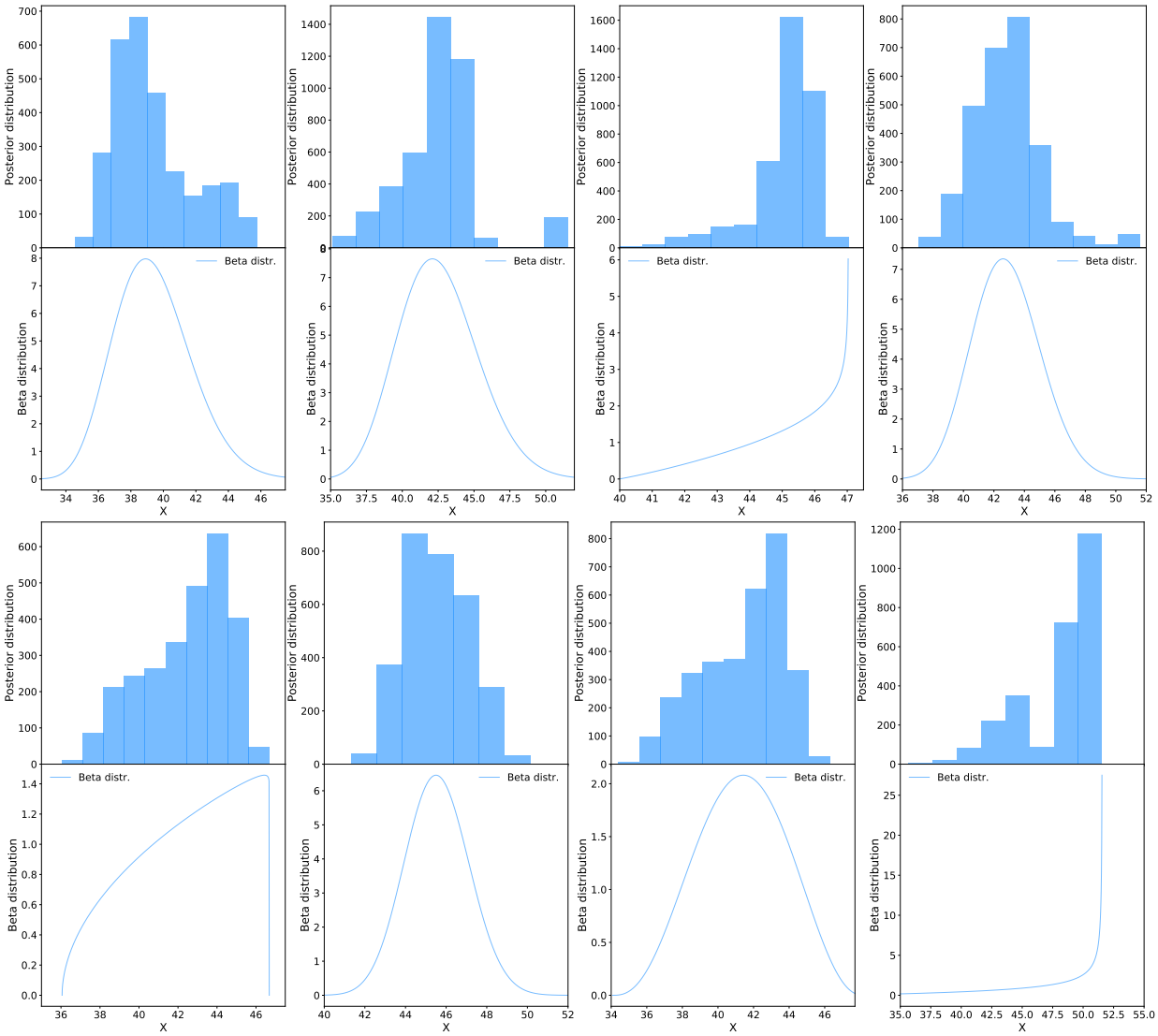

Figure 4.5: *Top:* Posterior distribution of the inclination angle of the eight observations of MCG-6-30-15 *Bottom:* their respective fit with a beta distribution. The inclination parameter for these high quality spectra is very well constrained.

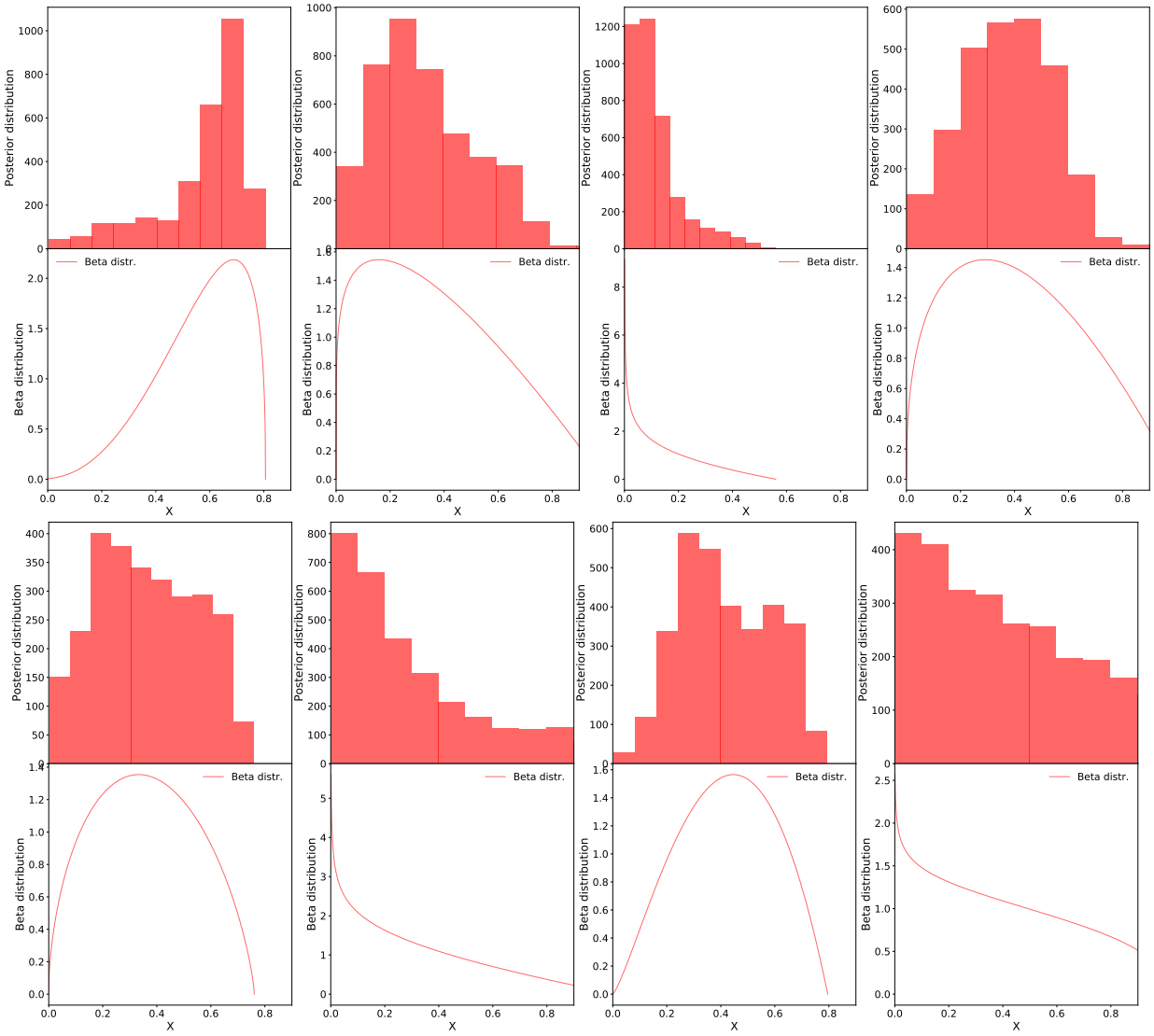

Figure 4.6: *Top:* Posterior distribution of the spin of the eight observations of MCG-6-30-15 *Bottom:* their respective fit with a beta distribution. The spin parameter is not constrained very well.

Table 4.9: Comparison of the total sample Bayesian evidence for the models `cwa18 * (pexmon + relxill - 2xG)`, `cwa18 * (pexmon + relxill-G(6.7keV))` and `cwa18 * (pexmon + relxill-G(6.97keV))`. We fit the models in the observed frame energy range 2.5 – 10 keV.

Obs. Id[a]	$\log(Z_{2G})$[b]	$\log(Z_{R_{G-6.7keV}})$[c]	$\log(Z_{G-6.97keV})$[d]
0111570201	-1.1	0	-2.5
0111570101	-0.6	0	-1.8
0029740801	-1	0	-0.5
0029740701	-2.1	-0.5	0
0029740101	-0.3	-0.1	0
0693781401	-0.3	0	0
0693781301	-0.3	0	-0.1
0693781201	0	-0.1	0
Total	-5	0	-4.4

[a] *XMM-Newton* observation Id.
[b] Logaritmic Bayesian evidence for the model `cwa18 * ( pexmon + relxill)`.
[c] Logaritmic Bayesian evidence for the model `cwa18 * ( pexmon + relxill - gauss)`.
[d] Logaritmic Bayesian evidence for the model `cwa18 * ( pexmon + relxill +gauss)`.

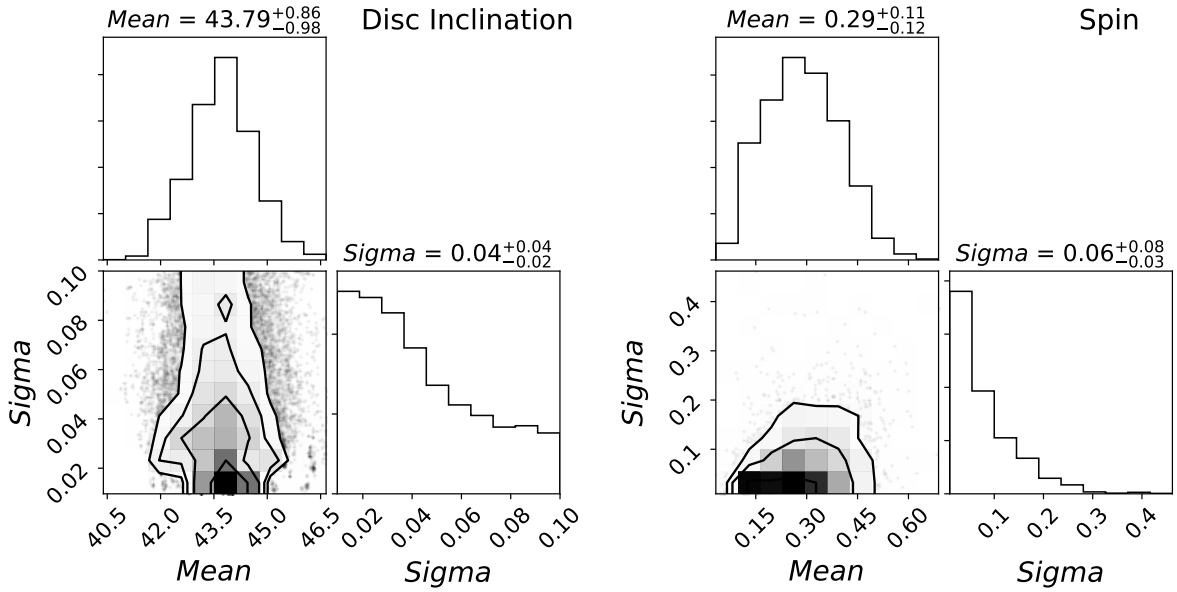

Figure 4.7: *Left:* Average inclination angle for MCG–6-30-15 calculated with the hierarchical Bayesian model. *Right:* Average spin found with the same method. We find a mean inclination angle of $43.79^{+0.86}_{-0.98}$ degrees and a mean spin of $0.29^{+0.11}_{-0.12}$.

4.5 Discussion

The goal of this work is to test different absorption and reflection models to find which one fits consistently eight *XMM* observations of MCG–6-30-15. We use Bayesian model comparison to select between the absorption models `wabs`, `swind1` and `cwa18` from Nandra et al. (2007) and the reflection models `kerrconv`, `reflionx` and `relxill`. Since we have eight observations of the same object, we assume that the "perfect" model will fit immutable parameters, for example, the inclination angle and the spin, consistently over the eight observation.

The three reflection models represent respectively a relativistic blurred reflection (`kerrconv`), a reflection component from an ionized disc without relativistic effects (`reflionx`) and a component that takes into account both the ionization from the disc and the relativistic blurring due to the proximity of the SMBH (`relxill`). We found that the model with only ionized reflection and absorption is not enough to fit the data but a relativistic component is also required (see Table 4.8).

The absorption component also should preferably model a layer of ionized absorption, in fact, `cwa18`, `swind1`, and `zxipcf` are strongly preferred over the simple photoelectric absorption model `zwabs` and the two-zone ionized absorber `cwa18*cwa18` (see Table 4.6). Between the models `cwa18` and `swind1`, the BF method prefers the `cwa18`.

At the end of the chain of model comparisons we find that the model that fits the data best is `cwa18*(pexmon + relxill - 2G)` (from now on referred to as end model) where `2G` are two negative Gaussians at 6.7 and 6.97 keV respectively. This model is also physically justifiable, as with the proximity of a SMBH one might expect the accretion disc to be ionized by the radiation emitted to be relativistically blurred around the SMBH. The two absorption features at 6.7 keV and 6.97 keV are consistent with resonant K shell absorption from highly ionized iron Fe XXV and Fe XXVI and were already found in previous work (see for example Nandra et al. 2007).

In Table 4.9, we compare the model with two absorption lines against the same model with only of the absorption lines at the time. The main difference is that the model with both absorption lines has one free parameter extra (the norm). The cumulative evidence for all the eight observations is higher for the model with only the 6.7 keV absorption line. However, by looking at the evidence for the single observations it is harder to clearly rule out the presence of the absorption line at 6.97 keV. The only two observations that show a clear difference in evidence between the two models with a single absorption line are 0111570201 and 0111570101 because (as one can see in Figure 4.2) the absorption line at 6.7 keV is clearly stronger than the 6.97 keV one. Thus, we can expect both the lines to be required in the fit. The model with both the absorption lines present is penalized over the models with only one line due to the larger number of parameters.

One desired quality of a well-fitting model should be the consistency of the values of parameters we do not expect to vary among the eight observations. For example, we expect the spin and inclination parameters to be constant among all the observations of the same object. In fact, the spin and inclination parameters for the end model do not show significant variation among the eight different observations. We can see this both in Figure 2.4 and 4.7, where the standard deviation resulting fro the HBM (that is, the spread of the population) is an upper limit.

We calculate the average inclination and spin of the observation by taking into account the shape of the single posterior distribution using a HBM (see Chapter 3, section 3.6). We find average inclination angle of $43.79^{+0.86}_{-0.98}$ degrees and average spin of $0.29^{+0.11}_{-0.12}$. The first result is consistent (if slightly higher) with the work of Miniutti et al. (2007), that found a disc inclination angle of $38^{+0.86}_{-0.98}$ degrees. However, the spin value is much lower than the value a = $0.989^{+0.009}_{-0.002}$ at 90% found by Brenneman & Reynolds (2006) and (Miniutti et al. 2007) but more similar to the value $a = 0.49^{+0.20}_{-0.12}$ found by Patrick et al. (2011) in deep *Suzaku* observations of MCG–6-30-15. The study by Patrick et al. (2011) seems to rule out the presence of maximally spinning SMBH in five nearby Seyfert I (including MCG-6-30-15).

Considering the work in the two previous Chapters (see Chapter 2 and 3), the spin value found here might seem a bit surprising. In fact, in our previous work on large samples of *Chandra* low signal-to-noise spectra, we found that the model with higher evidence was the one with maximally spinning SMBH.

The unexpected spin value obtained here could also indicate that the model we chose still does not fit the data, or it could indicate a difference between nearby AGN and the AGN at the peak of accretion (z = 0.5–4). To test this more in detail we should apply the method presented in this work to a larger sample of nearby *XMM* observations.

4.6 Summary and conclusion

MCG-6-30-15 is the first source where a broadening of the Fe Kα line was observed (Tanaka et al. 1995). The X-ray spectrum of this source shows complex absorption and reflection features and the physical origin of the Fe Kα line is still debated. We analyzed 8 *XMM* spectra of this source taken in the time period between 2000 and 2013 to determine a model that would explain the spectra and their variability using BXA and Bayesian model comparison. We find that to explain the features in the spectra ionized absorption is required but ionized reflection is not sufficient. The reflection component of the spectra seems to be best fitted by a combination of ionized and relativistic reflection, modeled with the XSPEC model `relxill`. We tested several absorption models, from photoelectric absorption (`zwabs`) to ionized absorption with partial covering fraction and free redshift to simulate out-/inflows (`zxipcf`). The absorption model with higher evidence is a ionized absorption model developed by Nandra et al. (2007) (`cwa18`). However, since to better fit the data we need to add two absorption lines at 6.7 and 6.97 keV, it seems that there are outflows not properly modeled by `cwa18`, thus the more complex absorption model `zxipcf` might be only rejected due to the larger number of free parameters.

Our main findings are:

- The eight *XMM* spectra of MCG-6-30-15 are best fit with a spectrum containing an ionized absorption and complex reflection. The Bayes factor method indicates that a model containing ionized reflection alone is not sufficient to fit the data but it requires also relativistic broadening.

- We constrain the inclination angle for MCG–6-30-15 using a hierarchical bayesian model and we find a value of $43.8^{+0.9}_{-1.0}$ degrees.

- We find that the SMBH in MCG–6-30-15 core has intermediate spin using the same hierarchical model. We find a spean average of $0.29^{+0.11}_{-0.12}$.

Chapter 5

Summary and conclusions

The aim of this work was to study the properties of the broad Fe Kα line and Compton reflection continuum at high redshift, its relation with the narrow core of the line and other physical parameters of the AGN, and to contribute to finding an answer to open issues regarding the ubiquity and the physical origin of the broadening of the Fe Kα line.

While the narrow core of the Fe Kα line arises when the primary X-ray continuum is reflected by the cold molecular torus, the broad wings of the line are produced in the innermost part of the accretion flow surrounding the central SMBH. The radiation emitted so close to the ISCO is heavily affected by the extreme gravitational field of the SMBH, thus by studying the line profile of the Fe Kα feature we can theoretically measure general relativity effects in the population of growing SMBH. For example, the broadening of the Fe Kα line could be a good tracer for the BH spin. In fact, higher spins would lead to smaller ISCO, and that in turn would make the general relativity effects on the line stronger, leading to a broader profile than the slowly spin scenario would produce.

The line profile of the Fe Kα feature is also strongly affected by the geometry of the matter surrounding the SMBH. The strong dependence of the broadening of the line with the inclination of the accretion disc can be used to test the unification scheme of AGN and the structure of the molecular torus.

The broad reflection features, observed definitely in the *ASCA* observation of MCG-6-30-15 by Tanaka et al. (1995), were detected consistently in high quality spectra of nearby bright AGN (e.g. Nandra et al. 1997a; Guainazzi et al. 2006; Nandra et al. 2007; de La Calle Pérez et al. 2010).

The detection of the feature in higher-redshift AGN is more problematic, due to the generally lower S/N of the data.

In the past, many studies have been conducted to address this issue not only for single sources but also for large samples of AGN (e.g. Streblyanska et al. 2005; Chaudhary et al. 2012; Falocco et al. 2012, 2013, 2014). Authors like Falocco et al. (2012, 2013, 2014) and Liu et al. (2016) relied on stacking techniques to obtain and fit an averaged spectrum of several AGN X-ray observations and gain insight on the population of these objects.

In this thesis, I aim to address the issue of the broad Fe Kα line and reflection at high-z using more robust Bayesian methods. Thanks to Bayesian inference, we can fit the spectra

individually and infer the properties and characteristics of the sample by stacking the evidence of every sources instead of fitting a stacked spectrum. This method can yield gain information even from faint sources and avoid artificial broadening that might be induced by stacking spectra of sources at different redshift.

In Chapters 2 and 3, I fit AGN X-ray spectra from the deepest *Chandra* deep fields using the Bayesian framework BXA (Buchner et al. 2014). The goal is to determine if the sample is best fit by modeling continuum and a narrow reflection component from the torus or if a broad disc reflection component is also required.

In Chapter 4, I test the model applied in the previous two chapters on a high signal-to-noise source, MCG–6-30-15, with eight *XMM* observations. I address the ongoing debate on the origin of the broadening of the Fe Kα line: relativistic effects vs. complex ionized absorption of the continuum. I fit the eight *XMM* spectra with BXA testing different types of absorption and reflection models.

5.1 Future outlook

The nature of the broad Fe Kα line and its relation with the BH spin and geometry of the AGN still poses many issues. The method presented in this work can be extended to samples observed with other X-ray instruments (for example *eROSITA* and *XMM*) to gain statistical significant constraints on the detection of the feature. Furthermore, to measure unambiguously parameters like spin and disc inclination, we might have to wait for the next generation of X-ray instruments, for example, *Athena*.

5.1.1 XMM-Newton

In this work, we mainly use AGN spectra observed with *Chandra*, since this telescope can resolve faint sources at higher redshift. However, as discussed in Chapter 4 and by Nandra et al. (2007), the serendipitous *XMM-Newton* archive could also supply an excellent sample to extend our analysis.

XMM-*Newton* provides us with extremely high signal to noise spectra, thanks to its unprecedented effective area. Therefore, nearby bright spectra of AGN observed with *XMM-Newton* are good candidates to gain more insights on the Fe Kα line profile.

In particular, it would be an interesting experiment to combine the method used in the previous chapters, especially Chapter 4, with the analysis exposed by Nandra et al. (2007) to all the bright nearby Seyferts with similar characteristics as MCG–6-3-15. For example, it would be interesting to apply the analysis developed in 4 to the other sources examined in Patrick et al. (2011) (e.g. NGC 3516, NGC 3783, and NGC 4051) to constrain the spin with a different method. Moreover, many authors found contradicting results on the presence or not of the broad Fe Kα wings in the spectrum of NGC 4051 and BXA might be able to shed light on this matter. There are 19 pointed observations of NGC 4051 in the *XMM* archive taken in the years from 2002 to 2018, thus our analysis could provide useful insights.

The *XMM* archival data could be also used to expand the analysis in Nandra et al. (2007). We looked for sources with the same criteria as by Nandra et al. (2007) in the *XMM* archive. We cross the serendipitous *XMM* catalog 3XMM with Veron, Cetty 2001. We restrict our analysis to nearby sources with z<0.05 and we exclude Seyfert 2, radio-loud sources, and blazars. Moreover, we require high SNR in the hard band. If restricting our study to sources with more than 30000 counts in the epic-PN spectrum in the 2–10 keV band we would get a sample of 66 *XMM* archival observations. However, this count-cut might not be necessary while using BXA, since BXA allows us to include in the analysis even fainter sources, thus the sample could result even larger (of the order of hundreds of objects).

Moreover, the work presented in Chapters 2 and 3 would be enriched and expanded by a similar analysis applied to the *XMM* deep fields. In a way, *Chandra* and *XMM* are complementary in their deep-survey capabilities. *Chandra* has higher spatial resolution, thus the sources observed with *Chandra* have a position accuracy of ≈0.3–1" compared to the accuracy of ≈1–3" of *XMM*. While *Chandra* deep observations do not suffer from significant confusion, *XMM* observations start to be confused already at exposure of > 200 ks (Brandt & Hasinger 2005). However, *XMM* has a larger field of view, ≈2.5 times the one of *Chandra*, and it has a larger collecting area (observing approximately double as many photons as *Chandra* in the same exposure), allowing efficient X-ray spectroscopy above the confusion flux.

XMM-Newton observed also several deep and wide fields, for example, the deepest *XMM* fields are the XMM-XXL, the Lockmann hole, and the XMM-CDFS.

The Lockman hole observed with *XMM* (Hasinger 2004; Brunner et al. 2008) covers an area of ∼18 deg^2 with an exposure of 1.6 Ms and 226 hard selected sources, while the XMM-XXL is a wide field covering an area of ∼ 50 deg^2 with an exposure time of 10 ks per *XMM* pointing (Menzel et al. 2016). The XMM-XXL sources were already analyzed in detail in Liu et al. (2016) and (Buchner et al. 2015) using BXA, however, models containing a relativistic reflection were not tested. Although, the sources might be too faint to accurately determine the characteristics of the broad Fe Kα line (see Fig. 7 in Liu et al. (2016)). On the other hand, the Lockmann hole observed with *XMM* has a flux depth similar to the AEGIS field (see Chapter 3) and thus it could be used as a further sample to apply our analysis.

The XMM-CDFS field is the *XMM* equivalent of the *Chandra* deep field CDFS analyzed in Chapters 2 and 3. With an exposure of 3 Ms and 339 sources in the 2–10 keV (Ranalli et al. 2013), the sources of the XMM-CDFS would allow us not only to gain information on the full sample but probably also to be studied in their individuality. In fact, the higher collective area of *XMM* makes sure that *XMM* spectra have a higher S/N that *Chandra* spectra.

5.1.2 eROSITA

eROSITA (extended Roentgen Survey with an Imaging Telescope Array) is the principal instrument on board of the Spectrum-Roentgen-Gamma (SRG) mission launched from Baikonur in July 2019 and result of a German-Russian collaboration. eROSITA is placed in the Lagrangian point L_2, which lies on the line connecting Earth and Sun and beyond Earth, and it will image the X-ray all-sky up to energies of 10 keV. In the hard X-ray band (2–10 keV), eROSITA will capture the first-ever all-sky image at those energies, while in the soft band (0.5–2 keV) the all-

sky survey mapped by eROSITA will reach unprecedented depths, it will be about twenty times more sensitive than the ROSAT all-sky survey.

eROSITA comprises seven identical Wolter Type-I modules of 54 nested mirrors shells. At the focal point of the seven mirror modules are placed seven X-ray built by MPE on the model of the pn CCD on board *XMM-Newton*.

The advantage of having multiple mirror systems over a single larger one is that the focal length in the multiple mirror case is going to be shorter, thus the instrumental background is reduced. The all-sky survey will be followed by 3.5 years of pointed observations.

eROSITA already completed the first of the eight all-sky images it will take over the course of four years. This first image revealed a million of X-ray sources, 10 times more than previously observed by *ROSAT* and 4 times deeper. The deepest regions of the *eROSITA* all-sky with have a flux comparable to the XMM-XXL and 2XMM fields, so around 2×10^{-14} cm^{-2}s^{-1} in the 2–10 keV range, and will detect 3 millions AGN. The whole population of *eROSITA* AGN will mainly comprise unobscured sources with luminosity peaking at 10^{44} erg/s and redshift 1.

This means that very likely we will not be able to constrain the Fe Kα line in the single sources.

Moreover, *eROSITA* is especially sensitive in the energy range below 1 keV. For this reason, studying the Fe Kα feature in detail and in the spectra of single sources might prove challenging if not impossible. In fact, if we want to observe a Fe Kα feature in the range of highest sensitivity of *eROSITA*, the source where this feature is emitted should have redshift z>5.4. Considering that the redshift distribution of the *eROSITA* observations peaks at z~0.8, one cannot expect that sources at z>5.4 will be observed, and if they will they probably will not have signal-to-noise high enough for spectroscopy. However, at the end of its four years long X-ray all-sky survey, *eROSITA* will have observed millions of AGN in the X-ray (Kolodzig et al. 2013). Thanks to the BXA and HBM methods, we are able to study the characteristics of a very large sample, like the *eROSITA* all-sky will be, of low signal-to-noise AGN.

As discussed in Chapter 3, a large sample of many faint spectra can be used to gain information on the population of accreting SMBH, as long as some S/N cut is accounted for.

(Kolodzig et al. 2013) found that after four years of *eROSITA* observations, the deepest sources will have from 100 to 500 (at the poles) counts in the 2–10 keV with the method developed in (Georgakakis et al. 2008). Since it's enough that only 0.5% of the *eROSITA* AGN to have 100 counts in the 2–10 keV to apply the method used in 2, the *eROSITA* all-sky will for sure provide a valuable sample for the Fe Kα analysis.

5.1.3 XRISM

Another future mission that will prove very important to deepen our current understanding of the Fe Kα line will be the X-ray Imaging and Spectroscopy Mission (*XRISM*) (Williams et al. 2019). *XRISM* is a JAXA/NASA mission with ESA contributions scheduled to be launched in early 2022. *XRISM* is the heir of ASTRO-H and will carry forward the project by performing high-resolution X-ray spectroscopical observations. One of the two instruments onboard is an X-ray spectrometer, called Resolve, that comprises an X-Ray Mirror Assembly paired with an X-ray calorimeter. The energy resolution of this instrument will be of 5–7 eV in the 0.3–12

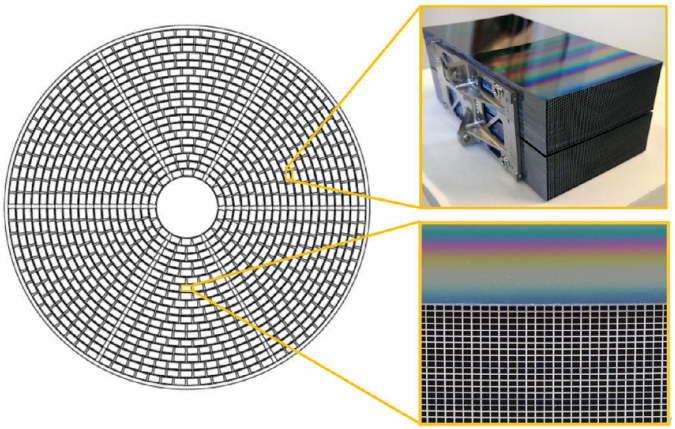

Figure 5.1: Scheme of the *Athena* high-performance Silicon pore optics (SPO). The mirror module (*left*) will an outer diameter of 2.4 meters and will comprise 678 SPO mirror modules (*bottom right*). The mirrors will be grouped in modules (*top right*) of 70 mirror plate pairs, arranged in four stacks of 35 plates. Each of this module on its own is a Wolter Type I telescope. (Image credits: Wille et al. (2015))

keV energy range, which is similar to the energy resolution achieved by *Hitomi*. The second instrument on board, called Xtend, is a CCD detector collecting the photons focused by a second identical X-Ray Mirror Assembly.

XRISM will be very important for bright sources, such as MCG–6-30-15 (see Chapter 4). In fact, the energy resolution of Resolve will allow us to actually disentangle the narrow core of the Fe Kα feature from the broad wings and will play a key role in finally determine the absorption components. The narrow component measured with Resolve will allow us to determine the geometry and location of the torus. In the meantime, the spectra collected with Xtend will have more photons and thus will allow us to constrain the broad component of the Fe Kα line.

XRISM would provide great insights on the bright Seyfert sources mentioned above, such as NGC 4051, NGC 3516, NGC 3783, and MCG–6-30-15 especially if used in tandem with *XMM-Newton*. In fact, observation from *XRISM* might be used to constrain absorption features and layers in the spectra, and these than could be added to spectral analysis of *XMM* spectra as in Chapter 4. That way, we would be able to study the reflection component of the *XMM* sources without worrying about the features of the absorption model.

5.1.4 *Athena*

However, the launch of *Athena* (Advanced Telescope for High Energy Astrophysics) will perhaps be the most promising event in the future of Fe Kα studies. The satellite *Athena* will be the key instrument for studies on the Fe Kα feature.

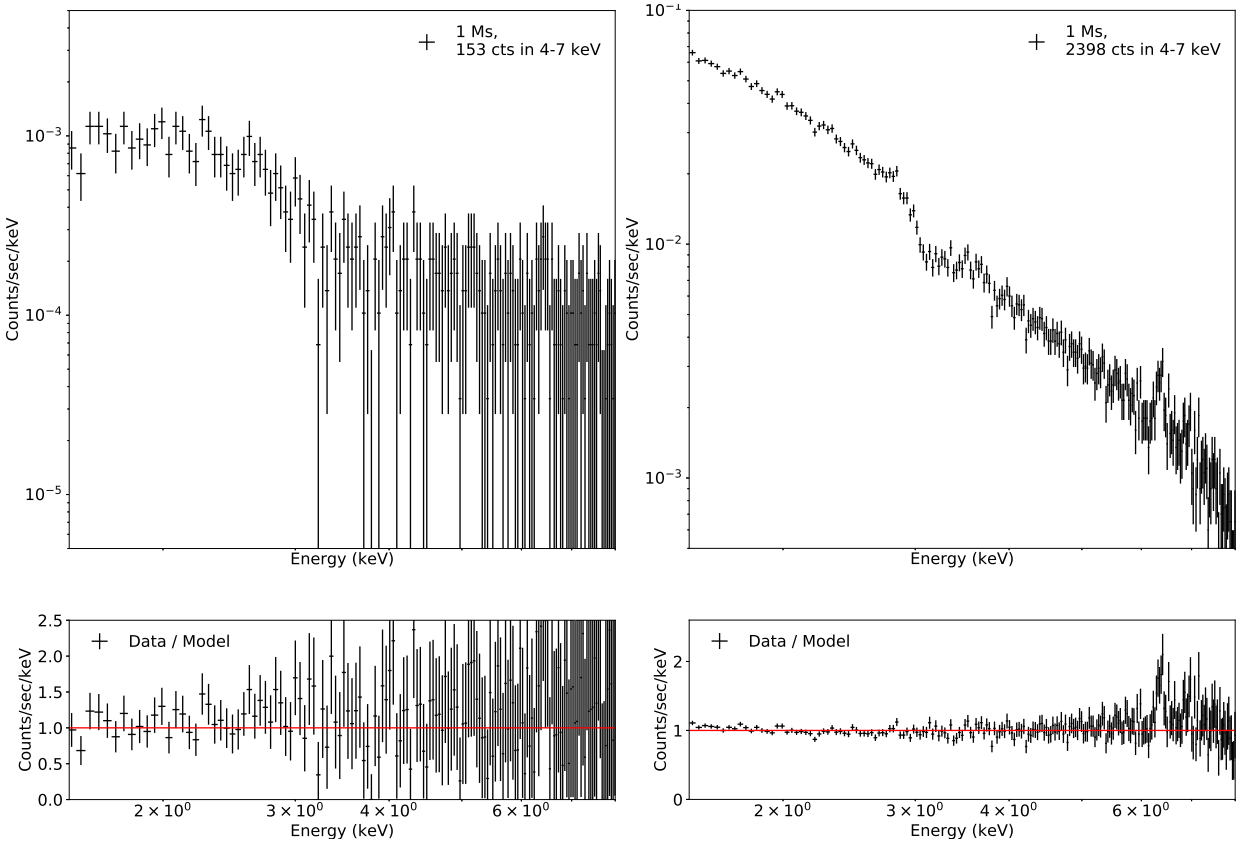

Figure 5.2: Comparison for *Chandra* (*left*) and *Athena* (*right*) spectra simulated with a spectrum containing a narrow and a broad reflection component and 1 Ms exposure as described in Chapter 2. The bottom panels are showing only the reflection component for the three instruments. The *Athena* spectrum has clearly a higher S/N ratio than the other two telescopes and the Fe Kα line is clearly visible. This shows that at a typical deep survey depth we will be able to study single sources observed with *Athena* and we will not need to study the sample as a whole.

Athena is the second L(large)-class mission, after the Jupiter Icy Moon Explorer, selected by ESA to be part of the Cosmic Vision Program. It is being developed to be launched in the 2030s. *Athena* will be a hundred times more sensitive of *Chandra* and *XMM-Newton* and its primary goal will be of mapping hot gas structures in the Universe and detect black holes. The mission will address how baryonic matter condensed to form galaxies and clusters.

Athena will carry a new type of X-ray optics (see Figure 5.1), the High-performance Silicon pore optics (SPO), with 12 meter focal length and 5 arcsec on-axis angular resolution. SPO technology uses a modular approach to simplify the mirror module production. The main telescope is segmented into smaller segments of about $10 \times 5 \times 20\,\mathrm{cm}^3$. In total, the configuration will comprise 678 SPO mirror modules arranged in 15 rows with an outer diameter of $\sim 2.4\,\mathrm{m}$. Each mirror module contains 70 mirror plate pairs, grouped in four stacks of 35 plates, two hyperbolic and two parabolic (see Figure 5.1, top right). The mirror plates are coated with iridium with an overcoat of boron carbide (Bavdaz et al. 2015; Wille et al. 2015). Each mirror modules itself is a Wolter I telescope.

On the focal plane, there will be two instruments, the wide-field imager (WFI) and the X-ray integral field unit (X-IFU). WFI will provide imaging in the 0.2 – 15 keV energy range over a wide field, together with spectrally- and time-resolved photons counting. X-IFU is a cryogenic X-ray spectrometer, based on a large array of transition-edge sensors (TES), that will offer 2.5 eV spectral resolution over the energy range from 0.2 to 12 keV.

The mirror structure will be mounted on a hexapod, that will allow the optics to be tilted to focus the X-ray photon on the selected focal plane instrument. This configuration will also allow us to correct for misalignment due to stresses during the launch.

Presently, the field of X-ray spectroscopy is afflicted by low signal to noise and low spectral resolution, especially in the big X-ray surveys. Even if we have at our disposal an incredibly large database of AGN observations in the X-ray, it is often difficult to reach conclusions about the population properties due to the low quality of the majority of these spectra. The first and only observation taken by *Hitomi* (Hitomi Collaboration et al. 2016) showed us the enormous potential of calorimetry in X-ray astronomy and *Athena* gives new hope to those of us attempting to validate complex models using low counts spectra. *Athena* will finally settle the debate surrounding the origin of the Fe Kα line profile.

In fact, how we mentioned above, deep field observations with the Athena WFI (Rau et al. 2013; Meidinger et al. 2016) will have one or two orders of magnitude more photons per unit exposure than *Chandra*. Moreover, *Athena* has a spectral resolution of 2.5 eV vs. the 0.1 keV of *Chandra*.

As a visual indication of the difference between *Chandra* and *Athena* we simulate two sets of unabsorbed spectra with redshift z=0.5 and power-law norm of 1×10^{-5} containing a primary power-law and bot narrow and broad reflection components (as explained in Section 2.3.1). In the left panel of Figure 5.2 you can see a spectrum simulated using the response files of a source in the CDFS 4Ms (CID-190) for *Chandra* with 1 Ms exposure. In the right panel of Figure 5.2, the spectrum is simulated in the same way but using the on-axis response files of *Athena* (we thanks Dr. Arne Rau for the response files). The total count in the 4–7 keV energy range for the *Chandra* spectrum is 153 counts, the *Athena* spectrum has 2398 counts, 15 times more than *Chandra*. In the bottom panels Figure 5.2 one can see the simulation without the power-law

component. The broad Fe Kα line is clearly visible in the left bottom panel while it is much harder to detect in the *Chandra* simulation.

The simulation is a good indication of how powerful *Athena* will be to study the Fe Kα line. In fact, *Athena* will observe ten times more counts than *Chandra* in the 4–7 keV (see Figure 5.2) and the spectra of *Athena* will less noisy. By studying the future *Athena* deep field we will be able not only to constrain population features such as spin and inclination angle of the full sample, but we will be able to constrain these parameters also for single observations. Moreover, the quality of the *Athena* spectra will be enough to test more complex models similarly as in Chapter 4. For this reason, we will be able to test more efficiently the geometrical configurations of the corona and the obscuring torus.

Therefore, we can expect that the future will reserve many exciting discoveries for the future, and *Athena* will solve once and for all the mysteries still bound to the Fe Kα line profile.

Appendix A

Bayesian Inference

In this thesis, we center our analysis on model comparison using Bayesian inference. We employ the software Bayesian X-ray Analysis (BXA) to fit different models to the data and obtain the Bayesian evidence Z to those models together with the best-fit parameters. In the following chapter, we introduce the basics of Bayesian inference and of the algorithm on which BXA is built, the Nested Sampling Algorithm (NSA).

A.1 Statistical inference

While descriptive statistics use quantities like average, mean, spread, etc. to characterize and summarize the sample, inferential statistics study something more general than the properties of the sample. The goal is to find a pattern that does not just hold for the particular sample but also for the parent population from which the sample was drawn. All methods in inferential statistics aim to achieve one of these three goals:

- Parameter estimation, that is the estimation of some unknown constants that determine the properties of the distribution.
- Data prediction. After already having estimated the parameters, they can be used to predict future data.
- Model comparison, which is the process of selecting one model out of 2 or more models as the one better describing the data. A model is basically a set of postulates about the process generating the data.

The two main "philosophic currents" in inferential statistics are frequentist and Bayesian inference.

The differences between Bayesian and frequentist framework originates from the way in which the concept of probability itself is interpreted.

In the frequentist approach, only repeatable random events (like the flipping of a coin) have a probability. This probability is equivalent to the long-term frequency of occurrence of the event

in question. Frequentists do not attach any probability to a hypothesis or to any unknown but fixed value.

Bayesian probability theory differs from the frequentist one in two fundamental ways: 1) in the interpretation of the term 'probability' and 2) in a different view of the origin of uncertainty. In Bayesian statistics, probability can be viewed as a degree of belief in the truth of a proposition. As a Bayesian, you can use probabilities to represent the uncertainty of every event and hypothesis. Hence, probabilities can be assigned also to unrepeatable events. Secondly, uncertainty is not only due to the intrinsic randomness of the object to be analyzed but can also result from incomplete information. It has been proved (Cox1946, Knuth2012) that Bayesian probability theory is the only theory that handles partial truths consistently.

A.2 Bayes' Theorem

The Bayesian approach to the concept of "probability" is the continuation of the Laplacian definition (that is the probability of an outcome A is equal to the number of outcomes in favor of A divided by the total number of outcomes in the sample space). In Bayesian reasoning, the probability $P(H|D)$ is a measure for the correctness or truth of the proposition or hypothesis H given the background information D. The notation $P(H|D)$ describes actually a conditional probability.

The posterior probability of the data given the model can be calculated by multiplying the *likelihood* function, $\mathrm{L}(\theta) = \mathrm{P}(\mathrm{D}|\theta)$, by the *prior distribution* (or sampling density for the data), $\pi(\theta) = \mathrm{P}(\theta)$

$$P(\theta|D) = \frac{P(D|\theta)P(\theta)}{P(D)}. \tag{A.1}$$

Here θ is the set of model parameters and D is the data associated with a measurement. In other words, the posterior distribution $P(\theta|D)$ is the probability that the true value of θ is between $(\theta, \theta + d\theta)$ given the data D. $P(D)$ is a normalization factor called evidence Z, or alternatively prior predictive, marginal likelihood, or marginal density of the data, that scales $P(\theta|D)$ to make it a proper probability density.

$$Z = \int d\theta P(D|\theta)P(\theta). \tag{A.2}$$

The prior incorporates our belief about θ before we carry out a measurement. In some cases, there is an obvious choice of prior to previous observations or outside knowledge/experience. However, when we do not know the behavior of θ we often choose an uninformative distribution that is either uniform or log-uniform. While θ may consist of a large number of parameters, we usually want to investigate only one or two at a time. To this purpose we *marginalize* (integrate) over the parameters we are not interested in (nuisance parameters) so as to obtain a marginalized posterior

$$P(\theta_i|D) = \iiint \prod_{k \neq i} P(\theta_k|D) d\theta_k = \frac{P(D|\theta_i)P(\theta_i)}{Z}. \tag{A.3}$$

The quantity $P(D|\theta_i)$ is called the marginalized posterior distribution. The Bayesian evidence is the completely marginalized likelihood

$$P(D) = Z = \int d\theta P(D|\theta)P(\theta). \tag{A.4}$$

The evidence serves as normalization of the posterior distribution $P(\theta|D)$. However, it can also be used to perform Bayesian model selection.

A.3 Bayesian model comparison

The Bayesian model comparison is a method of model selection based on Bayes factors, used to support one model over another, regardless of whether these models are correct or not.

Consider two models θ_1 and θ_2 not necessarily nested[1]. We wish to compare the models on the basis of the posterior probability of the model given the data. Using Bayes' rule, this is proportional to the prior probability for the model, $p(\theta)$ multiplied by the likelihood of the data given the model, $p(D|\theta)$. Thus the choice between M1 and M2 can be made on the basis of the ratio

$$\frac{p(\theta_2|D)}{p(\theta_1|D)} = \frac{p(\theta_2)}{p(\theta_1)} \times \frac{p(D|\theta_2)}{p(D|\theta_1)}, \tag{A.5}$$

that means, the prior odds ratio is equal to the posterior odds ratio times the factor of Bayesian evidences for the two models. Assuming that the two models are equiprobable a-priori, the first factor on the right side of the equation disappears. Thus the ratio of the posterior probabilities is determined by the factor

$$B_{21} = \frac{p(D|\theta_2)}{p(D|\theta_1)}, \tag{A.6}$$

called Bayes factor (BF). A large value of this ratio gives support for θ_2 over θ_1. The BF method is the Bayesian statistics equivalent to the classical likelihood-ratio test. However, the BF has the advantage that model comparison does not depend on any set of single parameters since the evidence is integrated over the prior space of all the parameters in the model. Moreover, the BF naturally introduces a penalty for models with larger prior space, preventing over-fitting (see Section A.4).

The BF is a continuous measure of the Bayes evidence, thus the evidence of different models can be compared but there is no universal way to determine whether the model is "good/strong" or "bad/weak". One popular way to quantify the strength of a model compared to another is Jeffrey's scale (see Table A.1).

However, by quantifying a continuous measure one might introduce subjectivity in the analysis and lose some information. For this reason, it is advisable to calculate thresholds dependent on the problem being analysed and justify them with simulations, instead of using Jeffrey's scale.

The Bayes factor method to perform model comparison presents several computational and theoretical issues.

[1]Two models are considered nested when one contains all the parameters of the other plus at least one additional one. The smaller model is called reduced (or restricted) while the larger model is called complete (or full).

Table A.1: Jeffrey scale.

B_{ij} [a]	$\ln(B_{ij})$ [b]	Evidence
$1 \leq B_{ij} < 3$	$0 \leq B_{ij} < 1.1$	Weak
$3 \leq B_{ij} < 20$	$1.1 \leq B_{ij} < 3$	Definite
$20 \leq B_{ij} < 150$	$3 \leq B_{ij} < 5$	Strong
$150 \leq B_{ij}$	$5 \leq B_{ij}$	Very strong

[a] Model components.
[b] Logarithm of the Bayes evidence of the full sample normalized to the largest evidence.

The Bayes factor can be really hard or even impossible to calculate, especially for large models with many random effects and large improper or unknown priors (non-parametric models). Often one needs to recur to less computationally intense methods.

As we have seen in the previous sections, the Bayesian model comparison involves marginalizing across the prior distribution for each model (Kruschke 2015). Therefore, one of the main issues of the Bayes factor method is its extreme sensitivity to the prior distribution shape (Kamary et al. 2014). Priors using wide parameter spaces not realized in the data penalize the model and thus influence the Bayes factor. In fact, this is one of the main criticisms of using Bayes factors for model comparison, because by modifying the parameter prior ranges/definitions, you can get arbitrary Bayes factors. The problem however is more relevant in a field where the models are empirical. In astrophysics, however, we can avail of physically justified models that should confirm the credibility of the method.

The way to solve this issue is to use Monte Carlo simulations to define the threshold where an odds ratio or Bayes factor should be preferred. In that case, such multiplicative factors are taken care of.

This is a frequentist method (good for characterizing methods) to calibrate Bayesian inference machinery (good for inferring about the world).

Moreover, to avoid biases from the prior distribution, one could concentrate attention directly on the posterior model probabilities rather than on the marginal likelihood or Bayes factor. In fact, the posterior distribution on the continuous parameters is robust against changes in non-descriptive priors.

A.4 The Occam's razor

Using large models we might risk overfitting the data. An overfitting model has more parameters justified by the data, producing an analysis corresponding too closely to a particular set of data and that will fail to fit additional data reliably. This is a problem while using comparison methods like the Maximum Likelihood Estimator, but Bayesian model comparison can avoid it. In fact, the Bayes factor embodies naturally an automatic "Occam's razor" effect (Jefferys & Berger 1992b).

Occam's razor is a philosophical concept that states that the simplest explanation of an occur-

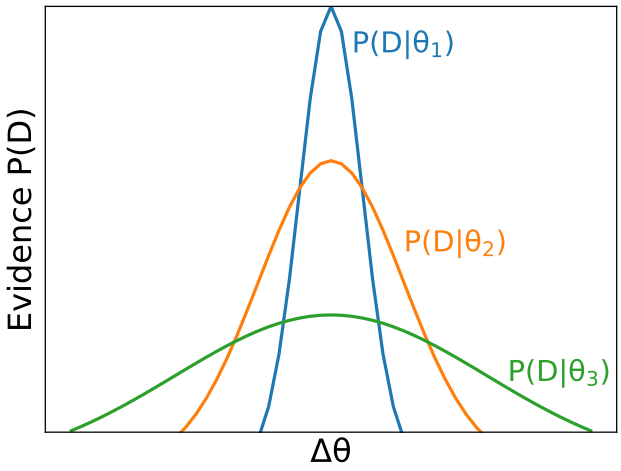

Figure A.1: Qualitative interpretation of the evidence for three models with different complexity. Models that are too simple (θ_1, blue) are unlikely to generate the data set, while models that are too complex (θ_3, green) can generate many possible data set, so it is again unlikely for them to generate the real data.

rence, which is the explanation that requires the smallest number of assumptions, is usually the correct explanation. This is a heuristic concept adopted by scientists and statisticians to accept the simplest possible model to describe the data and avoid overfitting.

As the integral of the likelihood over the prior parameter space, the evidence is usually larger for a model if its parameter space is smaller hence more of its parameters are likely. In contrast, the evidence of a model with large parameter spaces where large parts have low likelihood (i.e., not justified or needed by the data) is penalized. This can be reconstructed from Equation A.4

$$Z = P(D) = \int d\theta P(D|\theta)P(\theta) \sim P(\hat{\theta})\delta\hat{\theta}L(\hat{\theta}) \sim \frac{\delta\hat{\theta}}{\Delta\theta}L(\hat{\theta})\hat{\theta}, \tag{A.7}$$

where $\hat{\theta}$ is the best fit parameter, $\delta\hat{\theta}$ is the posterior accessible volume around $\hat{\theta}$ and in the third step we assume a uniform prior

$$P(\hat{\theta}) = \frac{\hat{\theta}}{\Delta\theta}, \tag{A.8}$$

and $\Delta\theta$ is the prior accessible volume. The factor $\delta\hat{\theta}/\Delta\theta$ is the Occam's factor, which is the ratio between the posterior accessible volume over the prior accessible volume. A complex model with many parameters, i.e. a larger prior accessible volume, will have lower evidence with respect to a model with fewer parameters (see Figure A.1).

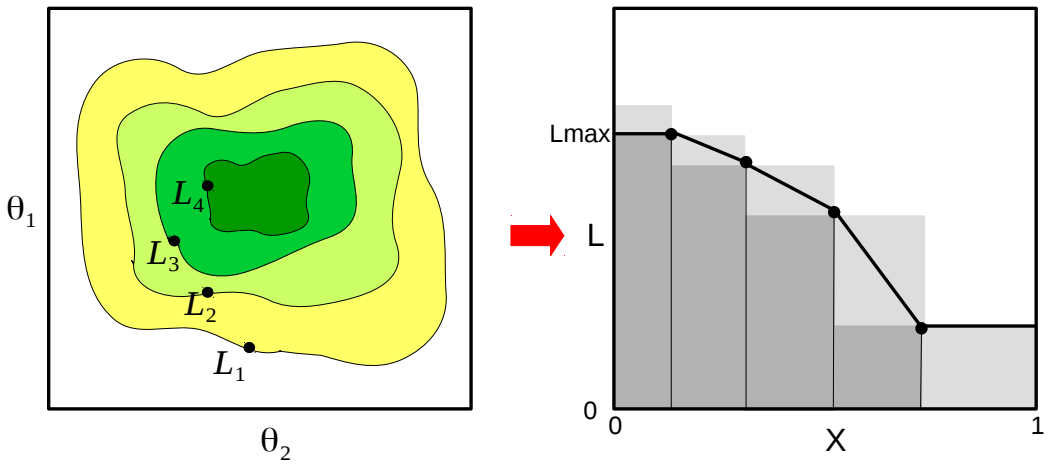

Figure A.2: *Right:* Illustration of the posterior of a two dimensional problem. *Left:* The transformed L(X) function where the prior volumes X_i are associated with each likelihood L_i. The key idea in the nested sampling algorithm is that any high dimensional problem can be mapped to an easy one dimensional one. (Figure adapted from Skilling 2006)

A.5 The Nested Sampling Algorithm

The integral to calculate the Bayesian evidence Z is often non-trivial and cannot be solved analytically. In some cases, the likelihood function can be multi-modal, adding complexity to the evidence integral.

The Nested Sampling (NSA) Algorithm is a computational approach developed by Skilling (2004) to calculated efficiently the Bayesian evidence and produce posterior distribution inferences as a by-product.

We can reduce the solution of the evidence integral to a one-dimensional problem by defining the prior volume X associated to likelihoods greater than ℓ as

$$\mathrm{X(L)} = \int_{\ell(\theta)>\mathrm{L}} \pi(\theta)\mathrm{d}\theta. \tag{A.9}$$

This is a decreasing function with X(0) = 1 and $\mathrm{X}(\mathrm{L}_{\mathrm{max}}) = 0$. Then the evidence integral can be written as

$$\mathrm{Z} = \int_0^1 \mathrm{L(X)dX}, \tag{A.10}$$

where dX is the prior mass associated with the likelihood in the interval [L, L + dL].

Let us assume that we can uniformly sample objects from their prior $\pi(\theta)$. Since X defines the prior mass, this is equivalent to sampling uniformly over X. Thus, to calculate numerically the integral in equation A.10, we start by choosing a sequence of N decreasing X values, starting at $X_0 = 1$.

$$X_N < X_{N-1} < ... < X_2 < X_1 < X_0 = 1. \tag{A.11}$$

We then evaluate the likelihood in the N points

$$L_i = L(X_i), \quad i = 1, 2, 3, ... \tag{A.12}$$

In the next step, we add the contribution of the lowest likelihood point L_i to the evidence and then we replace this point by a new randomly drawn point with a higher likelihood than L_i. Therefore, the NSA algorithm reduces the prior volume at every step towards higher likelihoods by removing a live point at a time without drawing N new points every iteration. The "shrinkage" of the prior volume is tracked by multiplying the minimum likelihood in step i with a weight $w_i \sim \Delta X$ indicating the current step height. Hence, following the trapezoidal rule we could define $w_i = (X_{i-1} - X_i)/2$ or we could use the simple interval $w_i = X_{i-1} - X_i$. The evidence in the i^{th} iteration is thus given by

$$Z_i = Z_{i-1} + w_i L_i. \tag{A.13}$$

We repeat the last steps until a convergence criterion is satisfied. For example, we could stop the algorithm when the maximum of the likelihood in that step is smaller than a small fraction of the evidence in the step before, that is $\max(L_1, ..., L_N) < fZ_j$, where f is a small fraction.

To sum up, the integral of the Bayes evidence Z is evaluated by:

1. we sample N points from the prior space,
2. we calculate the likelihood for the N points and select the minimum likelihood L_i,
3. we set the weights as $w_i = (X_{i-1} - X_i)/2$,
4. the new evidence is given by equation A.13,
5. the point of minimum likelihood is replaced with one drawn with $L(\theta) > L_i$,
6. repeat steps from 2 to 5 until a convergence criterion is met.

Thus, the complex integral to calculate the evidence is approximated using the trapezium rule.

Even though the NSA algorithm is designed to calculate the Bayesian evidence, we can obtain the posterior distribution of the model parameters naturally as a by-product. In fact, we can infer the posterior distribution using final live points and the points with the lowest likelihood value at each iteration of the algorithm (that is, the full sequence of discarded points from the NSA process). Each of such points is assigned the importance weight as follows

$$P_i = \frac{L_i w_i}{\sum_i L_i w_i} = \frac{L_i w_i}{Z}. \tag{A.14}$$

From Eq. A.14 one can calculate estimates (for example mean, standard deviation, covariances ecc.) for the key posterior parameters.

A.6 BXA and PyMultiNest

Always more studies rely on Bayesian inference for their analysis. Especially in X-ray astronomy, the use of NSA algorithms is particularly spread (e.g. Buchner et al. 2015; Graff et al. 2016; Sokolov et al. 2020; Mollière et al. 2020, and work in the previous Chapters), thanks to `pyMultiNest` (Buchner et al. 2014), the python wrapping of `MultiNest` (Feroz & Hobson 2008; Feroz et al. 2009, 2013).

The NSA allows us to sample from the prior under a likelihood constraint. We have at each iteration a sample of live points available, which fulfill this constraint. The `MultiNest` algorithm implements the NSA algorithm with an ellipsoidal rejection sampling scheme. More in detail, `MultiNest` uses the live points to wrap them into a combination of ellipsoids, enlarges the live point region by a factor, and samples from them. As soon as the likelihood of a sampled point is fulfills the current likelihood constraint, it is used in NS as the replaced live point.

At each iteration step i, the set of live points, N_{live}, is enclosed within a set of overlapping ellipsoids and the desired replacement point is sought within their union. The ellipsoidal decomposition algorithm allows great flexibility in the shape of the posterior exploration. Thus, `MultiNest` is particularly indicated for problems with elongated, curving degeneracies or multi-modal distributions while maintaining high efficiency in simpler problems. There are many other software and statistical frameworks used to perform the NSA algorithm and other Bayesian methods, for example, `Stan` (Stan Development Team 2014) and `UltraNest` (Buchner 2019) (see Chapter 3), however, in this thesis I mainly use the python wrapper of `MultiNest`.

Of particular importance for this work is the python package Bayesian X-ray Analysis (BXA) developed by (Buchner et al. 2015) and based on `MultiNest`. BXA in a Bayesian framework to connects the X-ray analysis software SHERPA and XSPEC with `pyMultiNest` for Bayesian parameter estimation and Bayesian inference.

BXA can be used for parameter estimation, including features like finding the best fit and computing posterior probability distributions, has functions to plot the spectral data versus the model fit, both for the best fit and for all the solutions (posterior sample) and can be used for model selection by computing the Bayesian evidence and model comparison by visualizing the deviation between data and model with Quantile-Quantile (QQ) plots.

Moreover, BXA also provides background models for some of the majors X-ray observatories (e.g. *Chandra*, *XMM-newton*, *Swift*, and more) to allow the statistically robust handling of the background. Many X-ray astronomers chose to subtract the background from the raw data. However, this approach might lead to statistical issues. In particular, subtracting the background reduces the amount of statistical information in the analysis making the final fit parameter values less accurate. The analysis might also be compromised if there are fluctuations present in the vicinity of localized features. Especially in the case of low count statistics, subtracting the background might impair the analysis because the background-subtracted data are not Poisson distributed and in some cases might even have negative counts. The background-subtracted spectra should then not be fit with Poisson distribution or the Cash statistic. The proper way to treat background data is therefore to model them.

Throughout this thesis, we use BXA to fit X-ray spectra and to calculate the Bayesian evidence for the fitted model and its best-fit parameters. Thanks to the Bayesian evidence we can

then compare different models and select which one of them fits the data better using the Bayes factor method (see Section A.3)

A.7 Hierarchical Bayesian modeling

To make predictions about a population based on the characteristics of the individual objects in the population one can use a Hierarchical Bayesian Model (HBM).

Assuming that the population can be described by the probability distribution function $N(\theta|\alpha)$, where α are the parameters of the distribution, then the distributions of population properties, when normalized, can be interpreted as probability distributions for individual parameters.

$$P(\theta) = N(\theta|\alpha) \int N(\theta\alpha)d\theta = P(\theta|\alpha). \tag{A.15}$$

Thus, the Bayes theorem can be written as

$$P(\theta|D) \propto P(D|\theta)P(\theta) = P(D|\theta)P(\theta|\alpha), \tag{A.16}$$

and the population can be used to make inferences on individual observations. However, we can write eq. A.16 for the population so that the individual observation can be used to find the population parameters α, as follows

$$P(\alpha, \theta|D) \propto P(D|\theta, \alpha)P(\theta, \alpha)P(\alpha), \tag{A.17}$$

where $P(D|\theta, \alpha)P(\theta, \alpha)$ is the likelihood. By marginalizing over the parameters of the individual objects we find

$$P(\alpha|D) \propto \int [P(D|\theta, \alpha)P(\theta, \alpha)d\theta]P(\alpha). \tag{A.18}$$

To sum up, HBM is needed to find simultaneous posteriors on individuals and population parameters and to quantify the uncertainty in those parameters (see also Chapter 3).

Bibliography

Aird J., et al., 2010, MNRAS, 401, 2531

Aird J., Coil A. L., Georgakakis A., Nandra K., Barro G., Pérez-González P. G., 2015, MNRAS, 451, 1892

Antonucci R. R. J., 1984, ApJ, 278, 499

Antonucci R., 1993, ARA&A, 31, 473

Antonucci R. R. J., Miller J. S., 1985, ApJ, 297, 621

Arnaud K. A., 1996, in Jacoby G. H., Barnes J., eds, Astronomical Society of the Pacific Conference Series Vol. 101, Astronomical Data Analysis Software and Systems V. p. 17

Baade W., Minkowski R., 1954, ApJ, 119, 206

Balbus S. A., Hawley J. F., 1991, ApJ, 376, 214

Balick B., Brown R. L., 1974, ApJ, 194, 265

Ballantyne D. R., Fabian A. C., 2003, ApJ, 592, 1089

Bambi C., 2017, X-Ray Reflection Spectroscopy. Springer Singapore, Singapore, pp 153–179, doi:10.1007/978-981-10-4524-0_8, https://doi.org/10.1007/978-981-10-4524-0_8

Barger A. J., Cowie L. L., Mushotzky R. F., Yang Y., Wang W. H., Steffen A. T., Capak P., 2005, AJ, 129, 578

Baronchelli L., Nandra K., Buchner J., 2018, MNRAS, 480, 2377

Baronchelli L., Nandra K., Buchner J., 2020, Monthly Notices of the Royal Astronomical Society, 498, 5284

Barret D., et al., 2016, in Society of Photo-Optical Instrumentation Engineers (SPIE) Conference Series, Vol. 9905, Proc. SPIE. p. 99052F, doi:10.1117/12.2232432

Bartalucci I., Mazzotta P., Bourdin H., Vikhlinin A., 2014, A&A

Baum S. A., O'Dea C. P., Dallacassa D., de Bruyn A. G., Pedlar A., 1993, ApJ, 419, 553

Bavdaz M., et al., 2015, in O'Dell S. L., Pareschi G., eds, Vol. 9603, Optics for EUV, X-Ray, and Gamma-Ray Astronomy VII. SPIE, pp 128 – 140, doi:10.1117/12.2188074, https://doi.org/10.1117/12.2188074

Begelman M. C., 1985, in Miller J. S., ed., Astrophysics of Active Galaxies and Quasi-Stellar Objects. pp 411–452

Beloborodov A. M., 1999, ApJ, 510, L123

Berta Z. K., Jimenez R., Heavens A. F., Panter B., 2008, Monthly Notices of the Royal Astronomical Society, 391, 197

Berti E., Volonteri M., 2008, ApJ, 684, 822

Betancourt M., Girolami M., 2015, Current trends in Bayesian methodology with applications, 79, 2

Blackburn J. K., 1995, in Shaw R. A., Payne H. E., Hayes J. J. E., eds, Astronomical Society of the Pacific Conference Series, Vol. 77, Astronomical Data Analysis Software and Systems IV. p. 367

Bondi H., 1952, MNRAS, 112, 195

Brandt W. N., Hasinger G., 2005, ARA&A, 43, 827

Brenneman L., 2013, Measuring the Angular Momentum of Supermassive Black Holes, doi:10.1007/978-1-4614-7771-6.

Brenneman L. W., Reynolds C. S., 2006, ApJ, 652, 1028

Brightman M., Nandra K., Salvato M., Hsu L.-T., Aird J., Rangel C., 2014, MNRAS, 443, 1999

Broderick A. E., Fish V. L., Doeleman S. S., Loeb A., 2011, ApJ, 735, 110

Bromley B. C., Miller W. A., Pariev V. I., 1998, in Holt S. S., Kallman T. R., eds, American Institute of Physics Conference Series Vol. 431, American Institute of Physics Conference Series. pp 269–272, doi:10.1063/1.55869

Broos P. S., Townsley L. K., Feigelson E. D., Getman K. V., Bauer F. E., Garmire G. P., 2010, ApJ, 714, 1582

Broos P., Townsley L., Getman K., Bauer F., 2012, AE: ACIS Extract (ascl:1203.001)

Brunner H., Cappelluti N., Hasinger G., Barcons X., Fabian A. C., Mainieri V., Szokoly G., 2008, A&A, 479, 283

Brusa M., Gilli R., Comastri A., 2005, ApJ, 621, L5

Buchner J., 2019, Publications of the Astronomical Society of the Pacific, 131, 108005

Buchner J., et al., 2014, A&A, 564, 25

Buchner J., et al., 2015, ApJ, 802, 89

Capellupo D. M., Netzer H., Lira P., Trakhtenbrot B., Mejía-Restrepo J., 2015, MNRAS, 446, 3427

Cash W., 1979, ApJ, 228, 939

Chandrasekhar S., 1931, MNRAS, 91, 456

Chandrasekhar S., 1984, Journal of Astrophysics and Astronomy, 5, 3

Chartas G., Kochanek C. S., Dai X., Moore D., Mosquera A. M., Blackburne J. A., 2012, ApJ, 757, 137

Chaudhary P., Brusa M., Hasinger G., Merloni A., Comastri A., Nandra K., 2012, A&A, 537, A6

Chiang J., Reynolds C. S., Blaes O. M., Nowak M. A., Murray N., Madejski G., Marshall H. L., Magdziarz P., 2000, ApJ, 528, 292

Chruściel P. T., Costa J. L., Heusler M., 2012, Living Reviews in Relativity, 15, 7

Civano F., et al., 2016, ApJ, 819, 62

Clavel J., et al., 1991, ApJ, 366, 64

Clavel J., et al., 1992, ApJ, 393, 113

Comastri A., 2004, Compton-Thick AGN: The Dark Side of the X-Ray Background. p. 245, doi:10.1007/978-1-4020-2471-9_8

Comastri A., Brusa M., Civano F., 2004, MNRAS, 351, L9

Corral A., et al., 2008, A&A, 492, 71

Corral A., Della Ceca R., Caccianiga A., Severgnini P., Brunner H., Carrera F. J., Page M. J., Schwope A. D., 2011, A&A, 530, A42

Crenshaw D. M., et al., 1996, ApJ, 470, 322

Dadina M., 2008, Mem. Soc. Astron. Italiana, 79, 140

Dai X., Steele S., Guerras E., Morgan C. W., Chen B., 2019, ApJ, 879, 35

Dauser T., Wilms J., Reynolds C. S., Brenneman L. W., 2010, MNRAS, 409, 1534

Dauser T., Garcia J., Wilms J., Böck M., Brenneman L. W., Falanga M., Fukumura K., Reynolds C. S., 2013, MNRAS, 430, 1694

Edelson R., 2000, New A Rev., 44, 423

Edelson R., et al., 2015, ApJ, 806, 129

Elitzur M., 2006, Unification Issues and the AGN Torus (arXiv:astro-ph/0612458)

Elitzur M., 2007, Unification Issues and the AGN Torus. p. 415

Elitzur M., 2008, New A Rev., 52, 274

Elitzur M., 2012, ApJ, 747, L33

Elvis M., Maccacaro T., Wilson A. S., Ward M. J., Penston M. V., Fosbury R. A. E., Perola G. C., 1978, MNRAS, 183, 129

Elvis M., Fassnacht C., Wilson A. S., Briel U., 1990, ApJ, 361, 459

Elvis M., et al., 1994, ApJS, 95, 1

Erkut M. H., 2011, ApJ, 743, 5

Event Horizon Telescope Collaboration et al., 2019, ApJ, 875, L1

Fabian A. C., 2006, in Wilson A., ed., ESA Special Publication Vol. 604, The X-ray Universe 2005. p. 463 (arXiv:astro-ph/0511537)

Fabian A. C., Rees M. J., Stella L. & White N. E., 1989, MNRAS, 238, 729

Fabian A. C., Nandra K., Reynolds C. S., Brandt W. N., Otani C., Tanaka Y., Inoue H., Iwasawa K., 1995, MNRAS, 277, L11

Fabian A. C., Iwasawa K., Reynolds C. S., Young A. J., 2000, PASP, 112, 1145

Fabian A. C., et al., 2002, MNRAS, 335, L1

Fabian A. C., Miniutti G., Gallo L., Boller T., Tanaka Y., Vaughan S., Ross R. R., 2004, MNRAS, 353, 1071

Fabian A. C., Miniutti G., Iwasawa K., Ross R. R., 2005, MNRAS, 361, 795

Falocco S., Carrera F. J., Corral A., Laird E., Nandra K., Barcons X., Page M. J., Digby-North J., 2012, A&A, 538, A83

Falocco S., et al., 2013, A&A, 555, A79

Falocco S., Carrera F. J., Barcons X., Miniutti G., Corral A., 2014, A&A, 568, A15

Fath E. A., 1909, Lick Observatory Bulletin, 5, 71

Feroz F., Hobson M. P., 2008, MNRAS, 384, 449

Feroz F., Hobson M. P., Bridges M., 2009, MNRAS, 398, 1601

Feroz F., Hobson M. P., Cameron E., Pettitt A. N., 2013, preprint, (arXiv:1306.2144)

Frank J., King A., Raine D. J., 2002, Accretion Power in Astrophysics: Third Edition

Freeman P., Doe S., Siemiginowska A., 2001, in Starck J.-L., Murtagh F. D., eds, Proc. SPIEVol. 4477, Astronomical Data Analysis. pp 76–87 (arXiv:astro-ph/0108426), doi:10.1117/12.447161

Fruscione A., et al., 2006, in Society of Photo-Optical Instrumentation Engineers (SPIE) Conference Series, Vol. 6270, Proc. SPIE. p. 62701V, doi:10.1117/12.671760

García J., Kallman T. R., 2010, ApJ, 718, 695

García J., Dauser T., Reynolds C. S., Kallman T. R., McClintock J. E., Wilms J., Eikmann W., 2013, ApJ, 768, 146

García J., et al., 2014, ApJ, 782, 76

Gebhardt K., et al., 2000, ApJ, 539, L13

Gelman A., 2002, Prior distribution. Encyclopedia of Environmetrics Vol. 3, John Wiley & Sons

Georgakakis A., Nandra K., Laird E. S., Aird J., Trichas M., 2008, MNRAS, 388, 1205

Georgakakis A., et al., 2011, MNRAS, 418, 2590

George I. M., Fabian A. C., 1991, MNRAS, 249, 352

Ghisellini G., Haardt F., Matt G., 1994, MNRAS, 267, 743

Giacconi R., Gursky H., Paolini F. R., Rossi B. B., 1962, Physical Review Letters, 9, 439

Gierliński M., Done C., 2004, MNRAS, 347, 885

Gierliński M., Done C., 2006, MNRAS, 371, L16

Gierliński M., Nikołajuk M., Czerny B., 2008, MNRAS, 383, 741

Gondoin P., Orr A., Lumb D., 2003, A&A, 398, 967

Graff P. B., Lien A. Y., Baker J. G., Sakamoto T., 2016, ApJ, 818, 55

Greenstein J. L., Matthews T. A., 1963, AJ, 68, 279

Guainazzi M., et al., 1999, A&A, 341, L27

Guainazzi M., Matt G., Perola G. C., 2005, Astronomy & Astrophysics, 444, 119âĂŞ132

Guainazzi M., Bianchi S., Dovčiak M., 2006, Astronomische Nachrichten, 327, 1032

Guilbert P. W., Rees M. J., 1988, MNRAS, 233, 475

Haardt F., Maraschi L., 1991, ApJ, 380, L51

Haardt F., Maraschi L., 1993, ApJ, 413, 507

Hartle J. B., 2003, Gravity : an introduction to Einstein's general relativity

Hasinger G., 2004, Nuclear Physics B Proceedings Supplements, 132, 86

Hasinger G., Miyaji T., Schmidt M., 2005, A&A, 441, 417

Hazard C., Mackey M. B., Shimmins A. J., 1963, Nature, 197, 1037

Heckman T. M., 1980, A&A, 87, 152

Heusler M., 1998, Living Reviews in Relativity, 1, 6

Hitomi Collaboration et al., 2016, Nature, 535, 117

Ho L., 1999, in Chakrabarti S. K., ed., Astrophysics and Space Science Library Vol. 234, Observational Evidence for the Black Holes in the Universe. p. 157, doi:10.1007/978-94-011-4750-7_11

Ho L. C., Filippenko A. V., Sargent W. L. W., 1997, ApJS, 112, 315

Hopkins P. F., Cox T. J., Younger J. D., Hernquist L., 2009, ApJ, 691, 1168

Hsu L.-T., et al., 2014, ApJ, 796, 60

Hubble E. P., 1926, ApJ, 64

Iwasawa K., Taniguchi Y., 1993, ApJ, 413, L15

Iwasawa K., et al., 1996, MNRAS, 282, 1038

Jansky K. G., 1933, Nature, 132, 66

Jefferys W. H., Berger J. O., 1992a, American Scientist, 80, 64

Jefferys W. H., Berger J., 1992b, American Scientist, 80, 64

Jeffreys H., 1939, Theory of Probability. Oxford University Press Inc.

Jovanović P., Popović L. Č., 2009, preprint, (arXiv:0903.0978)

Kamary K., Mengersen K., Robert C. P., Rousseau J., 2014, arXiv e-prints, p. arXiv:1412.2044

Kerr R. P., 1963, Phys. Rev. Lett., 11, 237

Khachikian E. Y., Weedman D. W., 1974, ApJ, 192, 581

King A. R., Pringle J. E., 2006, MNRAS, 373, L90

Kinkhabwala A., Behar E., Sako M., Gu M. F., Kahn S. M., Paerels F. B. S., 2003, arXiv e-prints, pp astro–ph/0304332

Kolodzig A., Gilfanov M., Sunyaev R., Sazonov S., Brusa M., 2013, A&A, 558, A89

Komatsu E., et al., 2011, ApJS, 192, 18

Korista K. T., et al., 1995, ApJS, 97, 285

Kormendy J., Richstone D., 1995, Annual Review of Astronomy and Astrophysics, 33, 581

Kristian J., 1973, ApJ, 179, L61

Krolik J. H., 1999, Active Galactic Nuclei: From the Central Black Hole to the Galactic Environment. Princeton University Press

Krolik J. H., Begelman M. C., 1988, ApJ, 329, 702

Krolik J. H., Kallman T. R., 1987, ApJ, 320, L5

Krolik J. H., Madau P., Zycki P. T., 1994, ApJ, 420, L57

Kruschke J. K., 2015, in Kruschke J. K., ed., , Doing Bayesian Data Analysis (Second Edition), second edition edn, Academic Press, Boston, pp 265 – 296, doi:https://doi.org/10.1016/B978-0-12-405888-0.00010-6, http://www.sciencedirect.com/science/article/pii/B9780124058880000106

Laird E. S., et al., 2009, ApJS, 180, 102

Laor A., 1991, ApJ, 376, 90

Laor A., Netzer H., 1989, MNRAS, 238, 897

Lawrence A., 2012, Monthly Notices of the Royal Astronomical Society, 423, 451

Lawrence A., 2018, Nature Astronomy, 2, 102

Lawrence A., Elvis M., 1982, ApJ, 256, 410

Lee J. C., Fabian A. C., Iwasawa K., Reynolds C. S., Brandt W. N., 1999a, Nuclear Physics B Proceedings Supplements, 69, 486

Lee J. C., Fabian A. C., Brandt W. N., Reynolds C. S., Iwasawa K., 1999b, MNRAS, 310, 973

Lee J. C., Ogle P. M., Canizares C. R., Marshall H. L., Schulz N. S., Morales R., Fabian A. C., Iwasawa K., 2001, ApJ, 554, L13

Lee J. C., Iwasawa K., Houck J. C., Fabian A. C., Marshall H. L., Canizares C. R., 2002, ApJ, 570, L47

Li T. P., Ma Y. Q., 1983, ApJ, 272, 317

Lightman A. P., White T. R., 1988, ApJ, 335, 57

Liu Z., et al., 2016, MNRAS, 459, 1602

Luo B., et al., 2017, ApJS, 228, 2

Lynden-Bell D., 1969, Nature, 223, 690

Magdziarz P., Zdziarski A. A., 1995, MNRAS, 273, 837

Magorrian J., et al., 1998, AJ, 115, 2285

Malkan M. A., 1983, ApJ, 268, 582

Mantovani G., Nandra K., Ponti G., 2014, MNRAS, 442, L95

Mantovani G., Nandra K., Ponti G., 2016, MNRAS, 458, 4198

Martocchia A., Karas V., Matt G., 2000, MNRAS, 312, 817

Matsuoka M., Piro L., Yamauchi M., Murakami T., 1990, ApJ, 361, 440

Matt G., 2002, MNRAS, 337, 147

Matt G., Fabian A. C., Reynolds C. S., 1997, MNRAS, 289, 175

Matthews T. A., Sandage A. R., 1963, ApJ, 138, 30

McHardy I., 1988, Mem. Soc. Astron. Italiana, 59, 239

McHardy I. M., Gunn K. F., Uttley P., Goad M. R., 2005, MNRAS, 359, 1469

McHardy I. M., et al., 2016, Astronomische Nachrichten, 337, 500

Meidinger N., Eder J., Eraerds T., Nand ra K., Pietschner D., Plattner M., Rau A., Strecker R., 2016, in Society of Photo-Optical Instrumentation Engineers (SPIE) Conference Series, Vol. 9905, Proc. SPIE. p. 99052A, doi:10.1117/12.2231604

Menzel M. L., et al., 2016, VizieR Online Data Catalog, p. J/MNRAS/457/110

Merloni A., et al., 2012, preprint, (arXiv:1209.3114)

Miller J. M., Fabian A. C., in't Zand J. J. M., Reynolds C. S., Wijnands R., Nowak M. A., Lewin W. H. G., 2002, ApJ, 577, L15

Miller L., Turner T. J., Reeves J. N., George I. M., Kraemer S. B., Wingert B., 2007, A&A, 463, 131

Miller L., Turner T. J., Reeves J. N., 2008, A&A, 483, 437

Miniutti G., 2006, Astronomische Nachrichten, 327, 969

Miniutti G., Fabian A. C., 2004, MNRAS, 349, 1435

Miniutti G., Fabian A. C., Goyder R., Lasenby A. N., 2003, MNRAS, 344, L22

Miniutti G., et al., 2007, PASJ, 59, 315

Minkowski R., 1960, ApJ, 132, 908

Misner C. W., Thorne K. S., Wheeler J. A., 1973, Gravitation

Misra R., Kembhavi A. K., 1998, ApJ, 499, 205

Misra R., Sutaria F. K., 1999, ApJ, 517, 661

Miyoshi M., Moran J., Herrnstein J., Greenhill L., Nakai N., Diamond P., Inoue M., 1995, Nature, 373, 127

Mollière P., et al., 2020, arXiv e-prints, p. arXiv:2006.09394

Montgomery C., Orchiston W., Whittingham I., 2009, Journal of Astronomical History and Heritage, 12, 90

Morrison R., McCammon D., 1983, ApJ, 270, 119

Mushotzky R., 2004, How are AGN Found?. p. 53, doi:10.1007/978-1-4020-2471-9_2

Mushotzky R. F., Edelson R., Baumgartner W., Gand hi P., 2011, ApJ, 743, L12

Nandra K., 2006, MNRAS, 368, L62

Nandra K., Pounds K. A., 1994, MNRAS, 268, 405

Nandra K., Pounds K. A., Stewart G. C., Fabian A. C., Rees M. J., 1989, MNRAS, 236, 39P

Nandra K., George I. M., Mushotzky R. F., Turner T. J., Yaqoob T., 1997a, ApJ, 477, 602

Nandra K., George I. M., Mushotzky R. F., Turner T. J., Yaqoob T., 1997b, ApJ, 488, L91

Nandra K., George I. M., Mushotzky R. F., Turner T. J., Yaqoob T., 1999, ApJ, 523, L17

Nandra K., O'Neill P. M., George I. M., Reeves J. N., 2007, MNRAS, 382, 194

Nandra K., et al., 2013, preprint, (arXiv:1306.2307)

Nandra K., et al., 2015, ApJS, 220, 10

Narayan R., 2005, New Journal of Physics, 7, 199

Narayan R., Yi I., 1994, ApJ, 428, L13

Nenkova M., Sirocky M. M., Nikutta R., Ivezić Ž., Elitzur M., 2008, ApJ, 685, 160

Nesseris S., García-Bellido J., 2013, Journal of Cosmology and Astroparticle Physics, 2013, 036

Niedźwiecki A., Zdziarski A. A., Szanecki M., 2016, ApJ, 821, L1

Novikov I. D., Thorne K. S., 1973, in Black Holes (Les Astres Occlus). pp 343–450

Nowak M. A., Chiang J., 2000, ApJ, 531, L13

Oda M., Gorenstein P., Gursky H., Kellogg E., Schreier E., Tananbaum H., Giacconi R., 1971, ApJ, 166, L1

Oke J. B., 1963, Nature, 197, 1040

Oknyansky V. L., Malanchev K. L., Gaskell C. M., 2018, in Revisiting Narrow-Line Seyfert 1 Galaxies and their Place in the Universe. p. 12 (arXiv:1810.08844)

Oppenheimer J. R., Snyder H., 1982, On Continued Gravitational Contraction. p. 36

Oppenheimer J. R., Volkoff G. M., 1939, Physical Review, 55, 374

Osterbrock D. E., 1977, ApJ, 215, 733

Page D. N., Thorne K. S., 1974, ApJ, 191, 499

Page M. J., Davis S. W., Salvi N. J., 2003, MNRAS, 343, 1241

Pariev V. I., Bromley B. C., 1998, ApJ, 508, 590

Patrick A. R., Reeves J. N., Lobban A. P., Porquet D., Markowitz A. G., 2011, Monthly Notices of the Royal Astronomical Society, 416, 2725

Peterson B. M., 1993, PASP, 105, 247

Ponti G., Miniutti G., Cappi M., Maraschi L., Fabian A. C., Iwasawa K., 2006, MNRAS, 368, 903

Pounds K. A., Nandra K., Stewart G. C., George I. M., Fabian A. C., 1990, Nature, 344, 132

Pounds K. A., Reeves J. N., Page K. L., Wynn G. A., O'Brien P. T., 2003, MNRAS, 342, 1147

Predehl P., et al., 2010, in Space Telescopes and Instrumentation 2010: Ultraviolet to Gamma Ray. p. 77320U (arXiv:1001.2502), doi:10.1117/12.856577

Pringle J. E., 1981, ARA&A, 19, 137

Pringle J. E., Rees M. J., 1972, A&A, 21, 1

Psaltis D., 2008, Living Reviews in Relativity, 11, 1433

Ranalli P., et al., 2013, A&A, 555, A42

Rangel C., Nandra K., Laird E. S., Orange P., 2013, MNRAS, 428, 3089

Rau A., et al., 2013, arXiv e-prints, p. arXiv:1308.6785

Rees M. J., 1984, ARA&A, 22, 471

Rees M. J., Mészáros P., 1998, ApJ, 496, L1

Reeves J., Done C., Pounds K., Terashima Y., Hayashida K., Anabuki N., Uchino M., Turner M., 2008, MNRAS, 385, L108

Reissner H., 1916, Annalen der Physik, 355, 106

Remillard R. A., McClintock J. E., 2006, ARA&A, 44, 49

Reynolds C. S., 1996, University of Cambridge

Reynolds C. S., 1999, Compton Reflection and Iron Fluorescence in Active Galactic Nuclei and Galactic Black Hole Candidates. p. 178

Reynolds C. S., 2000, ApJ, 533, 811

Reynolds C. S., 2001, in Peterson B. M., Pogge R. W., Polidan R. S., eds, Astronomical Society of the Pacific Conference Series Vol. 224, Probing the Physics of Active Galactic Nuclei. p. 105 (arXiv:astro-ph/0009503)

Reynolds C. S., Fabian A. C., 2008, ApJ, 675, 1048

Reynolds C. S., Nowak M. A., 2003, Phys. Rep., 377, 389

Reynolds C. S., Wilms J., 2000, ApJ, 533, 821

Ricci C., Walter R., Courvoisier T. J. L., Paltani S., 2011, A&A

Ricci C., Ueda Y., Paltani S., Ichikawa K., Gandhi P., Awaki H., 2014, MNRAS, 441, 3622

Ricci C., et al., 2017, Nature, 549, 488

Risaliti G., Elvis M., 2004, in Barger A. J., ed., Astrophysics and Space Science Library Vol. 308, Supermassive Black Holes in the Distant Universe. p. 187 (arXiv:astro-ph/0403618), doi:10.1007/978-1-4020-2471-9_6

Risaliti G., et al., 2013, Nature, 494, 449

Robert C. P., Chopin N., Rousseau J., 2009, Statist. Sci., 24, 141

Roseberry H. H., Bearden J. A., 1936, Physical Review, 50, 204

Ross R. R., Fabian A. C., 1993, MNRAS, 261, 74

Ross R. R., Fabian A. C., 2005, MNRAS, 358, 211

Rowan-Robinson M., 1977, ApJ, 213, 635

Ruszkowski M., Fabian A. C., Ross R. R., Iwasawa K., 2000, MNRAS, 317, L11

Sako M., et al., 2003, ApJ, 596, 114

Salpeter E. E., 1964, ApJ, 140, 796

Salvato M., et al., 2009, ApJ, 690, 1250

Salvato M., et al., 2011, ApJ, 742, 61

Sandage A., 1965, ApJ, 141, 1560

Schmidt M., 1963, Nature, 197, 1040

Schwarzschild K., 1999, arXiv e-prints, p. physics/9905030

Seyfert C. K., 1943, ApJ, 97, 28

Shakura N. I., 1972, AZh, 49, 921

Shakura N. I., Sunyaev R. A., 1973, A&A, 500, 33

Shakura N. I., Sunyaev R. A., Zilitinkevich S. S., 1978, A&A, 62, 179

Shankar F., Weinberg D. H., Miralda-Escudé J., 2009, ApJ, 690, 20

Shapiro S. L., Teukolsky S. A., Lightman A. P., 1983, Physics Today, 36, 89

Sim S. A., Long K. S., Miller L., Turner T. J., 2008, MNRAS, 388, 611

Skibo J. G., 1997, ApJ, 478, 522

Skilling J., 2004, AIP Conference Proceedings, 735, 395

Skilling J., 2006, Bayesian Analysis, 1, 833

Slipher V. M., 1917, Lowell Observatory Bulletin, 3, 59

Sokolov V., Pineda J. E., Buchner J., Caselli P., 2020, ApJ, 892, L32

Soltan A., 1982, MNRAS, 200, 115

Stan Development Team 2014, Stan: A C++ Library for Probability and Sampling, Version 2.2, http://mc-stan.org/

Steffen A. T., Barger A. J., Cowie L. L., Mushotzky R. F., Yang Y., 2003, ApJ, 596, L23

Streblyanska A., Hasinger G., Finoguenov A., Barcons X., Mateos S., Fabian A. C., 2005, A&A, 432, 395

Strohmayer T. E., 2001, ApJ, 552, L49

Sunyaev R. A., Titarchuk L. G., 1980, A&A, 86, 121

Tanaka Y., et al., 1995, Nature, 375, 659

Thorne K. S., 1974, ApJ, 191, 507

Tomsick J. A., Yamaoka K., Corbel S., Kaaret P., Kalemci E., Migliari S., 2009, ApJ, 707, L87

Tristram K. R. W., et al., 2007, A&A, 474, 837

Ueda Y., Akiyama M., Ohta K., Miyaji T., 2003, ApJ, 598, 886

Urry C. M., Padovani P., 1995, PASP, 107, 803

Uttley P., McHardy I. M., Papadakis I. E., 2002, MNRAS, 332, 231

Vaughan S., Fabian A. C., 2004, MNRAS, 348, 1415

Véron-Cetty M.-P., Véron P., 2006, A&A, 455, 773

Véron-Cetty M.-P., Véron P., 2010, A&A, 518, A10

Vianello G., 2018, ApJS, 236, 17

Vincent F. H., Różańska A., Zdziarski A. A., Madej J., 2016, A&A, 590, A132

Volonteri M., Haardt F., Madau P., 2003, ApJ, 582, 559

Volonteri M., Madau P., Quataert E., Rees M. J., 2005, ApJ, 620, 69

Volonteri M., Sikora M., Lasota J. P., Merloni A., 2013, ApJ, 775, 94

Wald R. M., 1984, General relativity

Wandel A., Peterson B. M., Malkan M. A., 1999, ApJ, 526, 579

Ward M., Elvis M., Fabbiano G., Carleton N. P., Willner S. P., Lawrence A., 1987, ApJ, 315, 74

Wille E., et al., 2015, in O'Dell S. L., Pareschi G., eds, Vol. 9603, Optics for EUV, X-Ray, and Gamma-Ray Astronomy VII. SPIE, pp 149 – 154, doi:10.1117/12.2187486, https://doi.org/10.1117/12.2187486

Williams B. J., Kelley R., Petre R., 2019, in AAS/High Energy Astrophysics Division. AAS/High Energy Astrophysics Division. p. 303.01

Wilms J., Reynolds C. S., Begelman M. C., Reeves J., Molendi S., Staubert R., Kendziorra E., 2001, MNRAS, 328, L27

Wilson T. L., Mehringer D. M., Dickel H. R., 1995, A&A, 303, 840

Wolter H., 1952a, Annalen der Physik, 445, 94

Wolter H., 1952b, Annalen der Physik, 445, 286

Woltjer L., 1959, ApJ, 130, 38

Xue Y. Q., et al., 2011, The Astrophysical Journal Supplement Series, 195, 10

Xue Y. Q., Luo B., Brandt W. N., Alexander D. M., Bauer F. E., Lehmer B. D., Yang G., 2016, VizieR Online Data Catalog, 222

Yaqoob T., 2007, in Ho L. C., Wang J.-W., eds, Astronomical Society of the Pacific Conference Series Vol. 373, The Central Engine of Active Galactic Nuclei. p. 109 (arXiv:astro-ph/0612527)

Yaqoob T., Padmanabhan U., 2004, ApJ, 604, 63

Yaqoob T., Padmanabhan U., Dotani T., Nandra K., 2002, ApJ, 569, 487

You J. H., Liu D. B., Chen W. P., Chen L., Zhang S. N., 2003, ApJ, 599, 164

Young A. J., Lee J. C., Fabian A. C., Reynolds C. S., Gibson R. R., Canizares C. R., 2005, ApJ, 631, 733

Zajacek M., Tursunov A., 2019, The Observatory, 139, 231

Zdziarski A. A., 1998, Monthly Notices of the Royal Astronomical Society, 296, L51

Zel'dovich Y. B., Novikov I. D., 1967, Soviet Ast., 10, 602

Zhang K., Wang T., Dong X., Lu H., 2008, ApJ, 685, L109

de La Calle Pérez I., et al., 2010, A&A, 524, A50

de la Calle Pérez I., et al., 2010, A&A,, 524,, A50

van der Klis M., 1995, in Alpar M. A., Kiziloglu U., van Paradijs J., eds, NATO Advanced Science Institutes (ASI) Series C Vol. 450, NATO Advanced Science Institutes (ASI) Series C. p. 301

Acknowledgement

Whoa, I cannot believe this is over. What a ride! As per tradition, I would like to take the opportunity to thank all the people that made this thesis possible, starting with my family for supporting me and cheering me up even if most of the time they were not understanding what this all was about. I am very grateful to my supervisor Prof. Dr. Kirpal Nandra for patiently bringing me to the end line and for always finding a way to spark up my projects when I thought they were completely swamped. Many thanks to Dr. Johannes Buchner, that always found time to direct and advise me and rescued my Ph.D. on multiple occasions. I also would like to thank the people of the high energy group, in particular Dr. Mara Salvato, for saying the right things when I needed them, and Dr. J. Michael Burgess, for saying the right things even if I didn't want to hear them. My profound gratitude goes also to my fellow and friends students, they have become like a second family to me and I will remember them all fondly. Finally, and most importantly, I want to thank Vlas, the keeper of my sanity. If it weren't for him my Ph.D. experience would have been very different and incredibly grimmer. So long, everyone! Thanks for everything.